Excited States in ^{161}W and ^{162}W and the Onset of Collectivity in the Neutron-Deficient Tungsten Isotopes.

Thesis submitted in accordance with the requirements of the University of Liverpool for the degree of Doctor in Philosophy

by

Emily Higgins

Oliver Lodge Laboratory

February 2019

The best that most of us can hope to achieve in physics is simply to misunderstand at a deeper level.

Wolfgang Pauli

Abstract

Excited states have been established in the neutron-deficient odd-N nucleus ^{161}W for the first time. The level scheme has been interpreted in terms of multi-particle excitations of independent nucleons outside of a closed shell.

The excitation level scheme for the neutron-deficient nuclide ^{162}W has been extended using recoil-decay correlations to a tentative spin of 17^{-}. The collective nucleus has been interpreted in terms of rotationally aligned bands. Configuration assignments have been made on the basis of comparisons of the angular momentum of initial emitting states, as a function of transition energy, with the predictions of the cranked shell model.

Comparisons made between these two nuclei and their neighbouring isotopes and isotones indicate rapid changes in nuclear structure dependent on the available valence space beyond the $N = 82$ shell closure.

Acknowledgements

I would like to thank my supervisor Professor David Joss for his support and guidance throughout the course of my studies.

Thank you to the STFC for providing funding, to everyone at the University of Jyväskylä accelerator lab for their expertise, and all the staff at Liverpool who have have always encouraged me and made this work possible.

I wouldn't have been able to get through if not for all members of the Nuclear group at Liverpool, they have provided the social and intellectual stimulation I needed to get the work done!

Finally I want to thank my parents for all they do for me and Haitham Alabiad for his support and understanding that really got me through.

Contents

List of Figures

Introduction

Prior to the 1940s the liquid drop model was the predominant theory used to describe the collective properties of the nucleus. However nuclear shell effects on the binding energy of the nucleus created the necessity to uncover an explanation for the many-body problem and reconcile the two seemingly contradictory theories.

Gamma-ray spectroscopy plays a major role in the exploration into the properties and structure of the nucleus. The underlying behaviour of a nucleus is dictated by its constituent nucleons within a potential generated by the mutual interactions of all constituents. As the number of valence nucleons outside of a closed shell increases the changes in behaviour can be subtle at times and overt at others, particularly when nearing a closed shell. In order to describe the complex interactions between nucleons in this many-body system the required computing power would be enormous, and for all but the lightest nuclei, completely impracticable. Thus the solution for now has been to describe, using models, the approximate nuclear potential of the system. These models require experimental data from a wide range of nuclei of different properties to constrain calculations. This has stimulated the development of increasingly sensitive instruments, improved accelerator technologies and investigative techniques in order to expand the field of experimentally accessible nuclei.

Figure 1 shows the chart of nuclides: it shows all naturally occurring nuclei and those synthesised artificially in nuclear reactions. Knowledge of excited states in

the heavy neutron-deficient nuclei with $N > 82$ has grown enormously in recent years. This region is of particular interest as it is a transitional region with nuclei approaching the N=82 closed shell and the proton drip line. At a closed shell nuclei are most commonly of a spherical shape. As nucleons are added to orbitals just beyond the closed shell it is known that they will exhibit phenomena related to single-particle excitations. As more valence nucleons are added they may develop a coherent motion within the mutual potential, which can in turn deform the nucleus.

The study of chains of isotones or isotopes can enable the understanding of systematic trends that occur when adding or removing nucleons from closed shell configurations. Investigations into these trends have been carried out with great interest in the nuclei with A$\sim$ 160 above the N=82 closed shell. With the help of the recoil-decay tagging technique discussed in section 3.6 it has become possible to study these extremely neutron-deficient exotic nuclei. The interplay between single-particle excitations and collective behaviour is what makes nuclei in this region particularly interesting. Above N=90 the nucleus very quickly deforms from spherical to deformed with the addition of just a few neutrons. The occupation of the $i_{13/2}$, $h_{9/2}$ and $f_{7/2}$ neutron orbitals play a pivotal role in the character of excitations in these nuclei.

This work reports measurements of the excited states in the transitional nuclei ^{161}W and ^{162}W identified using the selective recoil-decay tagging technique. The level scheme of ^{162}W has been extended and reveals a structure characteristic of *quasi*-collective excitations. The underlying configurations are discussed in terms of the cranked shell model. Prior to this work only the α decay of ^{161}W was known. This thesis reports the first identification of the level scheme of excited states in ^{161}W to high spin. The level scheme of ^{161}W can be interpreted in terms of multi-particle non-collective excitations. This indicates a threshold for the onset of collectivity in the neutron-deficient tungsten isotopes occurring at ^{162}W.

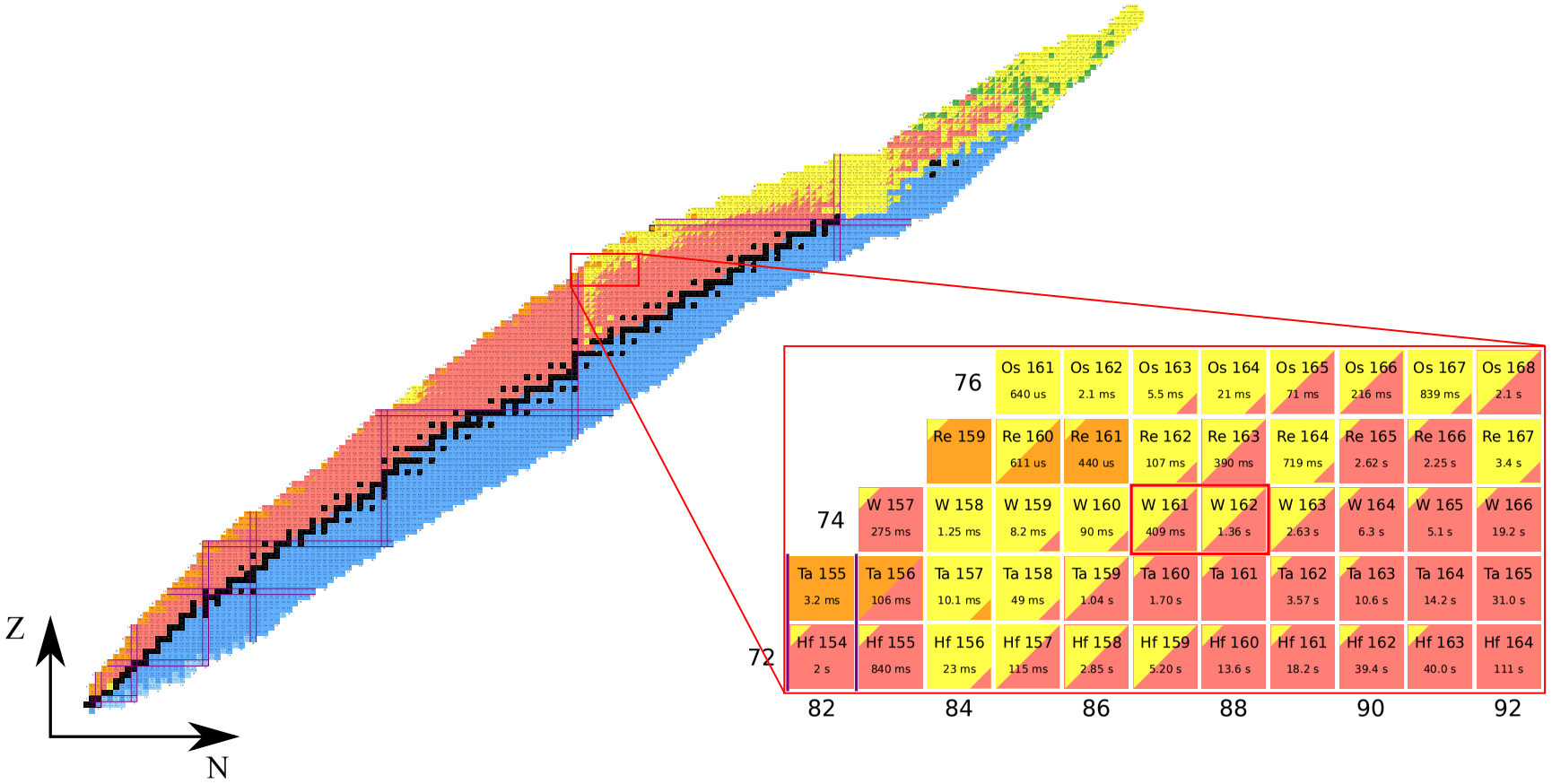

Figure 1: All known nuclei labelled with their decay modes: α-decay (yellow), $\beta+$ decay/EC (red), $\beta-$decay (blue), fission (green), proton or double proton decay (orange) and neutron or double neutron decay (light blue). Stable nuclei are shown in black. Secondary decays are indicated by triangles in the top left corner, a small triangle indicates branching ratios of less than 5% and large triangles are $< 5\%$. Purple lines bound magic numbers or "closed shells". The expanded region contains nuclides in the neutron-region above the N=82 shell closure and close to the proton drip line. Highlighted are the nuclei ^{161}W and ^{162}W.

Chapter 1

Concepts in Nuclear Structure

1.1 The Liquid Drop Model

The liquid drop model describes the nucleus as an incompressible macroscopic drop of charged fluid held together by short-range forces between nucleons giving it a constant mass-independent density [E29]. This model can be used to describe a number of bulk properties of the nucleus, such as the binding energy. The observation that the mass of a nucleus is smaller than the sum of its constituent nucleons led to the proposal of binding energy, dependent on the proton number Z, and the neutron number N such that

$$B(A,Z) = [M(A,Z) - ZM_H - NM_n]c^2, \tag{1.1}$$

and may be described by the semi-empirical mass formula

$$B(A,Z) = a_v A + a_s A^{2/3} + a_c \frac{Z(Z-1)}{A^{1/3}} + a_a \frac{(A-2Z)^2}{A} \pm \delta, \tag{1.2}$$

where a_v is the volume term, a_s is the surface term, a_c is the Coulomb term, a_a is the asymmetry term and δ is given by $(-) + a_p A^{-1/2}$ for doubly (odd) even nuclei

where a_p is the pairing term. For a nucleus of odd mass $\delta = 0$. The values, origins and contributions of each of these are discussed further in [Hey04] and [Kra88].

The difference in binding energy between two systems differing by one proton or neutron allow the separation energy of an individual nucleon to be defined as follows

$$\begin{aligned} S_p(A,Z) &= B(A,Z) - B(A-1,Z-1), \\ S_n(A,Z) &= B(A,Z) - B(A-1,Z), \end{aligned} \tag{1.3}$$

for a proton and neutron, respectively. For nuclei that are extremely neutron or proton rich these separation energies can fall below zero so that these nucleons become unbound. These limits are known as the drip lines. The effect of the Coulomb barrier in heavy neutron-deficient nuclei is the smearing of the proton drip line so that there may be more than one proton-emitting isotope for a given element. This means that in some cases where the Coulomb barrier is high several proton-emitting nuclei may exist for a measurable time, making spectroscopy beyond the proton drip line a possibility.

Although the liquid drop model predicts binding energies reasonably well, there are deviations at certain nucleon numbers. These *magic numbers* of nucleons have values of binding energy that vary from those predicted and appear to be much more tightly bound. This occurs due to shell effects and can only be described when contributions from individual nucleons are taken into account.

1.2 The Nuclear Shell Model

In order to account for the shell effects observed at magic numbers (N,Z=2, 8, 20, 28, 50, 82 and 126 for neutrons) such as the sharp discontinuities in binding energies at these numbers, we need to consider each nucleon contributing to the system.

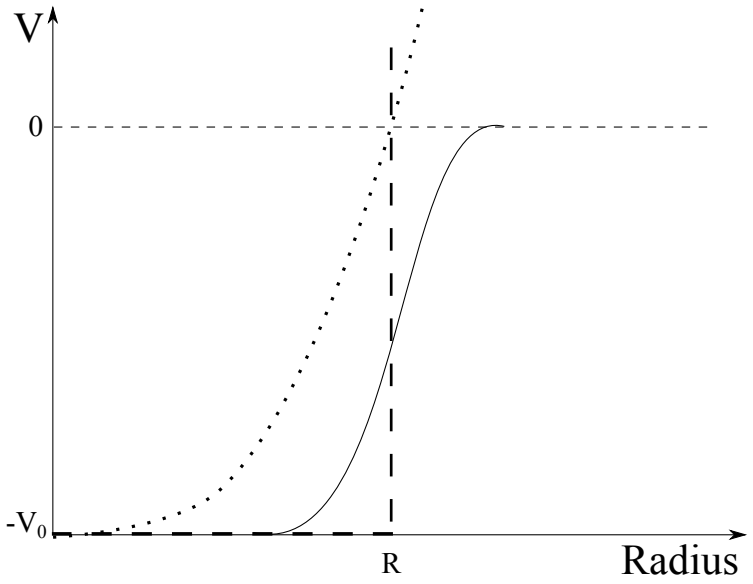

Figure 1.1: Three theoretical potentials of the nuclear mean field, The square well potential shown by dashed line, the Harmonic oscillator potential by the dotted line, and the Woods-Saxon potential by the solid line. R signifies the nuclear radius.

Analogous to the idea of shells in atomic theory, we imagine shells of neutrons and protons of discrete energies within a common potential, or *mean field*, created by the short range interactions of all other nucleons. The mean field is created by A nucleons moving with a given kinetic energy ($\overrightarrow{p_i^2}/2m_i$) and interacting via the two-body interactions, $V(i,j)$. The Hamiltonian for a particle i interacting with particles j will then be defined as

$$H = T + V = \sum_{i=1}^{A} \overrightarrow{p_i^2}/2m_i + \sum_{i<j=1}^{A} V(\overrightarrow{r_i}.\overrightarrow{r_j}), \tag{1.4}$$

The potential $V(\overrightarrow{r_i}, \overrightarrow{r_j})$ represents only the strong nuclear force between two nucleons. This is because the Coulomb force between two protons is much weaker, and the potential experienced by neutrons and protons is the same, as evident by their common magic numbers. Choosing a suitable approximation of this mean field potential is essential in order to correctly predict the nuclear properties.

Figure 1.1 illustrates three of these hypothesised potentials; the square well potential, the harmonic oscillator potential and the Woods-Saxon potential [WS54]. The

square well potential is the simplest form for the nuclear potential although surprisingly robust it is not entirely realistic. The potential should not have a sharp edge if it is to closely resemble the nuclear charge or matter distribution, which falls smoothly to zero beyond the mean radius, R. It only correctly predicts three of the nuclear shell gaps, 2,8 and 20.

The harmonic oscillator described by

$$V_{HO}(r) = -V_0 + \frac{1}{2}m\omega^2 r^2, \tag{1.5}$$

does very smoothly with distance r from the centre of the nucleus, but beyond R increases up to infinity. It also has an angular momentum degeneracy. The harmonic oscillator benefits from being easy to calculate analytically. However, it still does not correctly predict the shell gaps but can be modified to more closely resemble the true form of the potential.

The short-range nature of the nuclear force provides justification for the first modification to this potential, the l^2 term. Provided a nucleus is large enough that nucleons at the centre are a greater separation from the nuclear surface than the range of the nuclear force then those nucleons at the centre should be surrounded uniformly on all sides. These nucleons are screened from asymmetric mass distributions at the boundary and should therefore feel no net force. An attractive l^2 term is used here for its effect of flattening the radial shape of the potential. This is equivalent to the screening of central nucleons from asymmetric surface distributions as high angular momentum, l, nucleons feel a stronger attractive interaction. It is these higher angular momentum particles that spend a larger fraction of their time at larger radii due to the centrifugal force. Single-particle levels produced by the harmonic oscillator potential plus an l^2 term are shown in Figure 1.2.

In 1949 Mayer [May50], and Haxel, Suess and Jensen [HJS49] showed that the inclusion of a spin-orbit potential gave the proper separation of subshells. The form

of the potential now becomes

$$V_{MHO}(r) = -V_0 + \frac{1}{2}m\omega^2 r^2 - \kappa\hbar\omega[2\hat{l}\cdot\hat{s} + \mu(l^2 - \langle l^2\rangle_N)], \tag{1.6}$$

where l and s are the orbital angular momentum and spin quantum numbers, respectively and κ and μ are adjustable parameters varying for each oscillator shell. From this point on it is appropriate to label the states with the total angular momentum $j = l + s$, where a single nucleon has $s = \pm\frac{1}{2}$. The total angular momentum j is now $j = l + \frac{1}{2}$ or $j = l - \frac{1}{2}$, except for $l = 0$ where only $j = \frac{1}{2}$ is permitted. Now for each given value of $l > 0$ there are two new levels, see Figure 1.2, with energy separation proportional to the value of $\langle l \cdot s\rangle$ for each state. This splitting results in the correct shell spacings given in Figure 1.2.

The Woods-Saxon potential is a convenient choice for the one-body potential. Its shape with parameters chosen for the best fit to single-particle energies and nuclear radii most closely follows that of the nuclear density distribution. The Woods-Saxon potential is described by

$$V_{WS}(r) = \frac{-V_0}{1 + e^{(r-R)/a}}, \tag{1.7}$$

where a is the skin thickness, or diffuseness. $V_0 \sim 50MeV$ is the well depth adjusted according to correct separation energies. The effect of the Woods-Saxon potential is to remove the l degeneracies of major shells seen in the harmonic oscillator potential. Although the Woods-Saxon potential is considered more realistic, the modified harmonic oscillator is used for its ability to calculate the solutions to wavefunctions analytically.

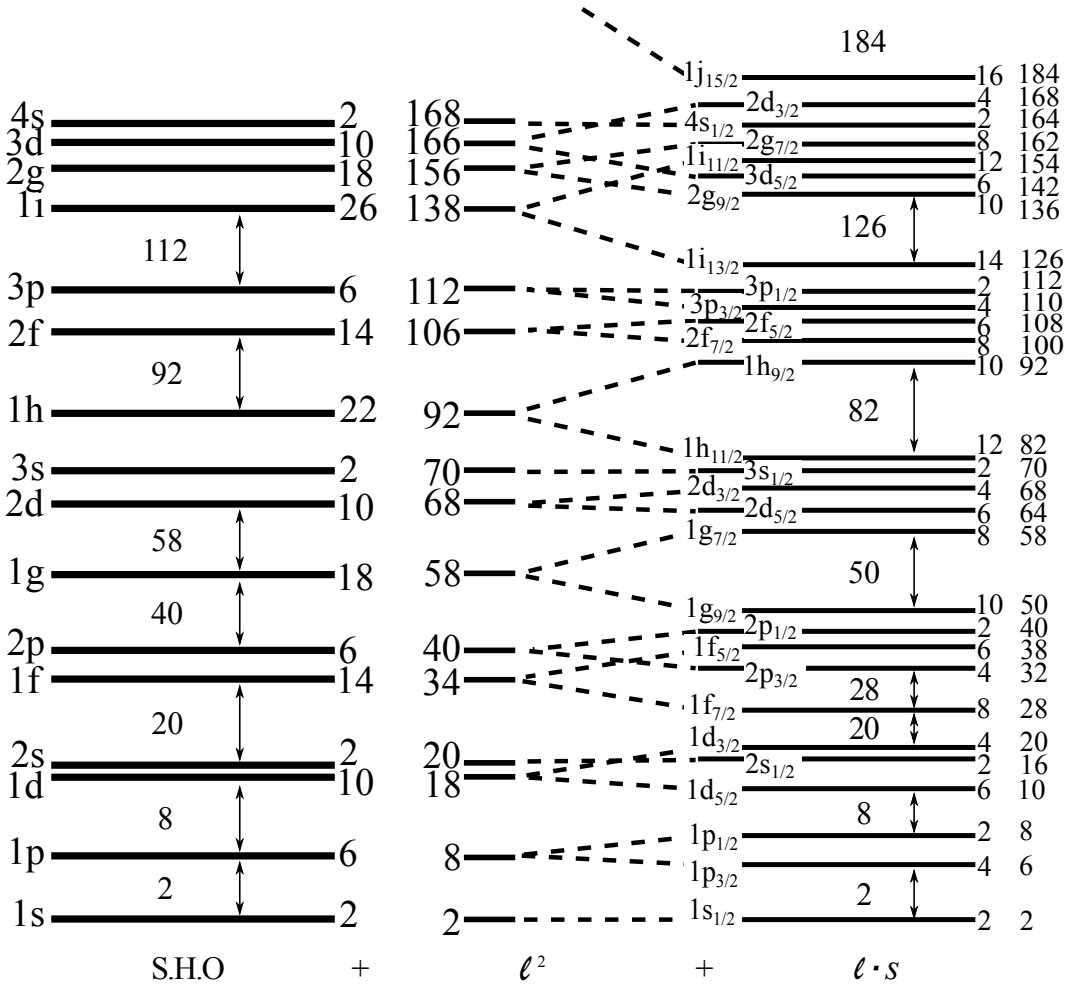

Figure 1.2: Single-particle energies as calculated for a single harmonic oscillator before and after correcting for the central radial flattening l^2 term and the spin-orbit $(l \cdot s)$ coupling. Magic numbers are now correctly reproduced. The spin orbit-interaction as seen on the right splits levels with $l > 0$ into 2 new levels, with an unmistakable effect on the predicted shell closures. Orbits are labeled as nl where n is the principle quantum number, or nl_j where $j = l \pm \frac{1}{2}$ for spin-orbit doublet levels.

1.3 Collective Motion in Nuclei

The shell model with its spherical average field does not always describe the effect of coherent motion of many valence nucleons well. Many nuclei far from closed shells have a non-spherical shape, which may display collective behaviour due to the residual interactions between nucleons. The collective characteristics of nuclei are described as either a vibration or rotation of the nucleus.

1.3.1 Nuclear Rotations

Rotational motion is only seen in those nuclei with non-spherical equilibrium shape, known as *deformed nuclei*. These most commonly occur in nuclei with nucleon numbers in the mid-shell. Nuclei with axially-symmetric deformations have one axis, the symmetry (z-)axis, longer or shorter than the other two, from which the angle θ is measured and their surface can be described by the radius vector

$$R(\theta,\phi) = R_0(1 + \alpha_{0,0} + \sum_{\lambda=1}^{\infty}\sum_{\mu=-\lambda}^{\lambda} \alpha_{\lambda,\mu}Y_{\lambda,\mu}(\theta,\phi)), \tag{1.8}$$

where R_0 is the radius of a sphere that would contain the same volume as the ellipsoid $\alpha_{0,0}$, introduced to conserve volume. The terms $\alpha_{\lambda,\mu}$ describe changes in nuclear volume, with λ defining the deformation type. In this work quadrupole deformations ($\lambda = 2$) are especially important. Quadrupole shapes are parametrised by the coefficients

$$\alpha_{2,2} \quad \alpha_{2,1} \quad \alpha_{2,0} \quad \alpha_{2,-1} \quad \alpha_{2,-2}. \tag{1.9}$$

These coefficients relate to deformation parameters β_2 and γ such that

$$\alpha_{2,2} = \frac{1}{\sqrt{2}}\beta_2 sin\gamma, \tag{1.10}$$

and

$$\alpha_{2,0} = \beta_2 cos\gamma \tag{1.11}$$

Simplifying equation 1.8 to

$$R(\theta, \phi) = R_{av}[1 + \beta Y_{20}(\theta, \phi)], \tag{1.12}$$

where Y_{20} is a quadrupole spherical harmonic. The *deformation parameter* β_2 is related to the eccentricity of the elliptical deformation by

$$\beta_2 = \frac{4}{3}\sqrt{\frac{\pi}{5}}\frac{\Delta R}{R_{av}}, \tag{1.13}$$

where ΔR is the difference between the semi-major and semi-minor axes of the ellipse.

Rotational nuclei are known to have common features. The kinetic energy of a rotating solid is $\frac{1}{2}\Im\omega^2$ where $\Im$ is the moment of inertia and ω is the rotational frequency. As a function of angular momentum $l = \Im\omega$, the energy is $l^2/2\Im$. Adopting the quantum mechanical value of l^2 and letting I represent the angular momentum quantum number gives

$$E = \frac{\hbar^2}{2\Im}I(I+1). \tag{1.14}$$

The nuclear excited states, dependent only on I for constant J, form a regular sequence known as a *rotational band*. In even-even nuclei, the ratio of the lowest states should therefore be constant with theoretical values of $E(4^+)/E(2^+)$ equal to 3.33 and $E(6^+)/E(2^+)$ as 7, which again are in striking agreement with systematics in the mass region $A \sim 160$.

Many deformed nuclei are described as axially symmetric; they have two minor axes which are the same length. Others, however, may have also have a deformation which causes all primary axes to be different lengths, these nuclei are described as axially asymmetric or triaxial, a property which is hard to determine experimentally. Deformation parameter γ is a measure of triaxiality.

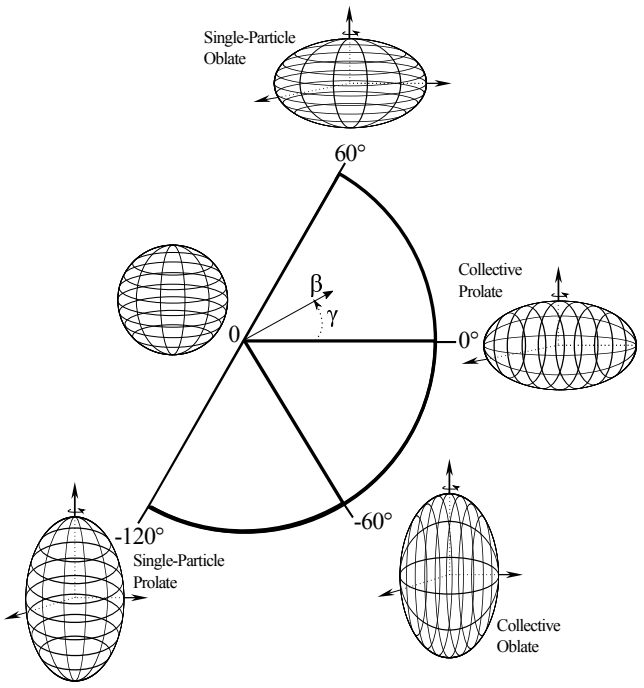

Figure 1.3: The Lund convention describing nuclear deformation.

The Lund Convention

The Lund convention, shown in Figure 1.3, provides a means of describing deviation from sphericity in terms of deformation parameters, β_2 the quadrupole deformation and γ the degree of triaxiality [A$^+$76]. Axially symmetric shapes appear at $\gamma = -120°, -60°, 0°$ or $60°$. These correspond to non-collective prolate, collective oblate, collective prolate and non-collective oblate, respectively. Triaxial shapes are therefore found at intermediate angles.

1.3.2 The Anisotropic Harmonic Oscillator (The Nilsson Model)

Although the modified harmonic oscillator discussed in section 1.2 successfully predicts the shell closures, the calculated levels are based on the assumption of the nuclear potential is spherical. As we now know many nuclei found far from closed shells with many valence nucleons have a permanently deformed shape [TFL49].

Nilsson created a successful model to describe the Hamiltonian governing the single-particle motion of nucleons in a deformed potential [Nil55]. A Nilsson Hamiltonian lifts the degeneracies of the spherical shell model and modifies single-particle energies as a function of deformation. The Nilsson Hamiltonian is described as

$$H_{Nil} = -\frac{\hbar^2}{2m}\Delta + \frac{1}{2}m(\omega_x^2 x^2 + \omega_y^2 y^2 + \omega_z^2 z^2) - \kappa\hbar\omega_0(2\hat{l}\cdot\hat{s} + \mu(\hat{l}^2 - \langle\hat{l}^2\rangle_N)), \quad (1.15)$$

This includes both a $l\cdot$s and $\hat{l}^2 - \langle\hat{l}^2\rangle$ term as described in section 1.2. This Hamiltonian treats the three axes as independent and for an axially symmetric shape we can introduce a deformation parameter ε ($\varepsilon \approx 0.95\beta$) under the following conditions

$$\omega_x = \mathring{\omega}\frac{R_0}{a_x}..., \quad (1.16)$$

ensuring each of the three frequencies is proportional to the inverse of the half-axis of the spheroid such that

$$\omega_x\omega_y\omega_z = \mathring{\omega}_0^3, \quad (1.17)$$

conserves volume. This gives the following

$$\omega_\perp^2 (= \omega_x^2 = \omega_y^2) = \omega_0^2(1 + \frac{2}{3}\varepsilon), \qquad \omega_z^2 = \omega_0^2(1 - \frac{4}{3}\varepsilon). \quad (1.18)$$

The deformed eigenstates can then be defined by the quantum numbers

$$\Omega^\pi[Nn_z\Lambda], \quad (1.19)$$

where

$$N = \text{Principal quantum number,} \tag{1.20}$$

$$n_z = \text{Number of oscillator quanta along the symmetry axis,} \tag{1.21}$$

$$\Lambda = \text{Projection of orbital angular momentum onto symmetry axis,} \tag{1.22}$$

$$\Omega = \text{Total angular momentum projection where} \quad \Omega = \Lambda + \Sigma = \Lambda \pm \frac{1}{2} \tag{1.23}$$

$$\pi = \text{Parity of the state} \quad (-1)^N \tag{1.24}$$

these are shown labeled in Figure 1.4.

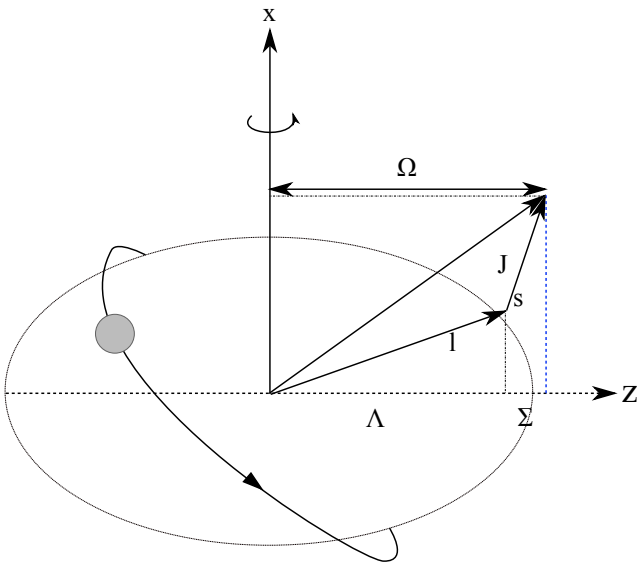

Figure 1.4: Coupling scheme showing the angular momenta $(\vec{l}, \vec{s})_{\vec{j}}$ and their projections $(\Lambda, \Sigma)_\Omega$ on the symmetry axis for a particle moving in an axially symmetric deformed potential

1.4 The Cranked Shell Model

The models discussed earlier considered collective motion as a macroscopic feature of the bulk of the nucleus. However collective and single-particle excitations cannot be decoupled. The cranked shell model provides a fully microscopic description of nuclear rotation. It considers independent particles moving in an average potential

generated by all the other nucleons, rotating with a fixed co-ordinate system. The theory was first derived by Inglis [Ing54] in 1954 in terms of the deformed single-particle potential and incorporates the effects of Coriolis and centrifugal forces on specific orbitals.

Considering a single-particle potential, U, rotating with respect to a rotational axis $\vec{\omega}$ with time dependence $U(\vec{r};t) = U(r,\theta,\phi-\omega t;0)$.

Transformation from the laboratory frame to the rotational frame occurs via the rotational operator $\hat{R}$,

$$\hat{R} = exp\left[-\frac{i\omega Jt}{\hbar}\right]. \tag{1.25}$$

The two wave-functions Ψ_{lab} and Ψ_{rot} can be related by

$$\Psi_{rot} = \hat{R}\Psi_{lab} = exp\left[-\frac{i\omega Jt}{\hbar}\right]\Psi_{lab}. \tag{1.26}$$

The Schrödinger equation in a rotating frame is

$$\hat{H}\Psi_{rot} = -i\hbar\frac{d\Psi_{rot}}{dt}, \tag{1.27}$$

by substitution this gives

$$\hat{H}_{rot} = \hat{H}_{lab} - \omega j_x, \tag{1.28}$$

where $\hat{H}_{lab}$ is the Hamiltonian in the laboratory system, describing the sum of the single-particle deformed potentials, and $-\omega j_x$ incorporates the Coriolis interaction. The eigenvalues of the single-particle cranking Hamiltonian, e' are known as Routhians and are defined as

$$e' = \langle u|\hat{H}_{rot}|u\rangle = \langle u|\hat{H}_{lab}|u\rangle - \omega\langle u|j_x|u\rangle, \tag{1.29}$$

where

$$e' = e - \omega j_x, \tag{1.30}$$

where u are the eigenstates of the cranking Hamiltonian and e is the single-particle energy in the laboratory frame. The total energy in the rotating frame is then the sum of the energies of all unoccupied orbits plus their Coriolis contributions such that

$$E = \sum_u e'_u + \omega \sum_u \langle u|j_x|u\rangle, \tag{1.31}$$

and

$$I_x = \sum_u \langle u|j_x|u\rangle \approx I, \tag{1.32}$$

for higher spins, where I_x is the projection of the total angular momentum and $I_x \to I$. The slope of the Routhians are related to the component of the angular momentum along the x axis, i_x known as the single-particle alignment, such that

$$\frac{de'}{d\omega} = -\langle u|j_x|u\rangle \approx -i_x. \tag{1.33}$$

Single-particle energies are often presented in the form of quasiparticle Routhians. Quasiparticles are a linear combination of particle and hole occupation probabilities. For each single-particle level there are two quasiparticle levels symmetric about the Fermi surface. Quasiparticle Routhians are most often plotted as a function of rotational frequency $\hbar\omega$. The crossing frequency ω_c corresponds to the rotational frequency at which a pair of nucleons in time-reversed orbits are broken apart by the Coriolis force and aligned with the rotation of the core. This will result in the addition of a single-particle contribution to the angular momentum of the core.

1.4.1 Comparing the Model with Experimental Data

A large amount of angular momentum can be gained by collective motion in stable deformed nuclei. This collective band structure cannot always be the most favourable excitation energy for a given spin or 'yrast'. At high rotational frequencies alignment can occur and the strong Coriolis force will begin to break pairing correlations and other excited configurations may become more energetically favourable. A

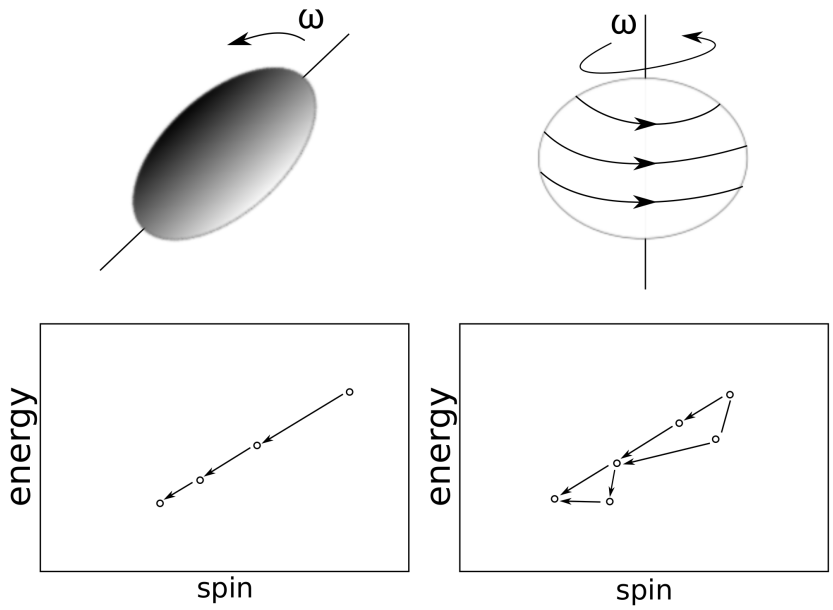

Figure 1.5: The two ways rotational motion is observed in near spherical nuclei. (a) Illustrates the way angular momentum can be accommodated by collective rotation. This results in a simple, regular yrast spectrum. (b) Conversely additional angular momentum can be acquired by the rearranging of individual nucleon orbits resulting in a more complex spectrum. Both are displayed through plots of transition energy against spin. (Image adapted from Bohr and Mottelson 1979)

sudden increase in experimental aligned angular momentum, is synonymous with the a band crossing described above. Figure 1.5 shows an example of this phenomenon.

In this way angular momentum can also be obtained via non-collective motion. The alignment of individual nuclear orbits along the nuclear symmetry axis contributes to the total spin of the system. These alignments can create much more complicated spectra than the traditional rotational behaviour.

There are three types of moment of inertia used to describe high-spin rotational structures, static ($\Im^{(0)}$), kinematic ($\Im^{(1)}$) and dynamic ($\Im^{(2)}$). The static moment of inertia is defined by a simple relation,

$$E = \frac{\hbar^2}{2\Im^{(0)}} I(I+1). \tag{1.34}$$

The kinematic moment of inertia is given by

$$\frac{\hbar I}{\omega} = \Im^{(1)} = I\hbar^2 \left(\frac{dE}{dI}\right)^{-1}, \tag{1.35}$$

and the dynamic moment of inertia

$$\Im^{(2)} = I\hbar^2 \left(\frac{d^2E}{d^2I}\right)^{-1} = \hbar\frac{dI}{d\omega}. \tag{1.36}$$

It is useful for determining intrinsic structure and assigning configurations to plot level scheme parameters as a function of rotational frequency, ie. the Routhians, e' versus rotational frequency, $\hbar\omega$ [BFM86]. From equation 1.35 the rotational frequency is defined as

$$\hbar\omega = \frac{dE(I)}{dI_x}, \tag{1.37}$$

and can be calculated from γ-ray transitions by

$$\hbar\omega = \frac{E(I_{x_2}) - E(I_{x_1})}{I_{x_2} - I_{x_1}}. \tag{1.38}$$

in the case of a rotational band, made up of a cascade of E2 transitions this can be simplified to

$$\hbar\omega = \frac{E_\gamma}{2}. \tag{1.39}$$

The experimental aligned angular momentum I_x represents the component of the angular momentum perpendicular to the symmetry axis z, given by

$$I_x = \sqrt{I(I+1)^2 - K^2}, \tag{1.40}$$

where K is the projection of angular momentum onto the symmetry axis.

Often when comparing experimental alignment gains to predictions from the cranked shell model it is helpful to subtract a rotational reference. The most commonly used reference alignment makes use of the Harris Parameters [Har64] J_0 and J_1 defined

by

$$I_{ref} = (J_0 + \omega^2 J_1)\omega. \tag{1.41}$$

Some care must be taken when using such approximations in triaxial nuclei, as K is no longer considered a good quantum number. In this work I_i as a function of E_γ is used. This fulfils a similar function to the rotational alignments as a function of rotational frequency, while removing the dependence K.

Chapter 2

Nuclear Decay Processes

Radioactive decay occurs from both naturally unstable nuclei and as a result of those produced in nuclear reactions. The most common forms of radioactive decay seen are β-decay (a weak interaction decay process) and α-decay (a strong interaction decay process). Electromagnetic decays such as γ decay and internal conversion can also occur. These are known as ionising radiations and the transfer of energy in matter is what enables their detection and forms the basis of spectroscopy.

2.1 Gamma-ray Transitions

Following radioactive decay by β emission or a nuclear reaction most resultant nuclei are left in an excited state. This excited state means that the nucleus has surplus angular momentum and energy and in order to return to the ground state γ rays may be emitted to carry away this excess. Gamma-ray spectroscopy is relatively easy compared to other decay processes due to negligible losses in air and can be accomplished at high resolution using detectors comprised of semiconducting materials with small band-gaps, such as germanium. Due to the properties of γ rays

they have proved useful for probing the structure of a nucleus, their energy being a direct consequence of the decay from a initial to final state.

Conservation of energy, angular momentum and parity when emitting γ rays creates a need for selection rules that determine the properties of the emitted rays. If we consider a γ transition, like that shown in Figure 2.1, the energy of the γ ray is considered equal to the difference in energy between the initial and final state such that

$$E_\gamma = E_i - E_f, \tag{2.1}$$

minus a negligible fraction, which is transferred to the nucleus to conserve momentum. Conservation of angular momentum requires that the total initial angular momentum, I_i must equal the total final angular momentum. In vector terms this is

$$\vec{I_i} = \vec{L} + \vec{I_f}. \tag{2.2}$$

As I_i, I_f and L must form a closed vector triangle this imposes restrictions on the possible value of the multipolarity L of the emitted γ ray. These are given by

$$|I_i - I_f| \leq L \leq I_i + I_f. \tag{2.3}$$

For example if there is a γ transition from $I_i = \frac{3}{2}$ to $I_f = \frac{5}{2}$ the possible values of L will be 1,2,3 and 4, meaning there will be a competing mixture of dipole, quadrupole, octupole and hexadecapole radiation. The lower order multipoles will usually be most favoured. The electric or magnetic nature of the photon is determined by the relative parity of the levels involved. A change in parity ($\Delta\pi$) signifies an odd parity in the radiation field and vice versa. The parity of the radiation field is given by

$$\begin{aligned} \pi(ML) &= (-1)^{L+1}, \\ \pi(EL) &= (-1)^{L}. \end{aligned} \tag{2.4}$$

It should be noticed that electric and magnetic multipoles of the same order will

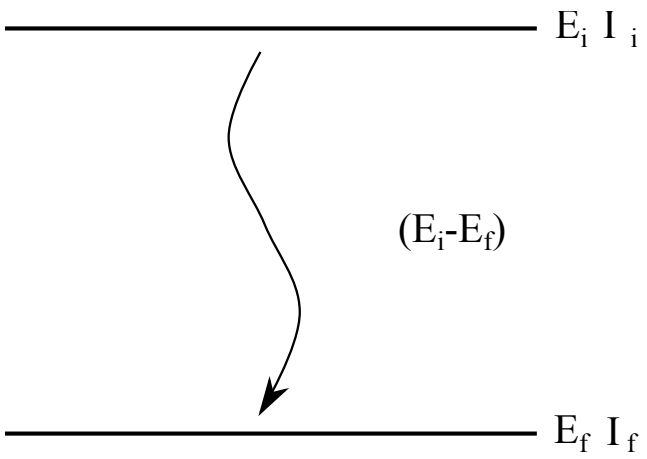

Figure 2.1: Schematic of γ decay, from an initial excited state with energy E_i and angular momentum I_i to a second less excited state.

always have opposite parity. If we consider only the lowest multipolarities, for decays between states of the same parity we expect to observe M1 or E2 transitions. Where there is a change in parity we would expect E1 or M2 transitions. As transition probabilities dictate that higher multipolarities are slower, as are magnetic transitions of the same order, we expect to observe only E2, M1 or E1 transitions in this work.

2.2 Alpha Decay

The spontaneous emission of an α-particle (or ^{4}He nucleus) from a parent nucleus is described as follows

$$ {}^{A}_{Z}X_N \rightarrow {}^{A-4}_{Z-2}X'_{N-2} + \alpha + Q \tag{2.5} $$

The net energy released by the decay is called the Q-value, which corresponds to the kinetic energy of the daughter nucleus and alpha particle system. From conservation of energy this is given by

$$ \begin{aligned} m_x c^2 &= m_{x'} c^2 + T_{x'} + m_\alpha c^2 + T_\alpha \\ (m_x - m_{x'} - m_\alpha)c^2 &= T_{x'} + T_\alpha = Q \end{aligned} \tag{2.6} $$

and the decay will occur spontaneously only when $Q > 0$. Conservation of linear momentum requires that both x' and α have equal and opposite momenta. Using non-relativistic kinematics the kinetic energy can be found as

$$T_\alpha = \frac{Q}{1 + m_\alpha/m_{x'}}, \tag{2.7}$$

as we recall x' typically represents a heavy nucleus and the mass ratio is very small, with $A >> 4$,

$$T_\alpha = \frac{Q}{1 + 4/(A-4)}, \tag{2.8}$$

which reduces to

$$T_\alpha = \frac{Q}{1 + 4/A}. \tag{2.9}$$

Alpha emission is a quantum tunnelling effect [Gam28, GC28]. Figure 2.2 shows the potential energy between the α particle and the daughter nucleus as a function of their separation. The dotted horizontal line represents the total energy of the alpha particle and the radius a is taken as the sum of the two radii. The schematic shows three regions of interest. At $r < a$, the α particle remains free to move within the nucleus but classically unable to escape. Further, $a < r < b$ this region is the potential barrier, where the potential energy is greater than Q, classically the α particle cannot enter this region from either direction. Finally, $r > b$, outside the nucleus.

The barrier height, B (not labelled) at $r = a$ is given by

$$B = \frac{1}{4\pi\epsilon_0}\frac{zZ'e^2}{a}, \tag{2.10}$$

where the alpha particle and nucleus have charges ze and $Z'e$, respectively. The radius at which the α particle leaves the nucleus, b comes simply from the equality of the particle's energy and the potential energy,

$$B = \frac{1}{4\pi\epsilon_0}\frac{zZ'e^2}{Q}. \tag{2.11}$$

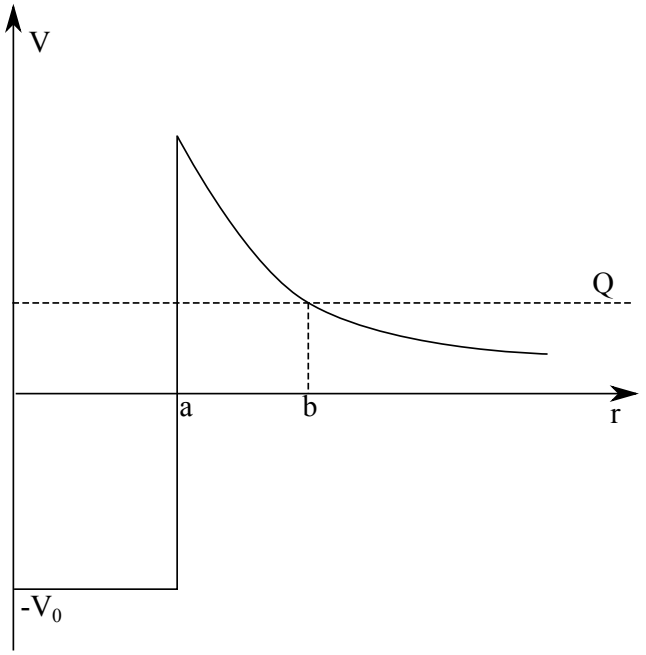

Figure 2.2: Potential energy of an alpha particle and the daughter nucleus, as α tunnels through the coulomb barrier, as a function of their separation r.

In 1928 the quantum theory for α decay was developed by Gamow [Gam28], giving a solution to the probability to penetrate the Coulomb barrier,

$$P = e^{-2G}, \tag{2.12}$$

where the Gamow factor G, is given by

$$G = \sqrt{\frac{2m}{\hbar^2}} \int_a^b \sqrt{V(r) - Q} dr, \tag{2.13}$$

which can be evaluated as

$$G = \sqrt{\frac{2m}{\hbar^2 Q}} \frac{zZ'e^2}{4\pi\epsilon_0} [arccos\sqrt{x} - \sqrt{x(1-x)}], \tag{2.14}$$

where $x = a/b = Q/B$. The quantum mechanical solution for the half-life of the decay is then

$$t_{1/2} = 0.693 \frac{a}{c} \sqrt{\frac{mc^2}{2(V_0 + Q)}} exp\left[2\sqrt{\frac{2mc^2}{(\hbar c)^2 Q}} \frac{zZ'e^2}{4\pi\epsilon_0} \left(\frac{\pi}{2} - 2\sqrt{\frac{Q}{B}}\right)\right]. \tag{2.15}$$

This demonstrates that the α-decay half-life is sensitive to the size and shape of the potential barrier.

Many heavy nuclei decay spontaneously by the emission of an α particle. The characteristic, well-defined energy and half-life of an α decay makes them ideal for selective tagging techniques in γ-spectroscopy. Alpha decay is also in itself a useful process for studying the internal structure of a nucleus.

Chapter 3

Experimental Methodology and Apparatus

The experiments discussed in this work were carried out at the University of Jyväskylä, Finland using the Jurogam array coupled to the Recoil Ion Transport unit (RITU) and GREAT spectrometer. This chapter is concerned with the heavy-ion fusion-evaporation reaction mechanism for synthesising exotic nuclei in an excited state, as well as the apparatus used for the detection of radiation emitted from the recoiling nucleus. The techniques used to sort and analyse the resulting data are also covered.

3.1 Heavy-Ion Fusion-Evaporation Reactions

The isotopes of interest in this study are far from stability and do not occur in nature. The lightest stable tungsten isotope has mass $A = 180$, which is eighteen neutrons heavier than ^{162}W. Fusion-evaporation reactions are the most commonly employed mechanism for producing neutron-deficient nuclei. Fusion-evaporation is a process in which a beam is incident on a target such that the beam and target nuclei will fuse provided the beam is accelerated to an energy high enough to overcome the

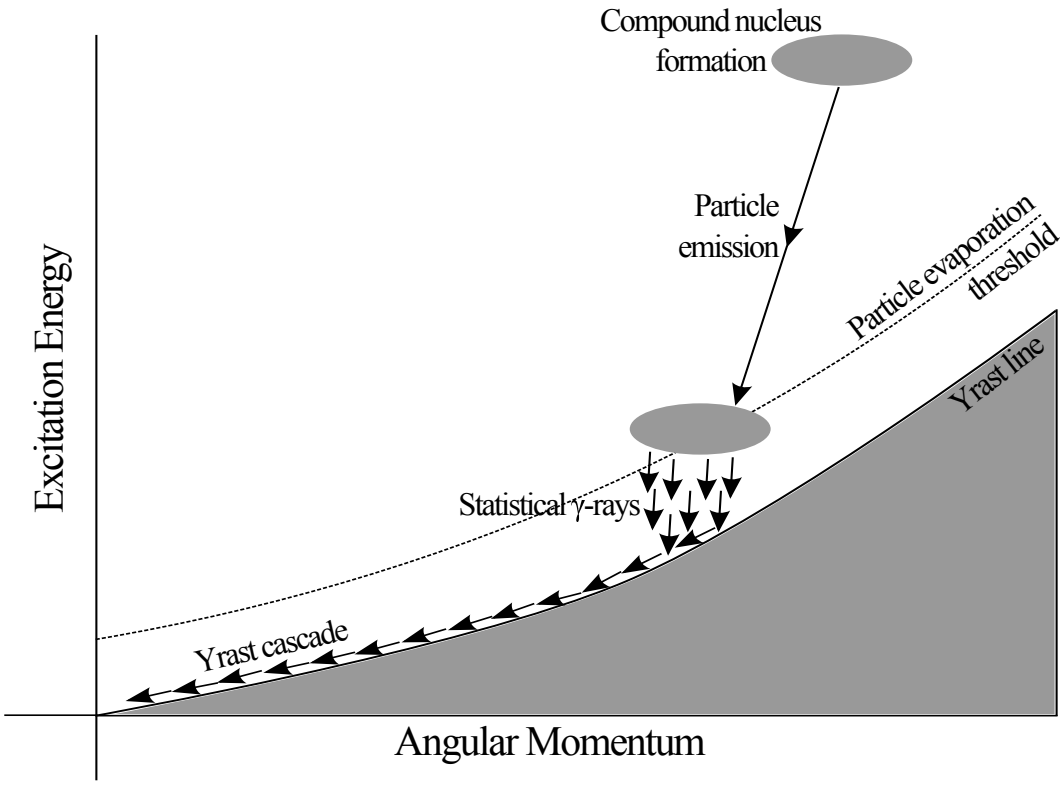

Figure 3.1: Schematic diagram illustrating the decay of a compound nucleus formed via the heavy-ion fusion evaporation process.

Coulomb barrier. The product nucleus will form a heavy, excited, neutron-deficient nucleus, the high angular momentum and energy cause the nucleus to evaporate neutrons, protons and α particles. These evaporated particles carry a fraction of the excess energy and angular momentum away with them. These evaporated particles, however, do not carry away much of the excess angular momentum. Once the excitation energy of the nucleus drops below the particle emission threshold the 'cooling' process will continue via the emission of statistical γ rays. These statistical γ rays remove a large amount of energy but very little angular momentum. Once close to the yrast line, defined as the lowest-energy state for a given angular momentum, the nucleus will emit discrete cascades of γ rays that dissipate angular momentum. Eventually the nucleus decays to the ground state. This process is illustrated in figure 3.1.

3.2 Gamma-ray Spectroscopy

3.2.1 Germanium Semiconductor Detectors

In order to measure the discrete energies of γ rays emitted from a residual nucleus, detectors with a high energy resolution and reasonable efficiency are required. For this reason Hyper-Pure Germanium (HPGe) detectors are most frequently used. HPGe, a type of semiconductor detector, works on the principle that interactions between radiation and the detector material will excite electrons from the valence band into the conductance band. This will leave behind holes in the valence band, the liberated charges will then be swept towards electrodes when a voltage is applied. These detectors act as a large $p-n$ junction, which under reverse bias forms a large electrically neutral region between the free electron doped (n+) and free hole doped (p+) materials. When radiation interacts within this region electron-hole pairs are formed. Electrons will flow towards the positive potential, while the holes towards the negative. This charge can be collected and converted to an output by a pre-amplifier. The number of electron-hole pairs formed and therefore the size of the output voltage is proportional to the energy of the incident γ-ray energy.

The HPGe detectors used in this experiment are in the bulletised coaxial configuration. This configuration consists of a cylindrical crystal with rounded front corners, to remove the low-field regions that occur at sharp corners of a crystal. The electrical contacts are configured so that the p+ contact covers the outer surface of the crystal and the n+ contact is in the inner cavity accessed through the back of the crystal. Figure 3.2 shows a schematic of a typical HPGe detector set-up, including escape suppression shielding.

The detectors are cooled to 77 K using liquid nitrogen using a cold finger from the dewar. This cooling is necessary to reduce the noise produced by thermal excitations as the band gap in germanium is very small ($\sim 0.68\ eV$). Germanium detectors have

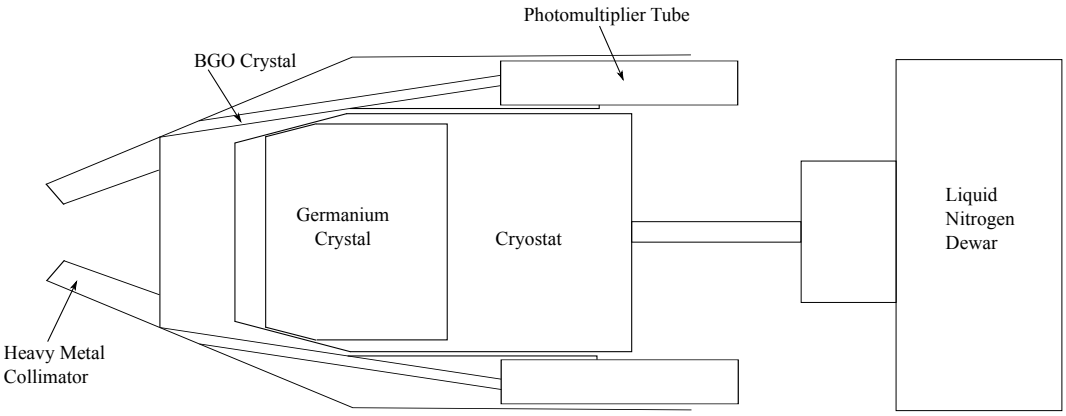

Figure 3.2: A schematic illustration of a Eurogam phase 1 escape suppressed germanium detector.

excellent energy resolution as the energy required to produce an electron-hole pair is only around 3 eV compared to an ionisation energy of 25 eV in NaI. This means that many more electron-hole pairs are formed for any given γ-ray interaction thereby reducing statistical fluctuations.

3.2.2 Compton Suppression

As we can see from figure 3.2, the HPGe crystal is surrounded by Bismuth Germanate (BGO), scintillator detectors. When a γ ray interacts with a medium via the photoelectric effect, its full energy is deposited. However, most γ rays at the energies seen in this work (200 keV $\leq E_\gamma \leq$ 1200 keV) will interact by Compton scattering. Compton scattering occurs when an incident γ ray scattering off an outer atomic electron transfers some of its energy to the electron according to the relation

$$E'_\gamma = \frac{E_\gamma}{1 + \frac{E_\gamma}{m_0 c^2} cos\theta}, \tag{3.1}$$

where E'_γ is the energy of the scattered photon, E_γ is the energy of the incident photon, m_0 is the rest energy of an electron and θ is the scattering angle. Scattered γ rays can then escape the detector volume having only imparted a fraction of their

energy, resulting in an unwanted continuum background that reduces the peak-to-total ratio.

BGO detectors are used as Compton suppression shields by operating in an anti-coincidence mode with the HPGe detectors. This means that any γ ray that has escaped the detector volume and is subsequently detected in the BGO will be removed from the data stream. BGO is used for its high efficiency due to its high atomic number Z. The ratio of counts in the full energy peak to those counts included in both the peak and background below (peak-to-total) is improved from around 0.2 for unsuppressed detectors, to 0.5-0.6 with escape suppression [BS96].

3.2.3 Large Detector Arrays

Nuclei produced via fusion-evaporation reactions are usually in a state of high angular momentum. This leads to the emission of a cascade of γ rays. The best way to analyse these decays is using a large array of hyper-pure Germanium (HPGe) detectors, which are designed to cover as much of the 4π solid angle as possible. The best way to gain an indication of the ability of a detector array to collect quality spectra is using the resolving power [NBF94], defined as

$$R = \left(\frac{SE_\gamma}{\Delta E_\gamma} PT \right), \tag{3.2}$$

where ΔE is the FWHM (full-width at half-maximum) of the γ-ray peak in the final spectrum, SE_γ is the average energy separation in a cascade of γ rays and PT is the Peak-to-Total ratio. As SE_γ is dependent only on the structure of the nucleus the resolving power can only be improved by improving the resolution or the peak to total ratio. Gamma rays collected in high fold (n) coincidences improve the peak to total ratio such that $R \propto PT^n$.

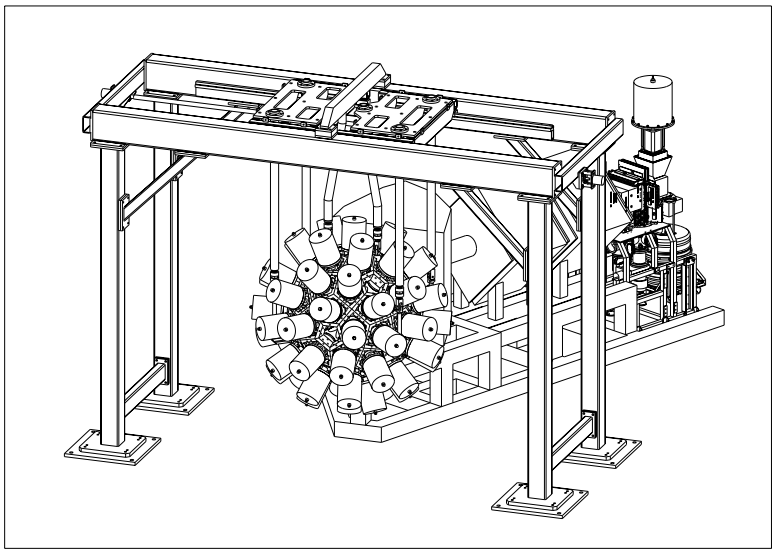

Figure 3.3: Line drawing of Jurogam array, used in conjunction with RITU and GREAT. Coutesy of Dave Seddon.

3.3 The Jurogam Spectrometer Array

The Jurogam spectrometer array is the primary tool for performing γ spectroscopy in this work. The array comprises 43 HPGe Compton-suppressed coaxial detectors [G$^+$05, Nol90]. Jurogam is a composite array made up of both Eurogam phase 1 and GASP type detectors [Baz92]. The germanium crystals have diameter 70mm, length 75mm and tapered over the front 3cm [B$^+$92]. With the full working array Jurogam has a total photopeak efficiency of 4.2% at 1.33 MeV. The array is arranged in six rings of detectors as listed in table 3.1. Jurogam may be used in conjunction with a gas-filled separator and focal-plane spectrometers described in section 3.6 and shown in figure 3.3.

Array Position	Ring Number	θ°	ϕ°
1	1	157.6	0
2		157.6	72
3		157.6	144
4		157.6	216
5		157.6	288
6	2	133.57	18
7		133.57	54
8		133.57	90
9		133.57	126
10		133.57	162
11		133.57	198
12		133.57	234
13		133.57	270
14		133.57	306
15		133.57	342
16	3	107.94	13.6
17		107.94	58.6
18		107.94	85.6
19		107.94	130.4
20		107.94	157.6
21		107.94	202.4
22		107.94	229.4
23		107.94	274.4
24		107.94	304
25		107.94	344
26	4	94.16	36
27		94.16	108
28		94.16	180
29		94.16	252
30		94.16	324
31	5	85.84	0
32		85.84	72
33		85.84	144
34		85.84	216
35		85.84	288
36	6	72.05	22.4
37		72.05	49.9
38		72.05	94.4
39		72.05	121.6
40 (Empty)		72.05	166.4
41 (Empty)		72.05	193.6
42		72.05	238.1
43		72.05	265.6
44		72.05	310.4
45		72.05	337.6

Table 3.1: Jurogam array specifications, angle θ is measured with respect to the beam axis and angle ϕ is defined for $\phi = 0^\circ$ as vertically upwards increasing clockwise when viewed from upstream.

3.4 Recoil Ion Transport Unit

RITU is a gas-filled magnetic separator used to transport heavy-ion evaporation residues from the target position to the focal plane detector system [L$^+$95]. RITU is essential for separating fusion products from fission fragments and unreacted beam.

Gas-filled separators are most commonly used in the transport of heavy fusion products. Collisions between recoiling reaction products and gas atoms allows an average charge state to be achieved for all species focusing them in a common trajectory. The relationship between the magnetic rigidity $B\rho$ and the average charge state q of an ion traversing a magnetic field can be expressed such that

$$B\rho = mv/qe, \tag{3.3}$$

where e is the charge on an electron and mv is the momentum of the reaction product. Bohr [Boh40] proposed a simple assumption, that all the electrons with orbital velocities less than v will be stripped. Using the Thomas-Fermi atomic model the average charge state for primary ions can be estimated as

$$q = \left(\frac{v}{v_0}\right) Z^{\alpha}, \tag{3.4}$$

which is valid in the velocity region $1 < v/v_0 < Z^{2/3}$ with $\alpha = 1/3$ and the Bohr velocity $v_0 = 2.19 \times 10^6\ m/s$. This then gives the approximation

$$B\rho = 0.227 \frac{A}{Z^{\alpha}}\ \text{Tm}, \tag{3.5}$$

where A and Z are the atomic mass and proton numbers, respectively. Formula 3.3 can be used as a rough estimate of the degree of separation between fission products or unreacted beam and the fusion evaporation residues when ρ is taken as the radius of their trajectory [GYL$^+$88].

From this we can deduce the two most important properties of a gas-filled separator: the magnetic rigidity $B\rho$ of the ion is independent of both velocity and initial charge state. From equation 3.5 it is indicated that the best separation of fusion products from the unreacted beam would be achieved where there is the greatest difference between their values of $A/Z^{1/3}$. Thus the most efficient application of gas-filled separators is the separation of fusion evaporation residues from asymmetric reactions. Where total acceptance is concerned gas-filled separators are considered superior to vacuum separators due to their high charge and velocity acceptance. This high transmission efficiency comes at loss of charge state selectivity. RITU uses a combination of dipole (D) and quadrupole (Q) magnets arranged in a $Q_vDQ_hQ_v$ configuration, with a 4.7m flight path. This first quadrupole element is strongly vertically (v) focused illuminating the dipole entrance. RITU has a 30% higher angular acceptance than the standard DQQ design [L$^+$95] which means that transmission losses between RITU and the Jurogam germanium array is greatly reduced over other configurations. The remaining two quadrupole magnets are used for vertical and horizontal (h) focusing of the recoiling reaction products onto the GREAT focal-plane spectrometer. The separator chamber is filled with helium at a pressure of 1 mbar from the target to the focal plane, which is continuously circulated through the chamber. A differential pumping system is used to separate the helium gas from the high vacuum of the beam line.

3.5 The GREAT Spectrometer

The GREAT spectrometer is a collection of detectors designed for measuring the decay properties of fusion evaporation reaction products transported to the focal plane via a recoil separator - in this case RITU [P$^+$03]. GREAT can either be used as a stand-alone device for decay measurement, or when coupled with the Jurogam spectrometer and RITU, as it is used here, provides a selective tagger for γ rays detected at the target position. The GREAT design combines the use of silicon,

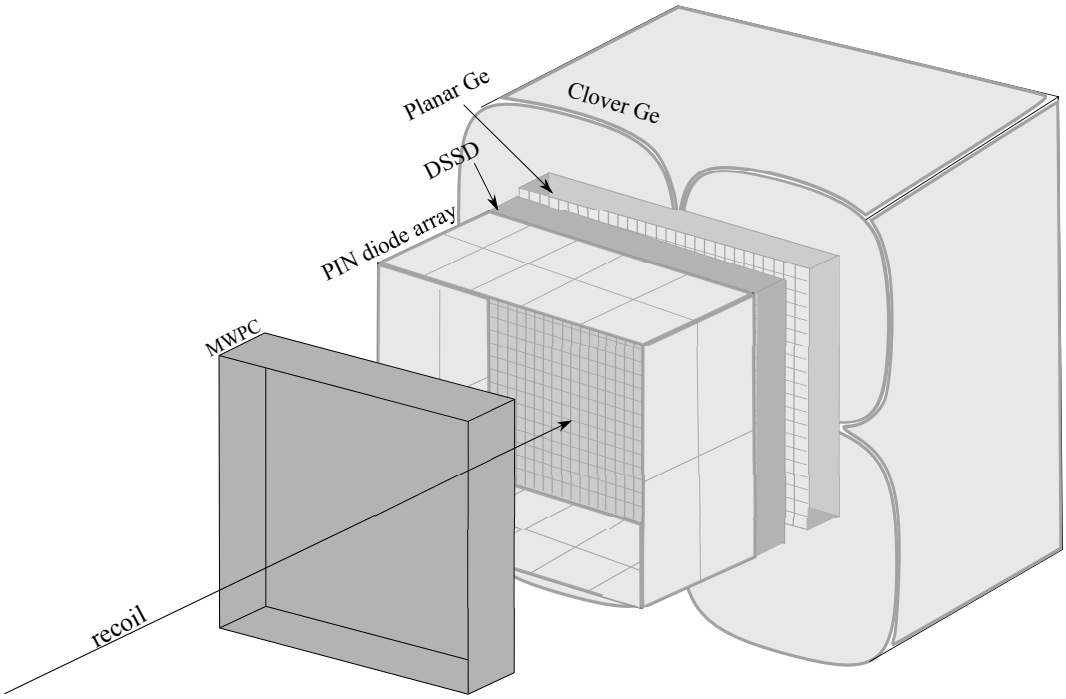

Figure 3.4: Schematic of the GREAT spectrometer.

germanium and gas detectors used in conjunction to detect the arrival of recoiling nuclei and their subsequent decays at the separator focal-plane.

GREAT comprises five distinct components, a multiwire proportional counter, an array of PIN diode detectors, double-sided silicon strip detectors (DSSD), a double-sided planar germanium strip detector and a segmented germanium clover detector. A schematic of the setup is shown in figure 3.4.

Multiwire Proportional Counter (MWPC)

The MWPC is a gas detector positioned at the entrance to GREAT. Its principal role is discriminating between scattered beam, recoils and their subsequent decays. The MWPC contains four wire planes in isobutane gas with mylar foils at the entrance and exit of the volume separating it from the low-pressure helium gas of RITU and the vacuum of the rest of the GREAT detector. The entrance to the detector has an aperture of 131_h mm $\times$ 50_v mm. Ions passing through the detector generate

energy loss, position and timing signals, which are shaped by commercial electronics systems and can be used to distinguish between reaction products and beam. The ions are next implanted into the DSSD. Here the MWPC is used as a veto as a signal in the DSSD that is not preceded by a signal in the MWPC can indicate the difference between a recoil implantation and its subsequent decay.

The double-sided silicon strip implantation detector

The transmitted reaction products are implanted into either one of two adjacent double-sided silicon strip detectors. The DSSDs are used to measure the energy of the implanted ions, as well as the energy of the protons, α particles and β particles emitted subsequently. The active area of each strip is 60 mm$\times$40 mm with a thickness of 300 μm. The strip pitch is 1 mm in both directions giving a position resolution similar to that of the MWPC and a total number of 4800 pixels. The DSSDs are mounted on a hollow block containing coolant that maintains a temperature of -20°C. The estimated recoil collection efficiency of this system is around 85% [P$^+$03].

The PIN diode detectors

The recoiling reaction products are implanted in the DSSD with a typical depth of 1-10 μm, which is not sufficient to prevent alpha particles and conversion electrons from escaping backwards relative to the beam direction. An array of 28 silicon PIN diodes is mounted in pairs in a box surrounding the perimeter of the DSSD to measure the energies of emerging conversion electrons. Each PIN diode has an active area of 28 mm$\times$28 mm with a thickness of 0.5 mm. This arrangement has an energy resolution of $\sim$ 5 keV and a geometric efficiency of $\sim$ 30% [P$^+$03].

The planar germanium detector

A planar germanium detector is positioned directly behind the DSSDs is to provide efficient detection of X-rays, low-energy γ-rays and high-energy β particles that have penetrated the DSSD. The crystal has an active area of 120 mm$\times$60 mm with a thickness of 15 mm. The strip pitch on each side is 5 mm giving position information used to allow events to be spatially correlated to decays in the silicon strip detectors. The detector has a thin beryllium entrance window and is positioned 10 mm downstream from the DSSD inside the vacuum chamber with its own cryostat.

The clover germanium detector

The clover detector comprises four germanium crystals each with four-fold electrical segmentation. Its purpose is to detect the higher energy γ rays that depopulate isomeric states. Each crystal has a 70 mm diameter before shaping and is 105 mm long. The crystals are tapered along the first 30 mm of their length. The clover detectors are positioned outside of the vacuum chamber and are surrounded by bismuth germanate suppression shields.

3.6 Recoil Decay Tagging

Fusion-evaporation reactions generally produce highly neutron-deficient compound nuclei. The reactions studied in this thesis produce compound nuclei close to the proton drip line. Cross sections for these reactions become very small in this region and the heavy-ion fusion evaporation process produces a large number of open reaction channels. Nuclear fission of heavy nuclei also has large cross section compared to fusion producing huge numbers of γ rays as the fission fragments de-excite. These simultaneous reactions create a large background which can obscure the γ-rays of interest. This makes γ-ray spectroscopy of neutron-deficient nuclei produced in this

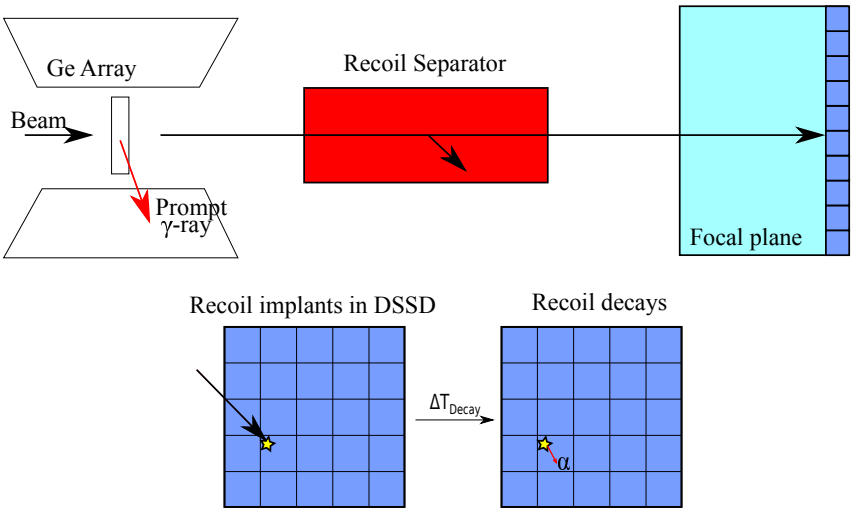

Figure 3.5: Schematic diagram showing the process that allows for recoil decay tagging.

way very difficult. However it is possible to study the γ-ray cascades of fusion evaporation residues via the selectivity provided by recoil separators and their focal-plane detector systems. The recoil decay tagging technique allows the study of reactions at the limit of what is experimentally acheivable, resulting in successful in-beam spectroscopy of nuclei with production cross sections as low as 10 nb [R$^+$10].

Many of the nuclei in this region decay by emitting α particles or protons with characteristic energies and decay times. These characteristic decay modes are ideal for applying a selective tag on the isotope of interest, reducing the background from other reaction channels. By separating and implanting recoiling fusion-evaporation reaction products into a silicon strip detector at the focal-plane of a separator, subsequent decays within the same pixel can be tagged provided they have the expected energy and occur within a set time period. This method is known as recoil decay tagging (RDT) [PWD$^+$95, SSH$^+$86], the apparatus used for this technique are described below and a simple schematic is shown in figure 3.5.

The process of RDT involves the nucleus of interest being produced via fusion-evaporation at the target where prompt γ rays are emitted and detected in the target spectrometer array. The nucleus then recoils with $^v/_c \sim$ 4% through a recoil

separator where it is separated from unreacted beam and focused onto the focal-plane detectors. The nucleus then traverses a gas detector and is implanted in a pixel of a double-sided silicon strip detector. At this point, distinctions can be made between recoils implanting in the focal plane and unreacted beam. Recoils due to their greater mass carry a greater charge and cause more ionisation in the gas detector than the beam. The velocity of heavy fusion products will also be lower than the light unreacted nuclei of the beam. These two factors are clear when a matrix of energy loss in the gas detector is plotted against time of flight, see figure 3.6. By requiring events to pass a 2D criterion on the silicon strip recoils can now be distinguished from unreacted beam.

Gamma rays detected at the target position may be correlated with those recoils detected in delayed coincidence at the focal plane due to time-stamps recorded for every event. Correlation of recoil events with prompt γ emissions at the target can be achieved by taking account of the time-of-flight of the recoil through RITU and ignoring all other γ rays produced outside this interval. Figure 3.7 shows a plot of time-of-flight between target and the silicon strip against the time-of-flight between the multiwire proportional counter and DSSD. A peak forms at the average flight time around which a two dimensional gate can be placed. The continuous background occurs due to the cyclotron periodicity, so many fusion-evaporation reactions may occur in the time it takes the recoil to reach the focal plane creating a large background.

Gamma spectra can now be recoil-correlated, meaning all γ rays must be in delayed coincidence with a recoil implantation. The comparison between raw γ-ray spectra and a recoil-correlated one can be seen in figures 3.8(a) and (b).

The unstable nucleus implanted in the focal plane will then decay via characteristic alpha decay, proton decay or isomer-delayed γ-ray emission. Decays are differentiated from recoil implantations by a lack of a coincident signal in the gas detector, since they originate solely within the DSSD pixel. By setting restrictions on the

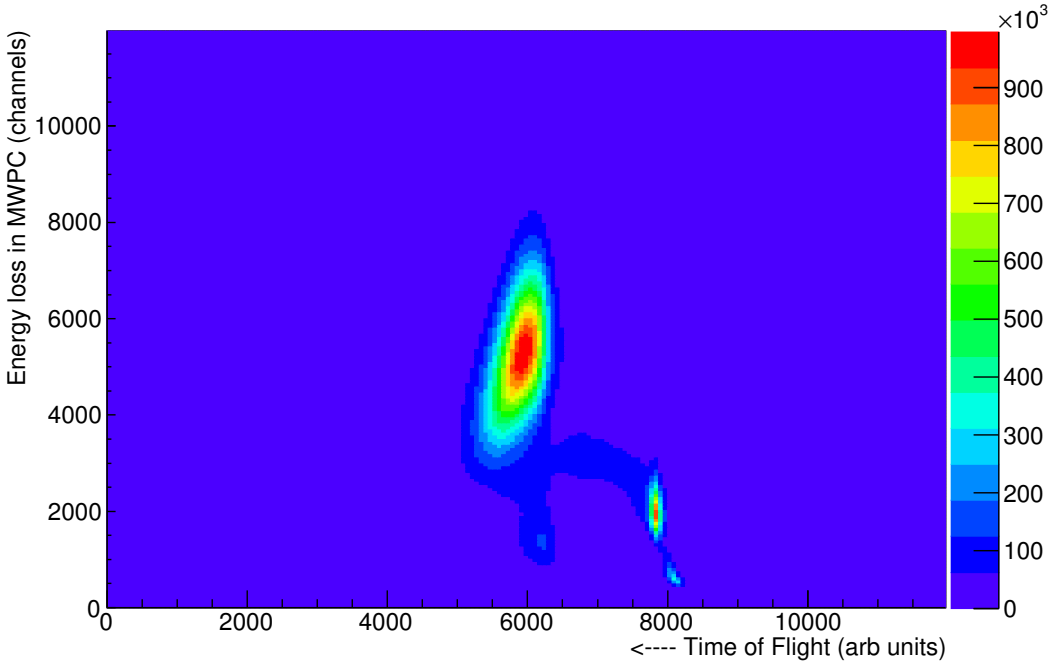

Figure 3.6: Two-dimensional plot showing energy loss in the MWPC versus time of flight. The larger peak is due to the recoils and the smaller belongs to the beam.

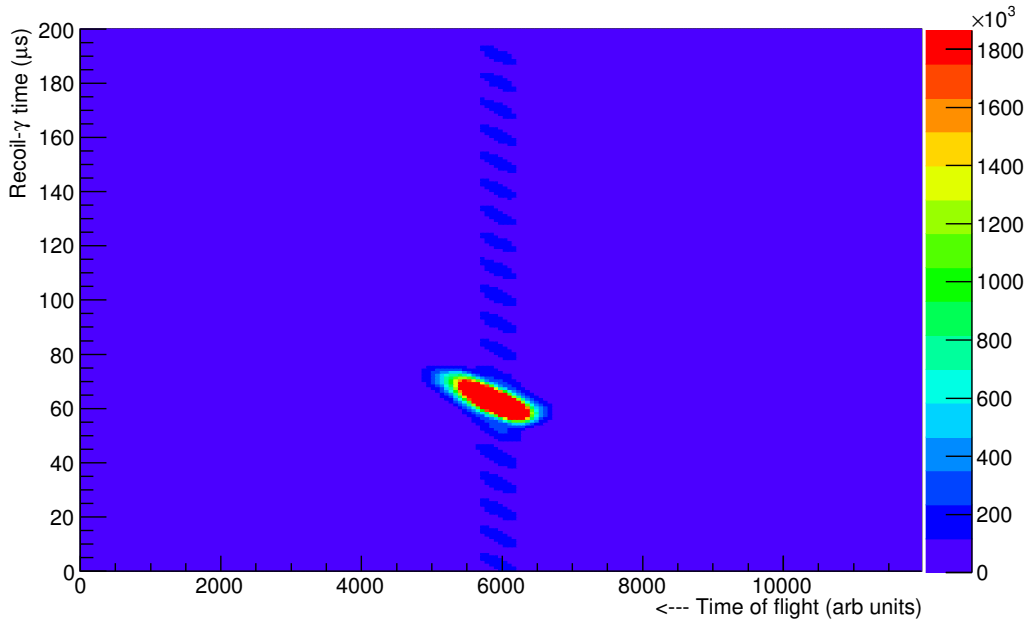

Figure 3.7: Two-dimensional plot of recoil-γ time difference versus the time of flight of ions between the MWPC and DSSD of GREAT

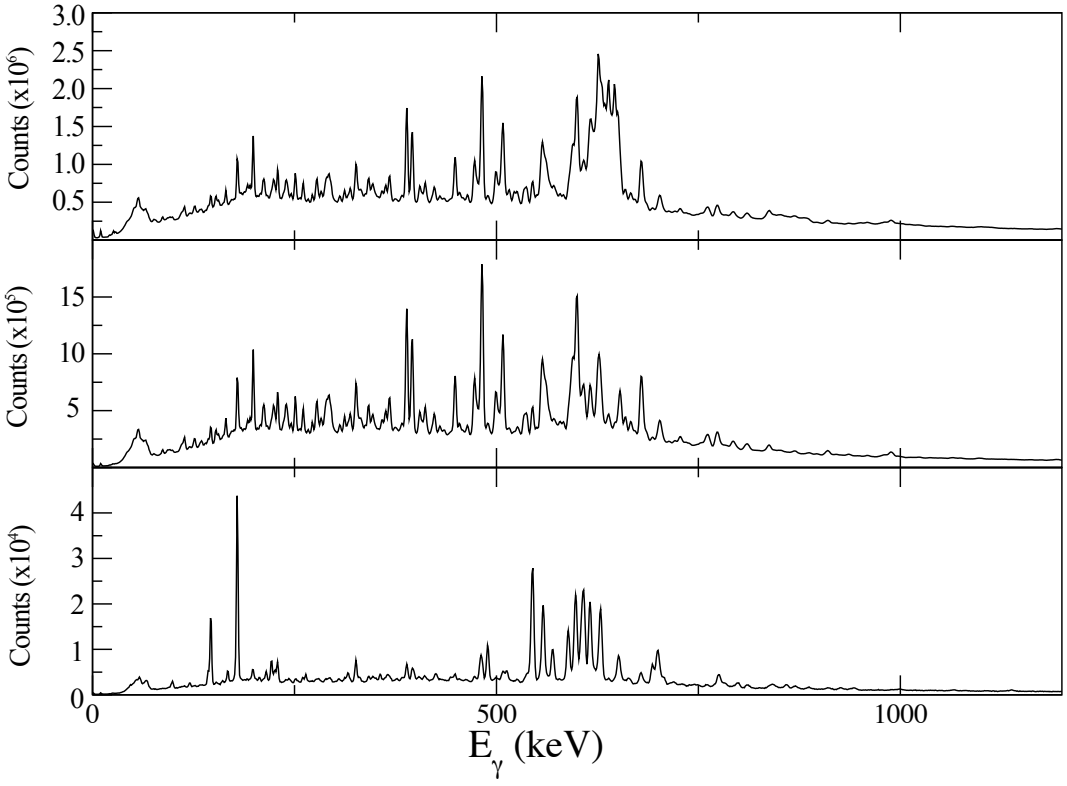

Figure 3.8: (a)Gamma-ray spectrum collected with the Jurogam spectrometer array. (b) Gamma rays detected in the Jurogam spectrometer array in delayed coincidence with the implantation of a fusion product in the DSSD. (c) Gamma rays detected in the Jurogam in delayed coincidence with the implantation of a fusion product followed by the detection of the α decay of ^{161}W in the same pixel within 3 half-lives.

timing and energy of these decays γ rays emitted by the nucleus of interest can be associated with a specific type of recoil. This is an exceedingly useful method to remove background from other open reaction channels. An example of a recoil-decay tagged spectrum is shown in figure 3.8(c).

3.7 Total Data Readout

The first recoil-decay tagging experiments used a data acquisition system with a hardware trigger. A trigger condition may have been that any focal plane detector was active. All signals from other detectors would then be delayed and read as part of this event. This leads to problems with common dead time. The trigger gate would

need to be wide (up to 50 μs) for γ-decaying isomeric states. This leads to high dead-time; up to 75% when running at high rates. The total data readout (TDR) triggerless system was designed for GREAT to overcome this dead-time problem [L$^+$01].

The TDR method overcomes this problem by reading all data, from each individual detector, time-stamping them relative to a 100 MHz clock and collecting them all in a software event builder using spatial and temporal correlations to determine events. Using software-based triggering the correlations can be processed before writing to tape. Here random γ rays can be eliminated by requiring that we see a recoil in the implantation detector then only γ rays detected in a time window determined by the time of flight are considered. Simultaneously, the spatial coordinates of the implanted nucleus are recorded and any later emission in that location within a set time window are treated as decays.

The signals from GREAT are read out by electronics and processed as in figure 3.9. The energy and timing signals are sent from the shaping amplifiers and constant fraction discriminators (CFDs) to the VXI card inputs which have 32 independent 14-bit ADC channels. Each input has a gate generated either by external CFD or software controlled triggers. A time stamp is generated for each channel at the start of its gate from within the ADC card, this is passed on to the event builder where correlations are determined. The distribution and synchronisation of the time-stamping is controlled by a 100 MHz metronome for all ADCs.

3.8 Detector Calibrations

Energy Calibrations

The output of the detector system is an electrical signal that is proportional to the energy deposited. These signals have no analytical meaning without reference to the

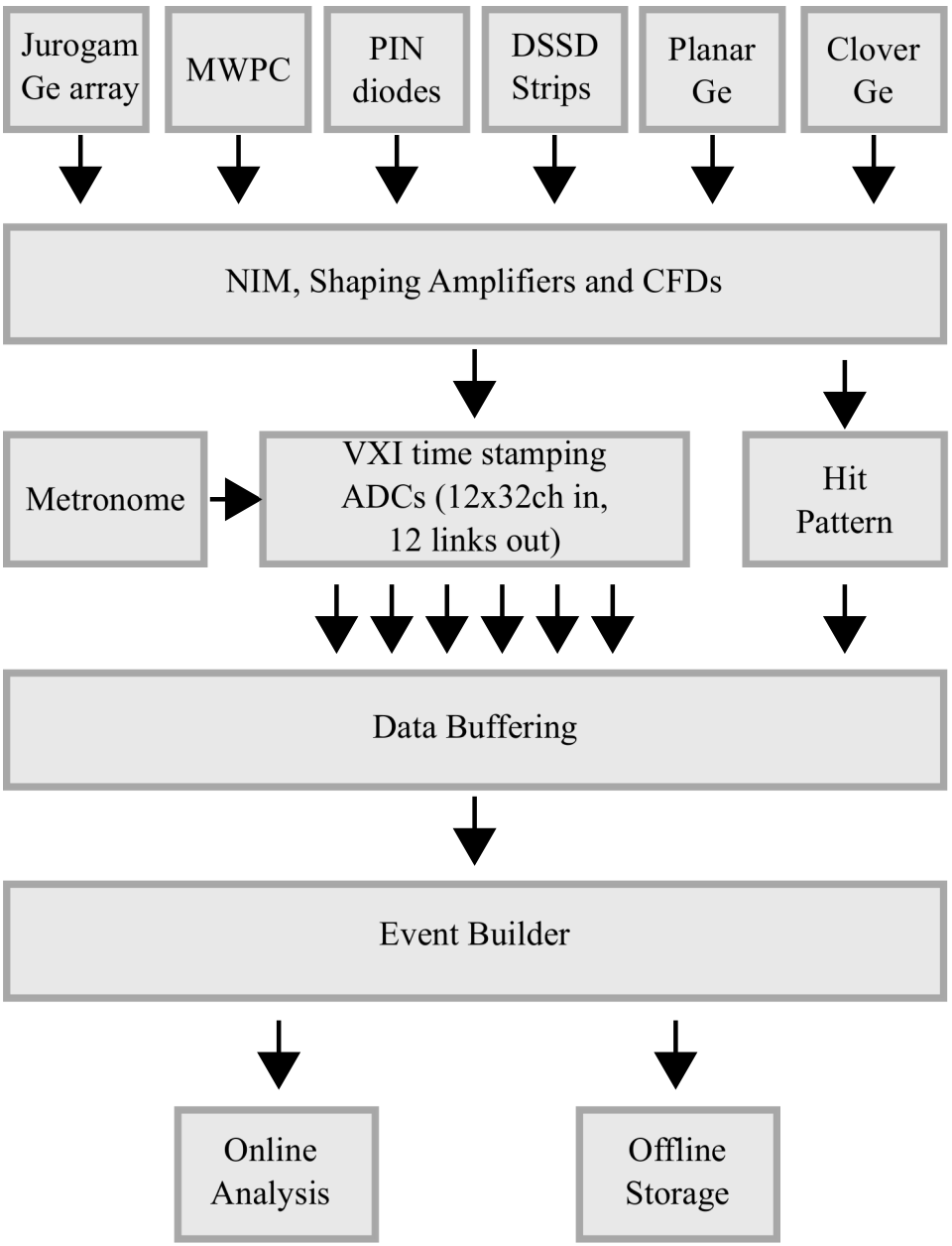

Figure 3.9: Schematic of the TDR system's electronics and data acquisition system. [L+01]

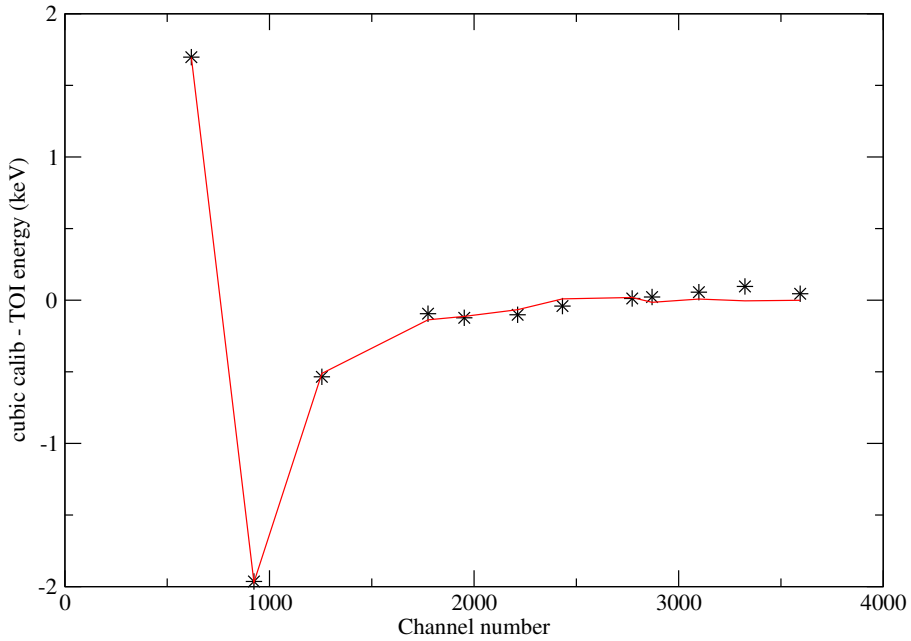

Figure 3.10: Non-linear behaviour of an ADC. The difference between calculated energy from the cubic fit to data and tabulated given values is plotted as a function of channel number using ^{152}Eu and ^{133}Ba sources. The solid red line is the fitted function.

radiation energies to which they correspond. To assign energies to these signals an accurate energy calibration must take place. This is done using standard calibration sources with known radiation energies.

The germanium detectors of the Jurogam array and the focal-plane are calibrated using a stationary, calibrated source containing ^{152}Eu and ^{133}Ba which emit γ radiation over a wide range of energies, from 80 keV to 1408 keV. The Analogue to Digital converters used are non-linear below channel number 1400. To correct for this non-linearity a damped-sine correction [Eec06] is carried out following a cubic fit for higher energy channels. A damped-sine correction involves fitting the function $Ae^{-Bx}sin(Cx+D)$ to the difference in energy between the calibrated peaks and the reference values, as shown in figure 3.10. This function is then subtracted from the cubic fit.

The DSSDs require two separate calibrations. The first is the external calibration, required for initial online analysis, which is done using a stationary, triple-α source

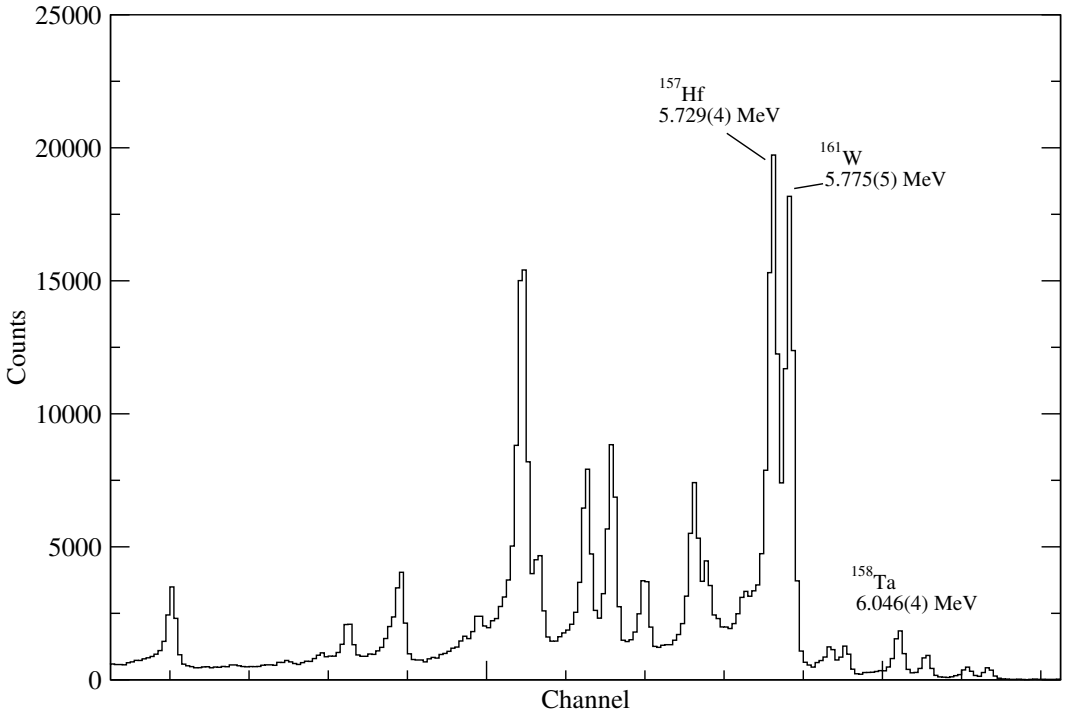

Figure 3.11: Spectrum showing α decays detected in a single DSSD strip. The decay peaks labelled [PWC$^+$96] are some of those used for internal calibration.

containing ^{239}Pu, ^{241}Am and ^{244}Cm. A secondary internal calibration is required as energy will be lost as the α particles must travel through the dead layer on the front surface of the DSSD. The internal calibration involves using known α-decay energies expected to follow the implantation of recoils produced in fusion-evaporation reactions. Figure 3.11 shows a typical spectrum for a single DSSD strip and indicates the decay peaks used for the calibration. The calibration used a linear fit from ^{162}W to ^{158}Ta and could be checked using the ^{161}W peak.

Efficiency Calibration

The efficiency of germanium detectors is energy dependent. An efficiency calibration is needed in order to determine accurately the relative intensities of γ rays. The detection efficiency of any given detector is given by the ratio of total number of events detected, the area of a peak, to the expected number of events emitted by the source

$$\epsilon_{abs} = \frac{N}{AIt}, \tag{3.6}$$

where A is the activity of the standard source, I is the branching ratio of the transition and t is the live time. The curve for the detection efficiency of Jurogam was fitted using EFFIT, part of the Radware software package [Rad95], as shown in figure 3.12. EFFIT fits the function

$$ln(\epsilon_{fit}) = \left[\left(A + Bx + Cx^2\right)^{-G} + \left(D + Ex + Fx^2\right)^{-G}\right]^{-1/G}, \tag{3.7}$$

where x is $ln(\frac{E_\gamma}{100})$ and y is $ln(\frac{E_\gamma}{1000})$, The G parameter determines the shape of the turnover region between the high and low energy efficiency curves [Rad95]. This shows the efficiency for the Jurogam γ-ray spectrometer array is $\sim 4\%$ at 1.3 MeV. Separate efficiency calibrations were carried out for both data sets used in this work, as different configurations of Jurogam were used in each experiment.

Doppler-shift Corrections

The Jurogam array is made up of six rings of Germanium detectors, each at a different angle θ relative to the beam direction. As the recoiling compound nucleus is travelling extremely fast ($\sim 3\%$ speed of light) the emitted γ radiation will be subject to Doppler shift. The measured γ-ray energy in each ring will vary from the true value by the relation

$$E_s = E_0\left(1 + \frac{v}{c}cos\theta\right), \tag{3.8}$$

where E_s is the shifted γ-ray energy, E_0 is the true transition energy, $^v/_c$ is the velocity of the recoil as a fraction of the speed of light and θ is the detector angle relative to the beam direction. Figures 3.13(a)-(c) show the shifted spectra for detector rings at the forward, normal and backward angles, compared to 3.13(d) we can see that for forward angles the energy is shifted up and for backward angles, shifted down.

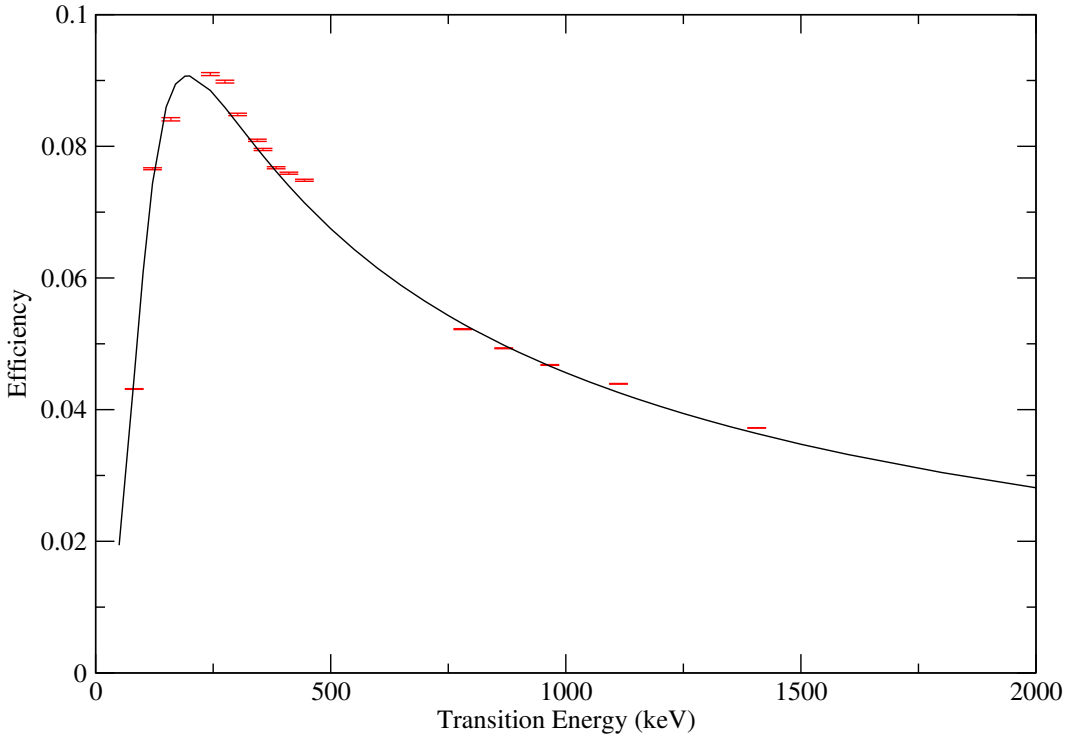

Figure 3.12: The efficiency curve for Jurogam array measured using standard radioactive sources. The curve was fitted using EFFIT giving parameters: A=1.88, B=1.75, C=0, D=1.52, E=-0.6, F=-0.09, G=4.87. The points plotted are those given by equation 3.6

The value of $^{v}/_{c}$ must be measured to correct these γ energies. This is done by plotting a graph of $^{E_s}/_{E_0}$ against cos θ yielding a gradient of $^{v}/_{c}$, which measured for ^{161}W to be 0.0314%. The Doppler-corrected spectrum given is demonstrated in figure 3.13.

3.9 Data Analysis

3.9.1 Gamma-ray Coincidence Analysis

The Jurogam array is capable of detecting two-fold, three-fold and high fold γ-ray coincidence data in large quantities. In order to investigate level schemes of nuclei produced via fusion-evaporation reactions, higher-fold data can be sorted into γ-γ

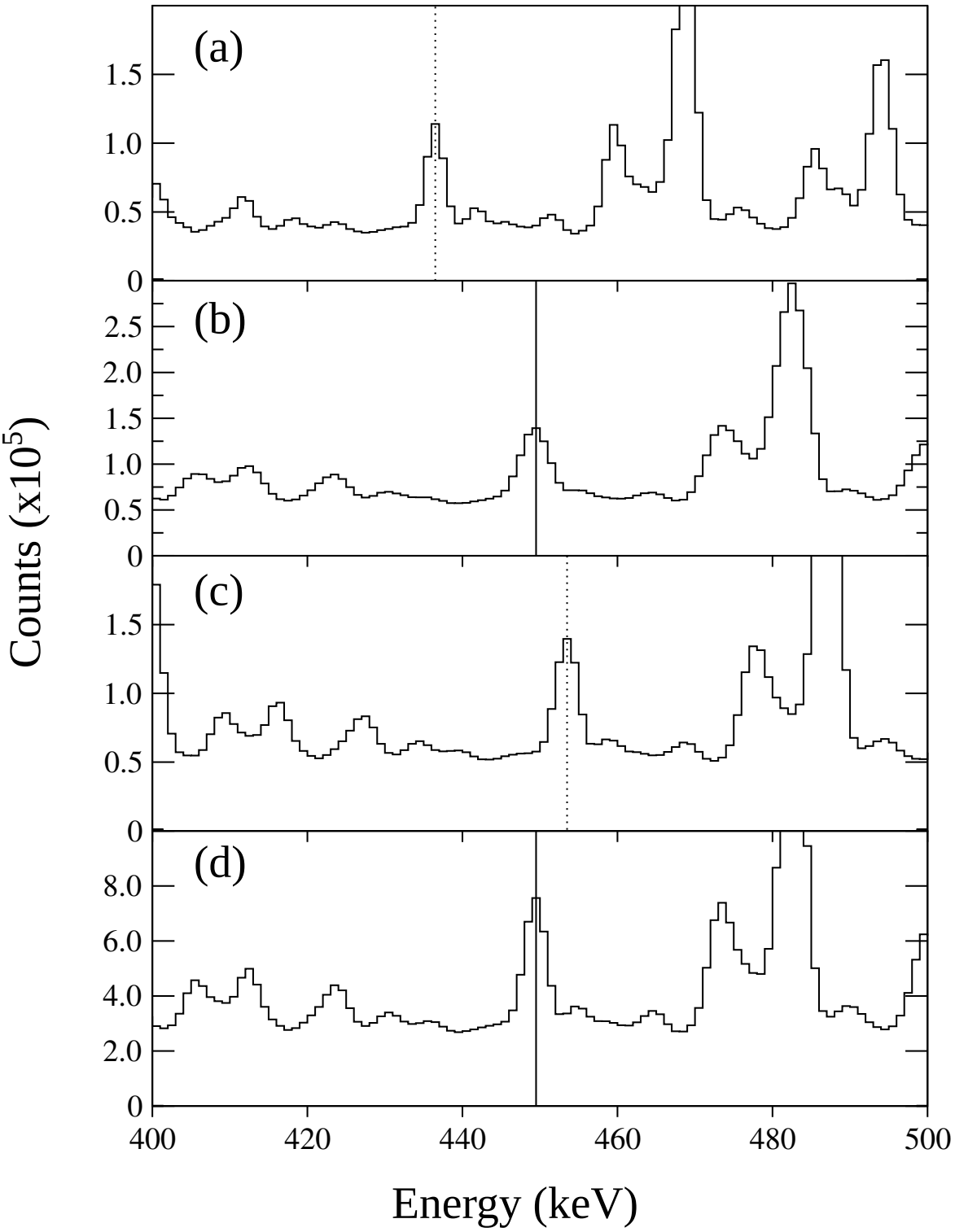

Figure 3.13: (a) Doppler-shifted recoil-correlated spectra at 72.05° (b) 90° and (c) 157.6°, (d) Summed recoil-correlated spectra following Doppler correction.

or γ-γ-γ coincidence events. These can then be analysed using Radware software packages Escl8r and Levit8r, respectively [Rad95].

Coincidences can be demanded with γ rays of specific energies on one axis of the γ-γ matrix or two axes of a cube. All coincident events will be projected onto the remaining axis in the form of a one-dimensional spectrum. Weak structures may be enhanced by the use of summed coincidences by taking a list of γ-ray energies and summing their coincident γ-ray spectra. The analysis of a number of coincidence spectra may allow for the identification of discrete decay paths of transitions through which an excited nucleus will decay.

The relative intensities of transitions can be used to order transitions within a cascade. These differences in intensity come about due to unobserved decay paths feeding levels at differing excitation energies. This results in transitions from lower-spin states occurring more frequently and increasing their relative intensity.

3.9.2 Angular-Correlation Analysis

Measuring the angular correlation of coincident γ-rays is a powerful tool for determining the spin and parity differences between excited nuclear states and bringing meaning to level schemes. Following a fusion-evaporation reaction the residual nuclei, produced with high excitation energy and spin, are aligned with their angular momenta perpendicular to the beam axis. Any anisotropy in γ-ray emission direction is therefore clearly identifiable. The preference exhibited is sensitive to I^{π} values of the initial and final states of the transition and is completely characterised by the relative population of the magnetic substates. The angular dependence of the intensity of a γ-ray transition can be expressed in the form of the angular distribution function

$$W(\theta) = 1 + A_2 P_2(cos\theta) + A_4 P_4(cos\theta), \tag{3.9}$$

where $P_k(cos\theta)$ are Legendre Polynomials and θ is the angle with respect to the direction of the beam, determined by the detector ring in Jurogam (as described in table 3.1). Here, using unpolarised γ rays, only even values of k are used, though odd values of k can be used for circularly polarised light or β-radiation [GTH65]. The angular distribution coefficient, A_k for each γ transition is determined by fitting equation (3.9) to the measured intensity of the coincident (cascade) peak in each ring. A_k^{max}, the value of A_k for a nucleus that is maximally aligned perpendicular to the beam, can be calculated according to the approach described in reference [Yam67].

For a transition between I_i and I_f with competing multipolarities L_1 and L_2 of multipole mixing ratio δ, the coefficient A_k^{max} is given in terms of statistical tensors B_k and F_k [Yam67] as follows

$$A_k^{max} = \frac{B_k(I_i)}{1+\delta}[F_k(I_f L_1 L_1 I_i) + 2\delta F_k(I_f L_1 L_2 I_i) + \delta^2 F_k(I_f L_2 L_2 I_i)]. \qquad (3.10)$$

For a mixed M1/E2 transition L_1=1 and L_2=2. For a Pure E1 or E2 $L_1 = L_2$, therefore the mixing ratio δ disappears. This simplifies the angular distribution coefficient to

$$A_k^{max} = B_k(I_i)F_k(I_f L_1 L_1 I_i), \qquad (3.11)$$

with values tabulated in ref [Yam67] and also ref [MS74] where the calculations were extended to higher spins. Examples of angular distributions for both a pure stretched dipole and quadrupole calculated by this method are shown in figure 3.14. These clearly demonstrate that angular distributions are useful when determining the multipolarity of a transition; stretched quadrupoles are most intense at angles along the beam line, stretched dipole at 90° to the beam axis.

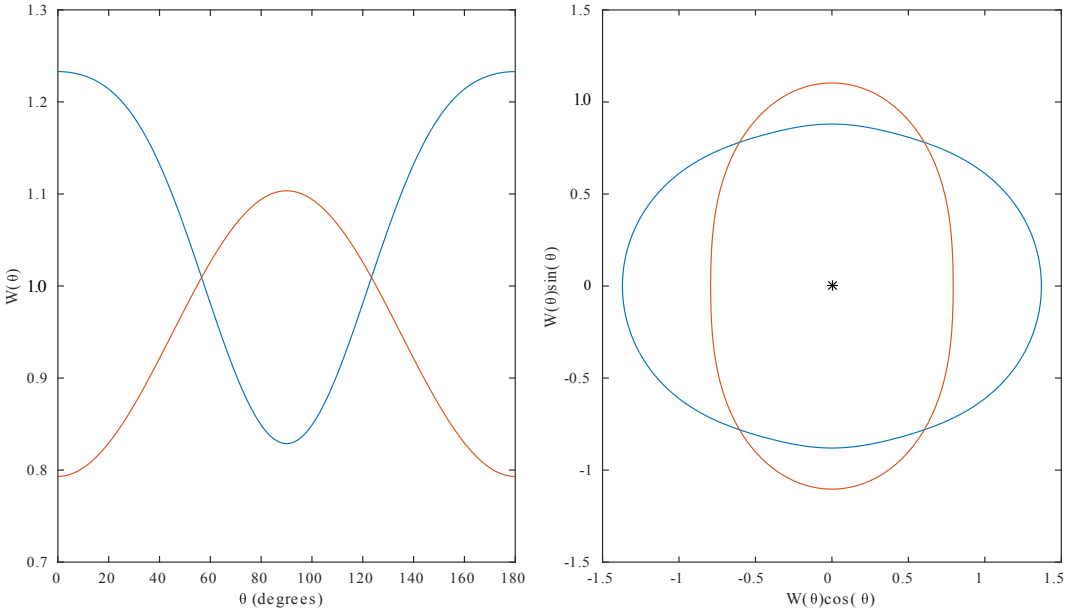

Figure 3.14: Angular distributions of typical Dipole and Quadrupole transitions. From ref. [Yam67] angular distribution coefficients were used, for a stretched E1 transition $\frac{29}{2} \rightarrow \frac{27}{2}$ $A_2^{max} = -0.27586$ $A_4^{max} = 0$ and for a stretched E2 $\frac{29}{2} \rightarrow \frac{25}{2}$ $A_2^{max} = 0.39409$ $A_4^{max} = -0.14888$. Attenuation coefficients of $\alpha_2 = 0.8$ and $\alpha_4 = 0.5$ were used.

Of course in reality many transitions are not maximally aligned, in these cases an attenuation coefficient α_k is required where

$$A_k = \alpha_k A_K^{max}, \qquad \alpha_2 \sim 0.75, \qquad \alpha_4 \sim 0.4, \tag{3.12}$$

α_k may be calculated either experimentally, estimated empirically or calculated according to a model [Yam67]. The attenuation coefficient α_k is often expressed as a function of $\frac{\sigma}{J}$, where σ represents the half-width of the m-state population's assumed Gaussian distribution. Also, in reality the detectors used for γ-ray spectroscopy have a finite opening angle. The coefficient Q_k can be used to account for the fact that point detectors are not used. This gives the angular distibution coefficient as

$$A_k = \alpha_k Q_k A_k^{max}. \tag{3.13}$$

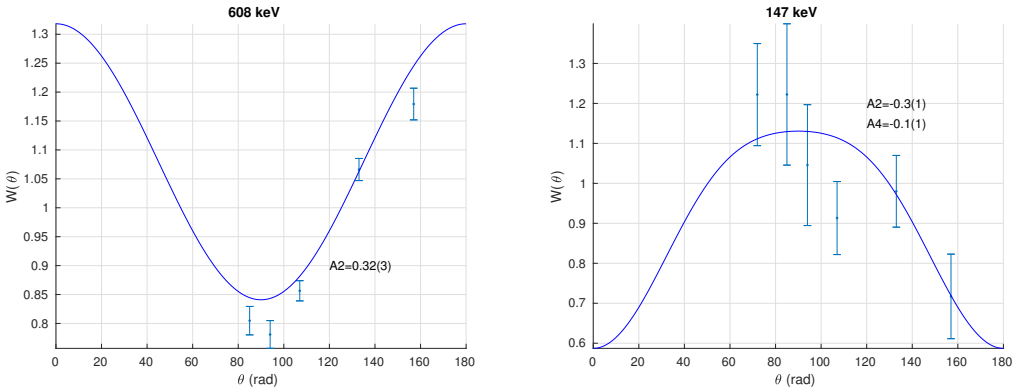

Figure 3.15: Example angular distributions of transitions seen in ^{161}W. The curves are fits of the angular distribution function W(θ) (3.9) to the experimental data. These were used to determine values of A_2 and A_4.

3.9.3 Experimental Angular Correlation Measurements and Multipolarity Assignments

Two examples of fits of equation 3.9 to experimental data for ^{161}W are shown in figure 3.15. Spectra were unfolded from the data into six 2D matrices of the full Jurogam array against individual rings at angles listed in table 3.1. For γ rays of interest in correlation with feeding transitions, peak areas were measured for each ring and normalised to give a value of $W(\theta)$. Fits were obtained using a Matlab least squares fit for equation 3.9, in this work coefficients $Q_{2,4}$ have been taken as 1.

Mixed Multipolarities - E2/M1

The clear distinction between multipolarities is complicated by mixed transitions, most commonly E2/M1 transitions. For a non-zero mixing ratio $\delta_{E2/M1}$, the value of A_k^{max} given in equation 3.10 is used. A larger positive mixing ratio will give a dipole distribution closer to that of a stretched quadrupole. A negative mixing ratio will therefore increase the preference for emission along 90°.

3.9.4 Angular Intensity Ratios

For weaker transitions or data sets with lower statistics an angular intensity ratio can be calculated in place of full angular correlations. This involves taking a ratio of the intensity of a γ ray at extreme angles and at a normal angle as follows

$$R_{DCO} = \frac{I[158°(90°)]}{I[90°(158°)]}, \tag{3.14}$$

for the extreme angles spectra are taken from ring 1(157.6°), and normal angles were the spectra of rings 4 (94.16°) and 5 (85.84°) summed. Typical values for a stretched quadrupole are much higher than those of a stretched dipole. A drawback of this method is this ratio is dependent on the multipolarity of the the feeding transition. For pure ($\delta = 0$) and stretched ($J_1 - J_2 = \lambda_1$) transitions $R_{DCO}[E2 \Leftrightarrow E2] = R_{DCO}[E1 \Leftrightarrow E1]$ so these conditions must be applied with caution.

Chapter 4

Multiparticle Excitations in ^{161}W

Excited states have been identified for the first time in the extremely neutron-deficient odd-mass nucleus ^{161}W. The nucleus was produced via the ^{58}Ni(^{106}Cd, $2pn$)^{161}W heavy-ion fusion-evaporation reaction carried out at the University of Jyväskylä, Finland. The level scheme, established for the first time in this work, extends to spins above 20^- and contains a number of structures built upon multi-particle excitations. The structure of the ^{161}W nucleus appears to differ greatly from heavier tungsten isotopes. The non-collective behaviour of the nucleus is exhibited by the pattern of γ-ray energies emitted from the nucleus as it de-excites, indicating a series of multiplets based on multiparticle excitations. The nucleus, five neutrons above the N=82 shell closure, displays no sign of collective excitations even to high spin.

4.1 Motivation

The evolution of collectivity is determined experimentally by investigating the variation of nuclear excited states and their properties over a wide range of nuclei. Short-range interactions between constituent particles of a nucleus can be strong enough to allow a small number of valence nucleons in anisotropic orbitals to polarise the nuclear core and cause the onset of deformation. A symptom of this is the possibility that neighbouring nuclei may exhibit a very different collective behaviour. The largest open shell currently experimentally accessible is the $82 < N < 126$ spanning 44 isotopes of which excited states have been established in 32 to date. The neutron-deficient tungsten isotopes in this shell allow the evolution of the properties of low-spin states to be investigated as a function of neutron number. Here it is also possible to examine the influence of orbitals originating from above and below the $N = 82$ shell gap for neutrons $(f_{7/2}, h_{9/2}, i_{13/2})$ and protons $(s_{1/2}, d_{3/2}, h_{11/2})$, respectively. The nucleus' shape is sensitive to the occupation of these orbitals as the collectivity varies smoothly yet rapidly over the transitional γ-soft isotopes above the $N = 82$ shell closure.

The attractive force between the spin-orbit partners $\pi h_{11/2}$ and $\nu h_{9/2}$ has been found to increase as the $h_{11/2}$ proton shell is occupied in extremely neutron-deficient nuclei. This is illustrated in Figure 4.1 by the departure from the usual trend where all low spin levels appear to decrease in energy with increasing neutron number. In these neutron-deficient nuclei in the region of $N > 82$ and $Z < 82$ there is a clear turning point in the energy of the 8^+ states in all shown nuclei around $N = 88$. Indeed the 8^+ state has been seen to drops below the 6^+ level in ^{156}Hf [S$^+$05] and ^{158}W [J$^+$17]. It is also clear that the energy of the 8^+ state decreases as the $\pi h_{11/2}$ orbital fills with increasing proton number.

This plot seems to suggest there is a distinct threshold in the transition to single-particle behaviour in the region of $86 \leq N \leq 90$ for in these elements. This will be

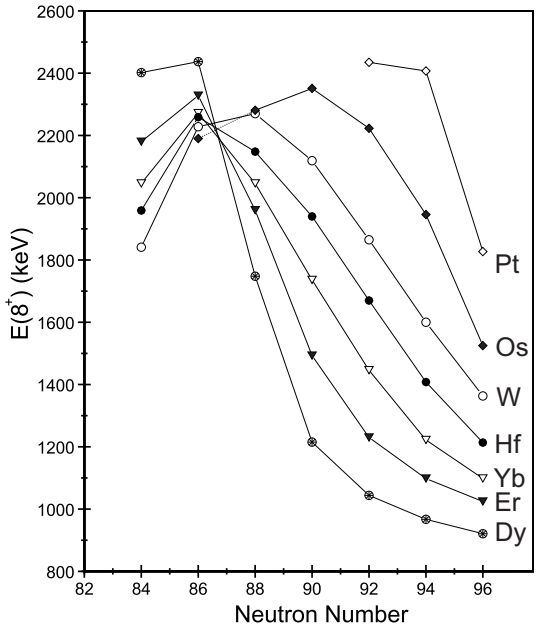

Figure 4.1: Variation in excitation energy of 8^+ states for N≤92 even-Z isotones from Dy to Os. Data extracted from the NNDC NUDAT database.

discussed in terms of the light tungsten isotopes and the excitation levels measured in ^{161}W, which confirm the single-particle nature of the nucleus.

In the vicinity of closed shells excited states are expected to be generated by aligning the angular momenta of a small number of nucleons. For example ^{158}W, just two neutrons above the $N = 82$ closed shell, has excited states up to 6^+ generated by aligning a pair of $f_{7/2}$ neutrons forming a multiplet, while the 8^+ isomeric state is formed by an $(f_{7/2}, h_{9/2})^2$ or $(h_{9/2})^2$ alignment [J$^+$17]. This is in comparison to ^{166}W [SHR$^+$92], just 8 neutrons heavier which has a structure made up of rotational bands built on $i_{13/2}$ neutron alignments.

The transition in nuclear structure in nuclei of $84 < N < 92$ further prompts a study of the interplay of collective and single-particle behaviours in the light tungsten isotopes.

4.2 Experimental Details

The experiment for the identification of excited states in ^{161}W was performed at the Accelerator laboratory of the University of Jyväskylä, Finland. Excited states in ^{161}W were produced using heavy-ion evaporation reactions involving a self-supporting ^{106}Cd target foil of nominal thickness of 0.9 mg/cm^2, with $\sim$ 96% isotopic enrichment. The nucleus ^{161}W was produced using a 270 MeV ^{58}Ni beam with average intensity of 6 pnA via the $2pn$ particle evaporation channel for $\sim$ 110 hours.

Prompt γ rays were detected at the target position by the Jurogam array. Recoiling fusion-evaporation residues were separated from fission products and scattered beam by the RITU gas-filled separator and implanted into the GREAT spectrometer at the focal plane. A more in-depth discussion of the equipment is found in section 3.3. All detector signals from Jurogam and GREAT were passed to the total data readout (TDR) acquisition system [L$^+$01] where they were time stamped with a precision of 10 ns to allow accurate temporal correlations between γ rays detected at the target position, recoils implanting in the focal plane and any subsequent decays. These data were sorted into γ-γ-γ cubes using GRAIN [Rah08] and analysed using the RADWARE levit8r software package [Rad95].

4.3 Results

4.3.1 Identification of γ-rays Emitted by ^{161}W

Prior to this study the only known nuclear properties of ^{161}W were the energy (5775 keV), half-life (409 ms) and branching ratio (73%) of its alpha decay [HFM$^+$79, PWC$^+$96]. In this work excited states in ^{161}W have been observed for the first time.

The RDT technique was employed in this work to correlate γ rays with recoils and their subsequent radioactive decays. The proximity in α-decay energy of ^{161}W to

the decay of its daughter ^{157}Hf (E_α = 5729 keV, $t_{1/2}$ = 115 ms) could lead to some ambiguity in the assignment of γ rays to ^{161}W via the RDT technique, see figure 4.2(a). For this reason further steps were undertaken to confirm that the assignment of γ rays to the level scheme of ^{161}W was irrefutable. Figure 4.2(a) shows alpha decays detected within the DSSD following the implantation of a recoiling reaction product within 1200 ms ($3\times t_{1/2}$). Here the overlap of the two α-decay peaks is clear. Figure 4.2(b) contains all γ decays detected in the Jurogam array in delayed coincidence with the alpha decay of ^{161}W within 1200 ms of a recoil implantation followed by the α decay of ^{157}Hf within 400 ms. This eliminates the the possibility of recoil-decay correlating with ^{157}Hf produced directly in the reaction. Figure 4.2(b) shows intense γ-ray transitions assigned to ^{161}W on the basis of these correlations.

Excited states have been observed up to a tentative spin of $45/2^-$ with an excitation energy of 5534 keV. Gamma-ray energies were measured using coincidence spectra generated from an $\alpha(^{161}$W)-correlated γ-γ-γ cube. The correlation time between implantation and the decay of the recoil was limited to 1500 ms and matrix contained 8×10^6 α-correlated γ-γ-γ events. The ground state, as in ^{165}Os, has been assigned a spin and parity of $7/2^-$ based on measured proton and α-decay chains originating from the ground state of ^{170}Au [K$^+$04].

Figure 4.3 shows typical γ-ray coincidence spectra. Two parallel structures are clearly distinguishable with interlinking transitions. This is made more apparent in Figure 4.4 which shows typical summed, double-gated spectra generated from a $\alpha(^{161}$W)-tagged γ-γ-γ cube by demanding coincidences between two lists of transitions. Figure 4.4(a) shows γ rays found in coincidence with both a list of transitions comprising the 558, 616 and 590 keV transitions and a list comprising the 570, 652, 708, 783 and 99 keV transitions. Here we see only the γ rays assigned to the left-hand structure of the level scheme of ^{161}W, shown in Figure 4.5. Figure 4.4 (b) contains all γ rays in coincidence with both a list of transitions 598, 545, 608 and 629 keV and the list of transitions 617, 490, 694, 481 and 679 keV. This shows all γ

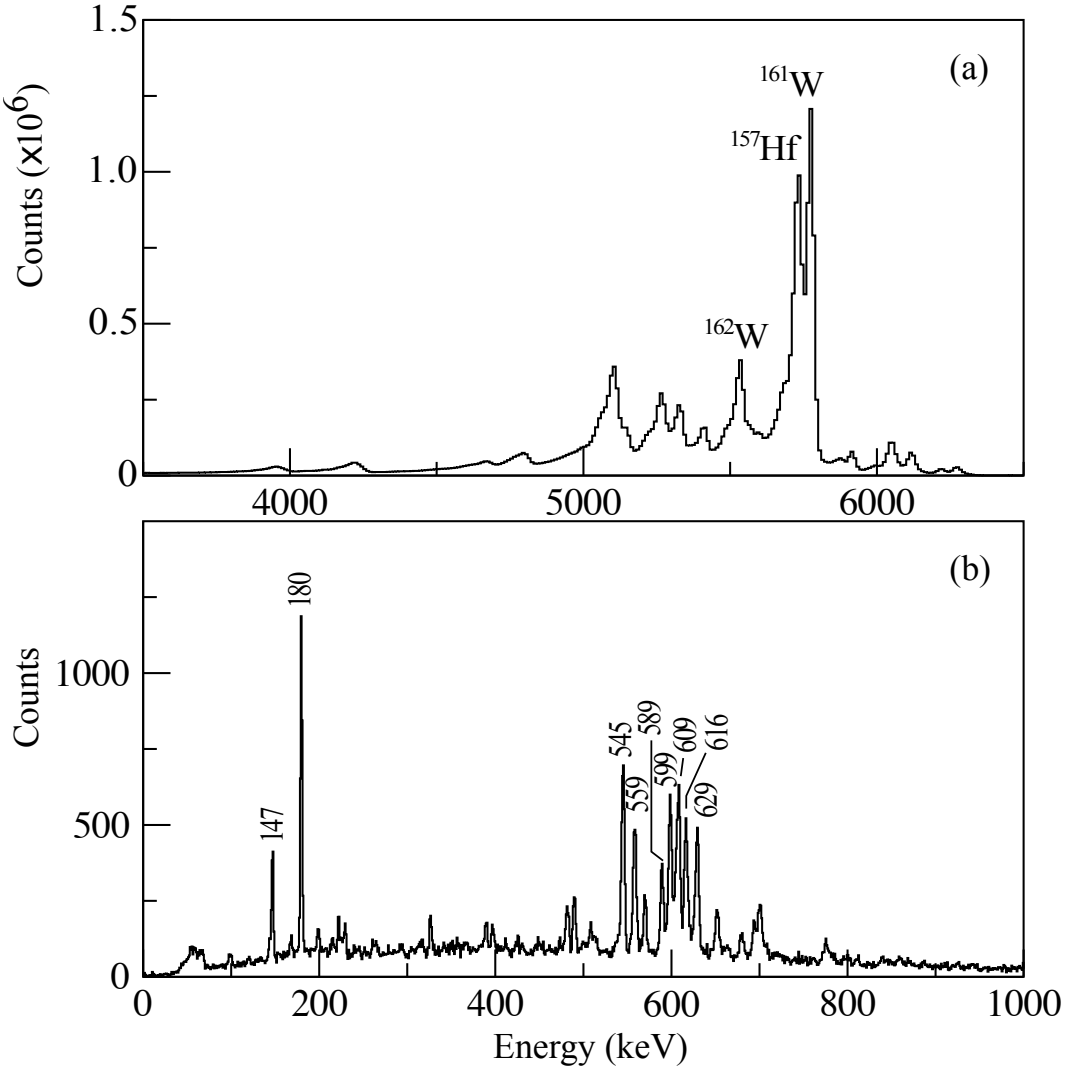

Figure 4.2: (a) All α decays detected within the DSSD following the implantation of a recoil within 1200 ms. (b) Gamma rays in coincidence with the alpha decay of ^{161}W within 1200ms of a recoil implantation followed by the alpha decay of ^{157}Hf within 400ms.

rays that make up the right-hand structure of the level scheme of ^{161}W plus those transitions feeding the structure at high spin.

Figure 4.4(c) shows coincidences demanded between lists of transitions 598, 545, 608 and 629 keV and transitions 570, 652, 708, 783 and 99 keV, indicating those transitions linking the two parallel structures.

There also appears to be a self-coincident triplet of γ rays with energy $\sim$700 keV, which form a side structure along with a transition of energy 724 keV. This is appar-

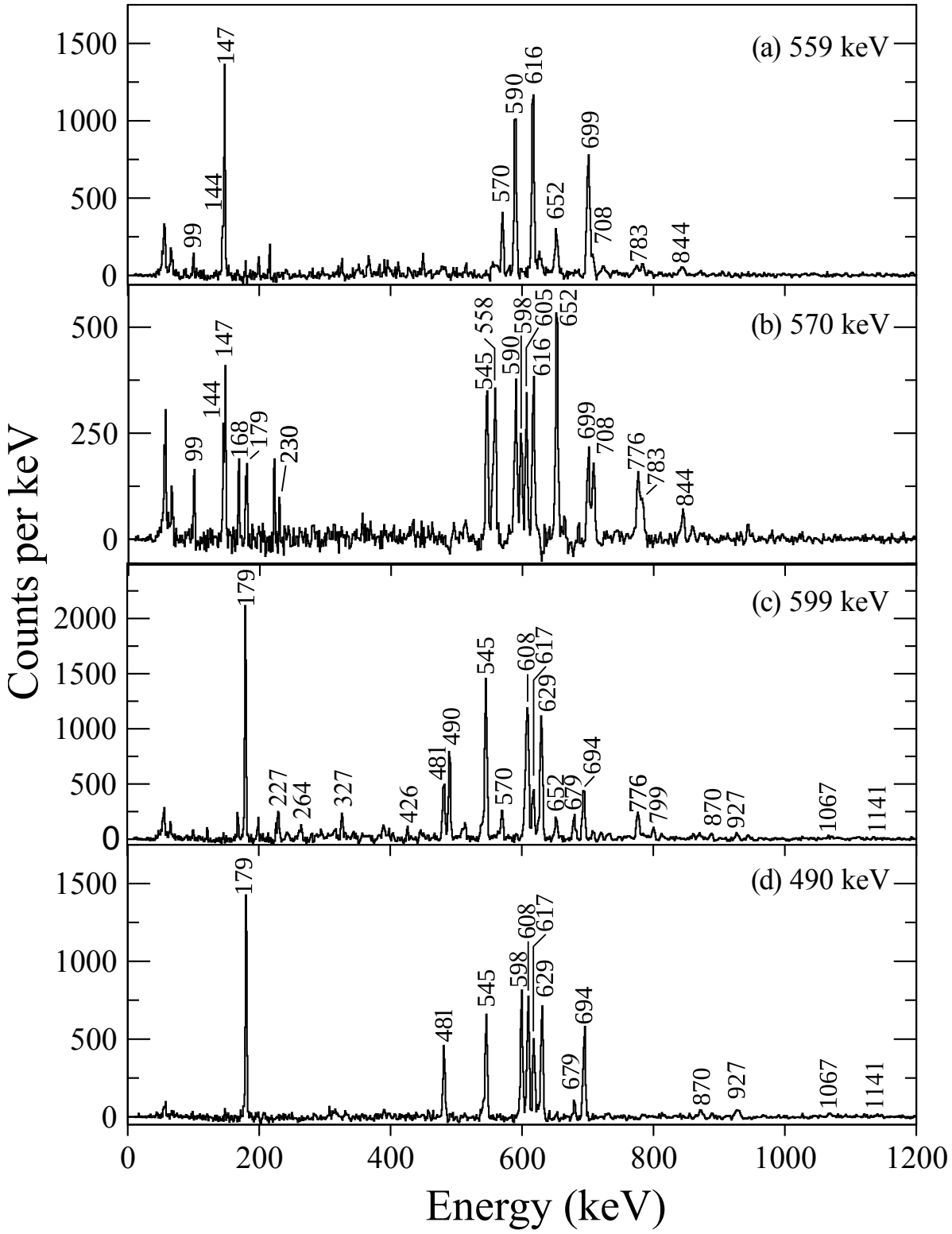

Figure 4.3: Gamma-ray coincidence spectra generated from an α-correlated γ-γ-γ cube, The correlation time between recoil implantation and $\alpha(^{161}\mathrm{W})$ decays was limited to 1500 ms. (a)γ-ray transitions from ^{161}W in coincidence with the 558 keV γ ray (b) γ rays in coincidence with the 570 keV transition (c) γ rays in coincidence with the 598 keV transition (d)γ-ray transitions in coincidence with the 490 keV transition.

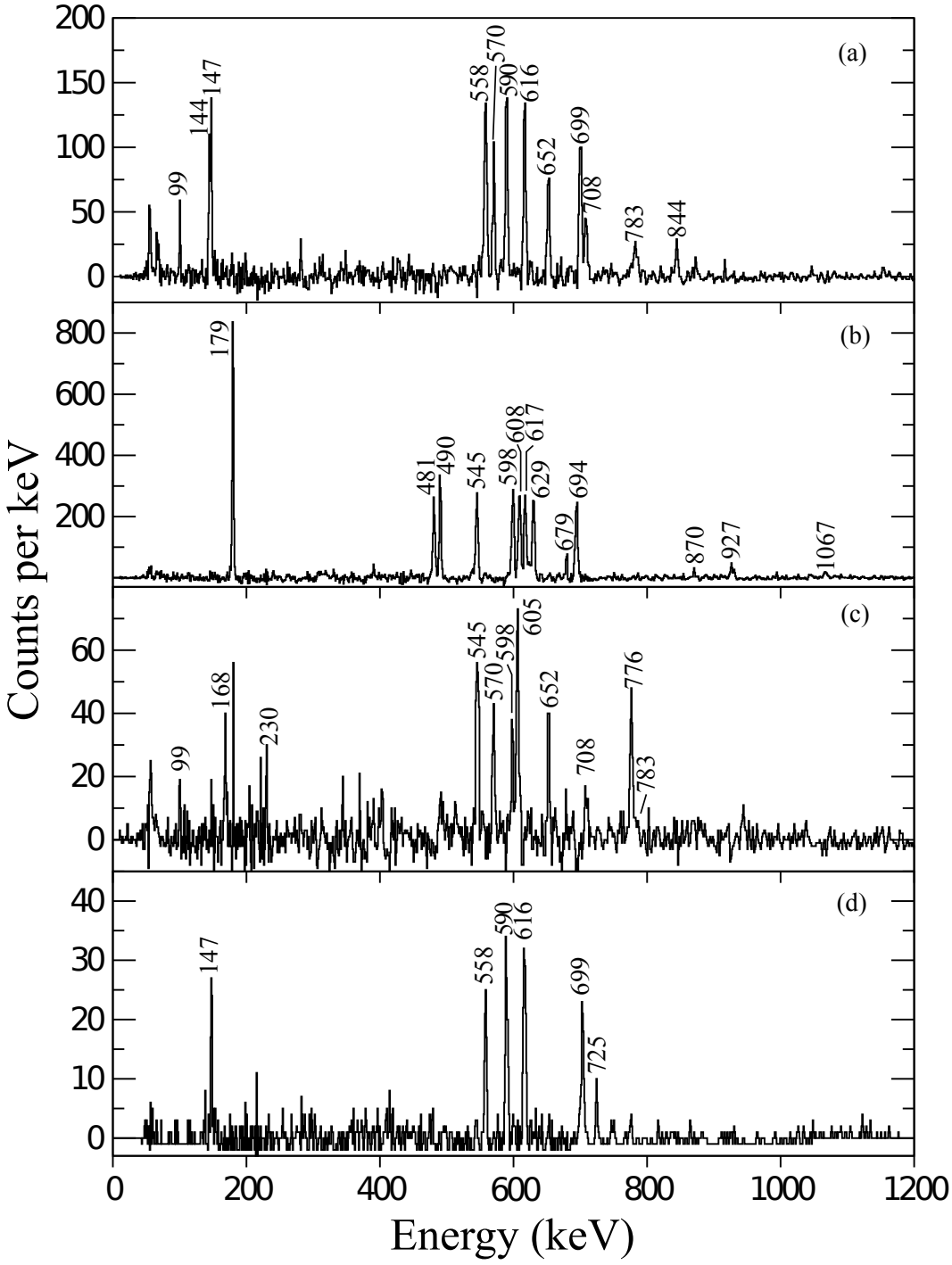

Figure 4.4: Gamma-ray coincidence spectra generated from an α-correlated γ-γ-γ cube, The correlation time between recoil implantation and $\alpha(^{161}\mathrm{W})$ decays was limited to 1500 ms. (a) γ rays found in coincidence with both a list of transitions comprising the 558, 616 and 590 keV transitions and a list comprising the 570, 652, 708, 783 and 99 keV transitions (b) Contains all γ rays in coincidence with both a list of transitions 598, 545, 608 and 629 keV and the list of transitions 617, 490, 694, 481 and 679 keV. (c) Coincidences were demanded between lists of transitions 598, 545, 608 and 629 keV and transitions 570, 652, 708, 783 and 99 keV (d) Double-gated spectrum of γ-rays in coincidence with two of the three 700 keV γ rays

ent in Figure 4.4(d) which shows a double-gated spectrum of γ-rays in coincidence with two of the three 700 keV γ-rays. Figure 4.3(c) also indicates some other weaker transitions, including a second 629 keV γ ray. These transitions all appear to be feeding in through the 629 cascade transition at spin $25/2^-$. A number of mutually coincident γ rays are seen in coincidence with the 1141 keV transition. These low-intensity transitions are 327, 264, 227, 121 and 426 keV, angular distributions could not be extracted for these transitions and ambiguities in their relative intensities mean that they have not yet been placed in the level scheme. Other transitions feeding at this level are the 799 keV, and the second 629 keV γ ray.

4.3.2 Angular Distribution Measurements

The order in which transitions were placed has been determined by measuring both the relative intensity and angular distributions of transitions. These are listed in table 5.1[1]. For example the 147 keV transition was determined to be a dipole transition from the negative A_2 coefficient measured. Figure 4.6 shows the fit of angular distribution function $W(\theta)$ to transition intensity as a function of angle for the 147 keV γ ray. This evaluation was also influenced by the presence of similar low lying $9/2^-$ states in neighbouring nuclei, ^{157}Yb, ^{159}Hf, ^{163}W [X$^+$13, DCS$^+$00, S$^+$10] and others, which feed the $7/2^-$ ground state via an M1 transition. The deduced level scheme is shown in figure 4.5.

4.4 Discussion

The low-lying states in tungsten isotopes close to the $N = 82$ shell closure are based on single quasiparticle configurations created by the alignments of individual valence nucleons. The neutrons close to the Fermi surface of a nucleus in this region of the Segré chart occupy the $f_{7/2}$, $h_{9/2}$ and $i_{13/2}$ orbitals. The proximity of ^{161}W to the

[1]Fits to angular distribution measurements shown in appendix

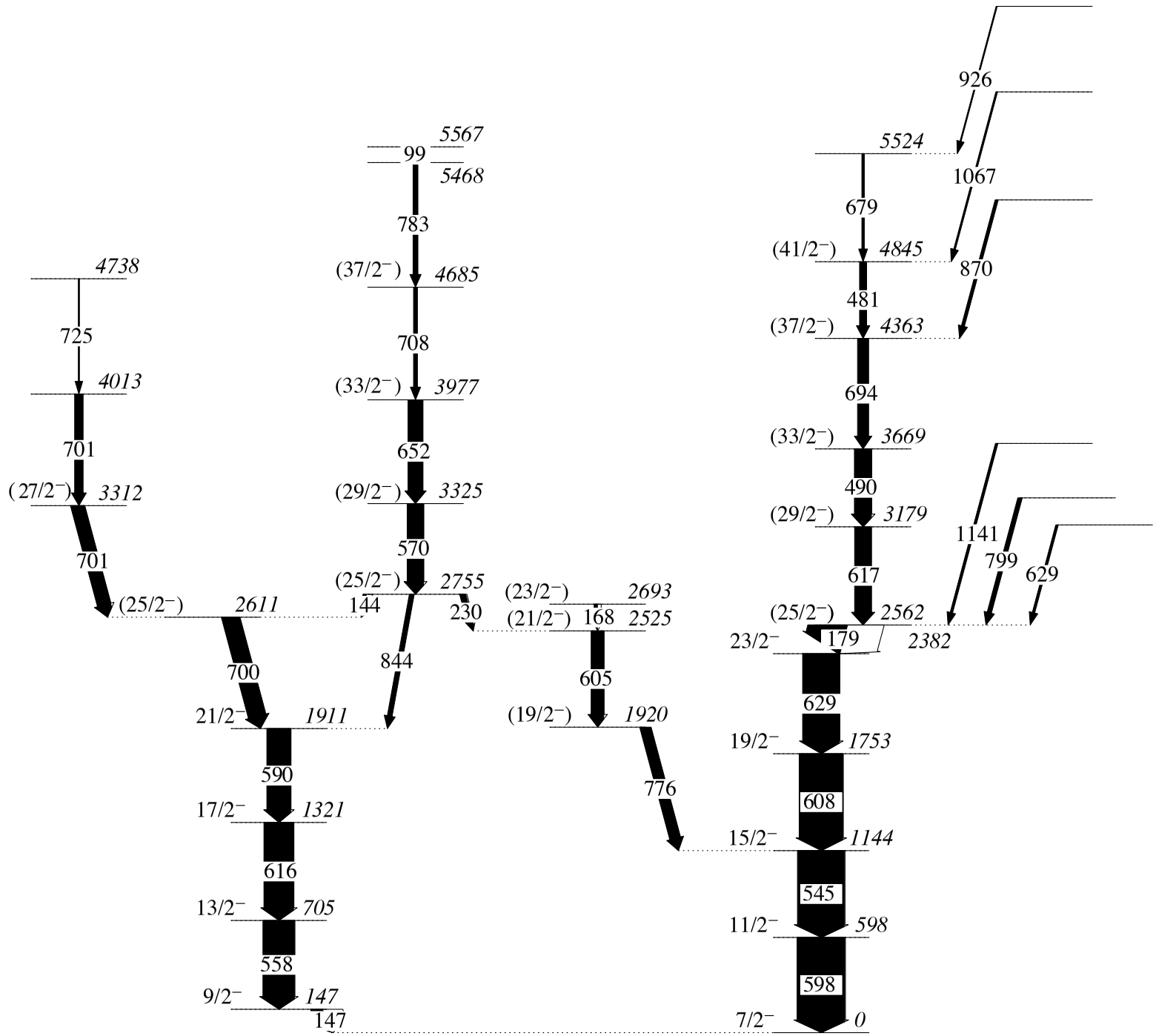

Figure 4.5: Deduced Level Scheme for ^{161}W

E_γ (keV)	I_γ	A_2	A_4	Multipolarity
99.4	4.78(5)			(E2)
121.1†	6(1)			
143.5	6.63(5)	-0.6(2)		(E1)
146.8	24.85(9)	-0.3(2)	0.1(1)	M1
167.5	6.47(4)			(E2)
179.3	80.5(2)	-0.18(6)	0.1(1)	(M1)
226.7†	11(1)			
229.6	14.19(7)	-0.6(2)		(E1)
263.8†	3.6(5)			
326.7†	9.7(9)			
425.6†	4.2(6)			
481.1	14.4(5)	0.28(6)		E2
489.6	35.6(7)	0.33(7)		E2
544.8	97.9(2)	0.21(2)	0.10(3)	E2
558.2	66.8(2)	0.19(2)	0.07(3)	E2
569.8	34.3(1)	0.18(4)		E2
589.5	51.5(2)	0.14(4)	0.05(7)	E2
598.4	100(1)	0.15(4)	-0.08(6)	E2
605.4	44.6(9)			
608.4	91(1)	0.32(3)		E2
615.9	62.7(9)	0.22(6)		E2
617.15	35.1(7)	0.2(1)		E2
629.5	} 77(1)			
628.7		0.23(5)		E2
652.1	34.1(1)	0.14(6)		E2
679.4	5.1(3)			E2
694.1	23.4(7)	0.41(8)		E2
699.5	} 49.6(8)			
700*				
701*				
708.1	8.3(3)	0.6(2)		E2
724.7	2.3(2)			E2
776.0	23.3(7)			
783.1	5.2(3)	0.22(6)	0.01(9)	E2
799.3	9(1)			
844.2	7.6(3)			(E1)
870.4	6.26(5)			
927.0	2.4(3)			
1067.1	3.36(5)			
1141.0	5(1)			

Table 4.1: Measured γ-ray transition properties for ^{161}W. * is unresolved doublets, †transitions not placed in level scheme. Fits to angular correlation measurements shown in appendix, for all but the strongest transitions the A_4 coefficient has been set to zero. Energies are accurate to ± 0.5 keV for strong transitions ($I_\gamma > 10\%$) rising to ± 2.0 keV for weaker transitions.

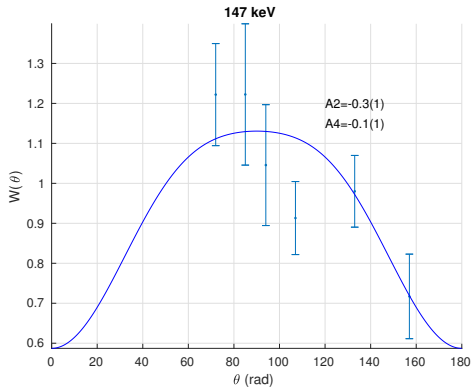

Figure 4.6: Angular distribution measured for 147 keV transition on ^{161}W, for further explanation see Section 3.9.2

$N = 82$ shell closure makes it an ideal probe for investigations into the interplay of single-particle interactions and collective structures in weakly deformed nuclei. The quasiparticle configurations of maximally aligned states in ^{161}W are discussed below.

4.4.1 Single-Particle Configurations

The values of spin assigned to these states following angular distribution measurements allows for an initial attempt to assign these states to the single-particle configurations on which these multiplets are built. From Figure 4.8 it is clear that the relevant orbitals at this mass are the proton $h_{11/2}$ and neutron $f_{7/2}, h_{9/2}$ and $i_{13/2}$ orbitals.

The ground state and first excited state have been taken as the single-quasiparticle $\nu f_{7/2}$ and $\nu h_{9/2}$ states respectively. An M1 transition from $9/2^-$ first excited state to the $7/2^-$ ground state has been identified in a number of neutron-deficient nuclei in this region, including the lighter N=87 isotones ^{157}Yb and ^{159}Hf [DCS$^+$00, X$^+$13] and also in ^{163}W fed by the M2 transition from the $13/2^+$ isomeric state [S$^+$10]. The excitation energy of this first excited state seen in neighbouring isotones has been plotted as a function of Z in Figure 4.7 along with the known $i_{13/2}$ states relative

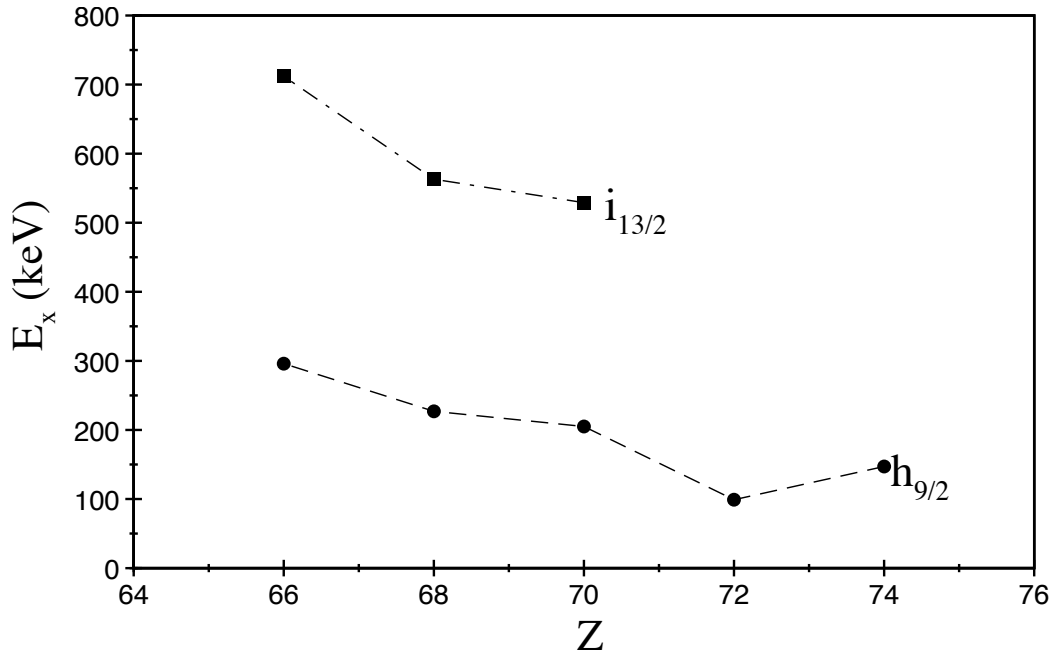

Figure 4.7: Excitation energies of the $h_{9/2}$ and $i_{13/2}$ states in N=87 isotones.

to the $f_{7/2}$ ground state. There is a general trend of decreasing excitation energy of the $h_{9/2}$ with increasing proton number. This reinforces the interpretation that there is an increasing attractive force between the $h_{9/2}$ neutron and the $h_{11/2}$ proton as the proton $h_{11/2}$ subshell fills. There is less data for the $i_{13/2}$ states, however, it appears to exhibit similar behaviour.

There is no evidence of an $i_{13/2}$ single-quasiparticle configuration in ^{161}W. The absence of this structure is consistent with the trend of increasing excitation energy of the $i_{13/2}$ state above the yrast line approaching the $N = 82$ shell closure [D$^+$13, O$^+$09, B$^+$99, T$^+$10, D$^+$92]. This indicates a nucleus with a low deformation. It is clear that the relative position of these orbitals about the Fermi surface is highly dependent on deformation, as predicted in the Nilsson diagram shown in Figure 4.8.

4.4.2 Three-Particle Configurations

The states feeding these single-particle states form multiplets based on the $h_{9/2}$ and $f_{7/2}$ neutrons. Further angular momentum is generated by the alignment of pairs of

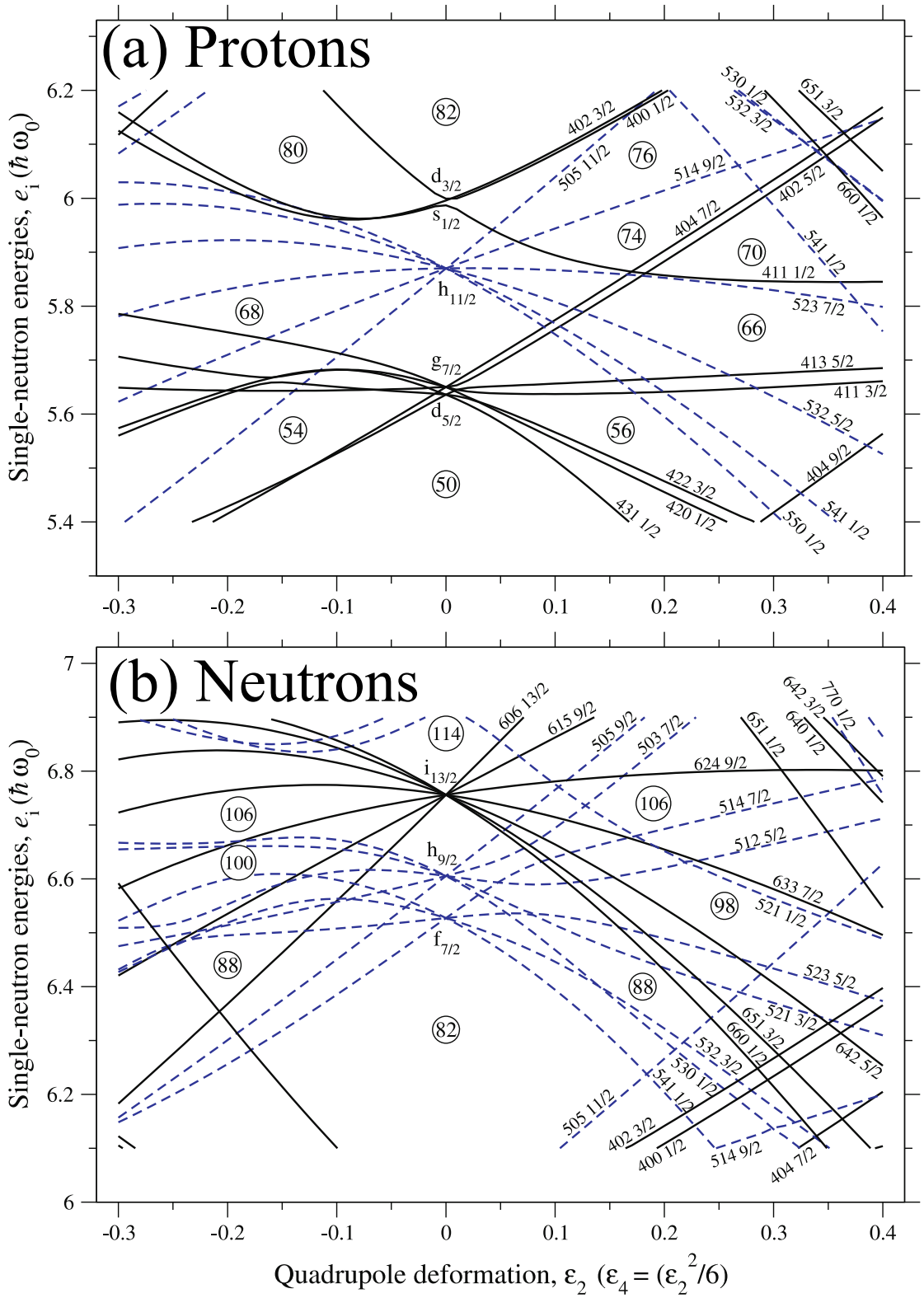

Figure 4.8: Single-particle energies calculated for A∼150 as a function of quadrupole deformation. Solid black lines represent positive-parity levels and negative-parity levels as dashed blue lines. Calculations for protons are shown in (a) and neutrons in (b). Levels are labelled according to their quantum numbers $N n_3 \Lambda \Omega$ as defined in section 1.3.1. [P+09]

neutrons in nearby orbitals. The 1911 keV $21/2^-$ level built upon the $h_{9/2}$ neutron can then be interpreted as the alignment of a pair of $f_{7/2}$ neutrons forming the $[h_{9/2}f_{7/2}^2]_{21/2}$ multiplet.

Figure 4.9 shows the low-spin yrast states of tungsten isotopes above N=82. The positive-parity even-spin states of even-A isotopes are shown next to the multiplet of states built on the $9/2^-$ states of their odd-A neighbours. It is interesting to see the clear trend of decreasing excitation energies with increasing neutron number - a well known symptom of increasing deformation, appears smooth between both odd- and even-A isotopes. From this it can be interpreted that the aligning $f_{7/2}$ neutron pair coupled to the $h_{9/2}$ single-particle configuration in the odd-N case, is equivalent to coupling the $f_{7/2}$ neutron multiplet yielding the 2^+, 4^+ and 6^+ states in the even-N core. The excitation energies of states measured in ^{159}W do not reflect the trend seen in its neighbouring isotopes. Further measurements should be carried out to confirm the ordering of states assigned to this nucleus.

The 2382 keV $23/2^-$ level above the $\nu f_{7/2}$ state has been determined to be a pair of $h_{9/2}$ neutrons aligning to form the three-quasineutron $[\nu f_{7/2}h_{9/2}^2]_{23/2}$ configuration. Figure 4.10 shows the excitation energies of the 8^+ and $23/2^-$ states of the neighbouring even- and odd-N tungsten isotopes respectively. Here the $23/2^-$ states of the odd-mass isotopes track closely the excitation energies of the 8^+ states and the systematics of the 8^+ states in nearby neutron-deficient elements, shown in Figure 4.1. The decrease in energy of the 8^+ states with $N < 88$ was interpreted as a symptom of the increasing attraction between the $\pi h_{11/2}$ and $\nu h_{9/2}$ orbitals as the $N = 82$ shell closure is approached [JLA+04].

4.4.3 Five and Higher Quasiparticle Configurations

The 2562 keV $25/2^-$, 2611 keV $25/2^-$, 2755 keV $25/2^-$ and 3312 keV $27/2^-$ states are based on five and seven quasiparticle configurations as little as 179 keV above

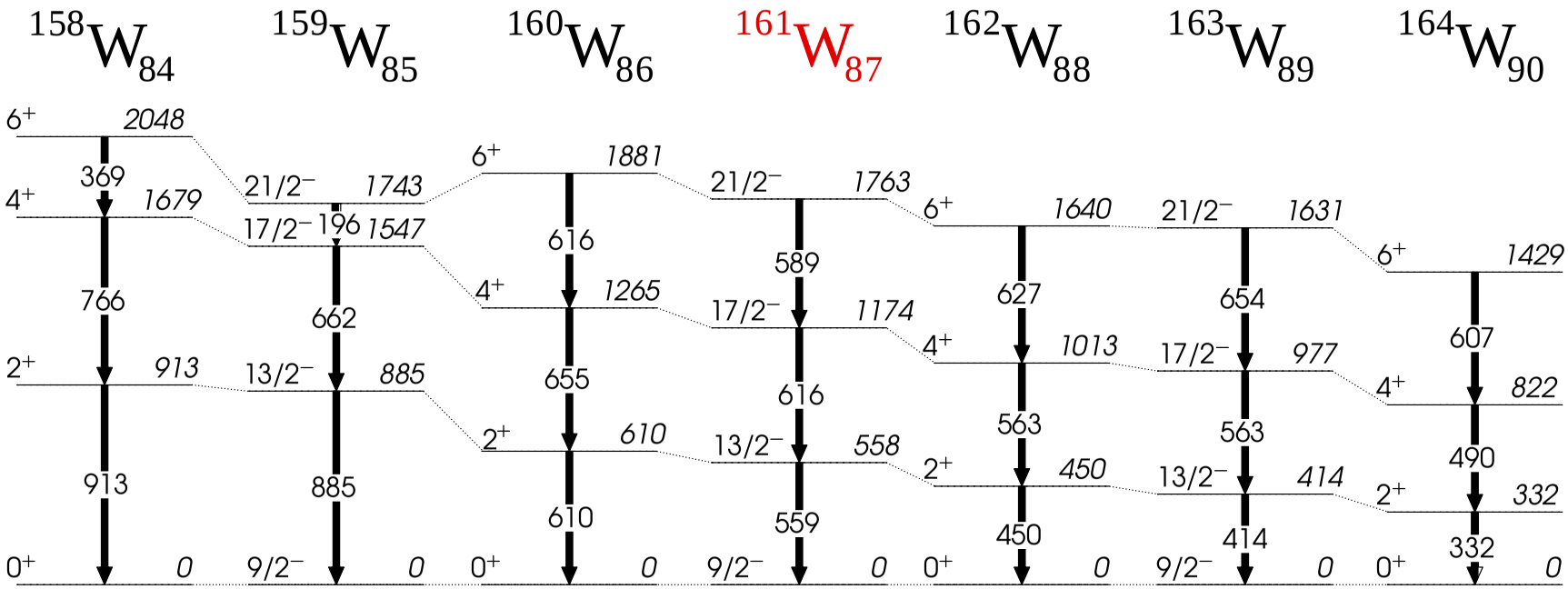

Figure 4.9: Comparison of energy levels in light tungsten isotopes, dashed lines connect states of similar structure. Excitation energy is defined relative to the $9/2^-$ bandhead for odd mass isotopes. [J+17, S+11, K+01, L+15, T+10]

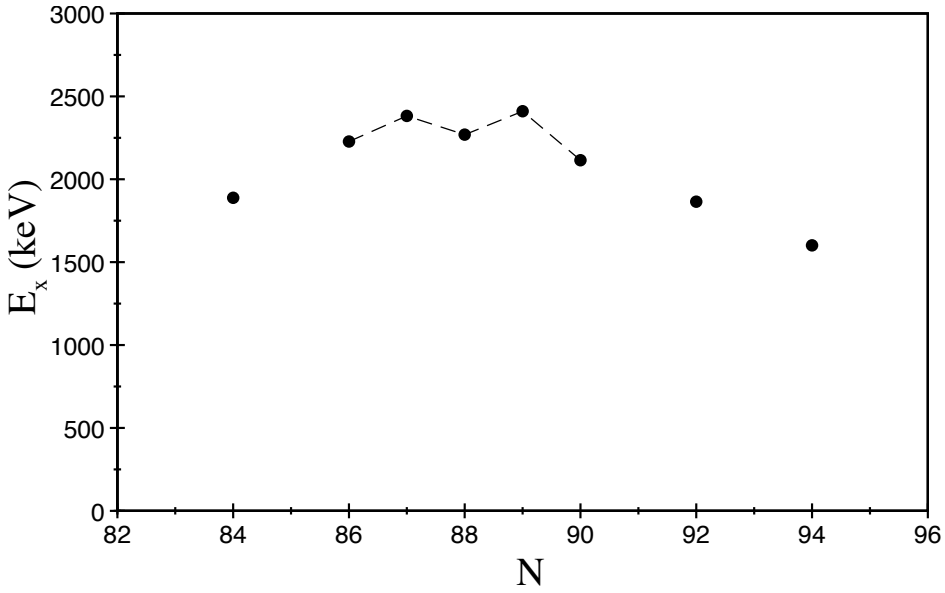

Figure 4.10: Excitation energies of the 8^+ and $23/2^-$ states as a function of N for tungsten isotopes $^{158-164}$W [J^+17, K^+01, L^+15, T^+10]

the maximally aligned three quasiparticle states. Three of these states can be interpreted as the antiparallel coupling of pair of $h_{9/2}$ neutrons to their spin-orbit $\nu h_{11/2}$ partners via the strongly attractive $(\pi h \nu n)_{1+}$ two-body interaction. This has been observed to significantly lower the excitation energies of states outside of a closed gadolinium core [Z^+96]. In ^{161}W the $25/2^-$ state at excitation energy 2755 keV feeds the $\nu h_{9/2} f_{7/2}^2$ state via two different decay paths. This state may be populated by the increase in excitation energy causing two pairs of $f_{7/2}$ neutrons to couple to the $h_{9/2}$ orbital. This state also feeds into the right-hand structure via a more complicated decay path. Angular distribution measurements for these linking transitions were inconclusive, therefore the assigned spins are tentative. All quasiparticle configurations deduced for ^{161}W are shown in Table 4.2.

The lighter even-A ^{160}W nucleus exhibits 4^+ to 2^+ excitation energy ratio of 2.07, which would typically be exhibited by a vibrational nucleus. However, the level scheme has been interpreted in terms of the alignment of a few valence nucleons outside of a closed shell [K^+01]. A reduced excitation energy is seen in this nucleus of the 8^+ state , which can be interpreted as an increasing interaction between the

$E_x(keV)$	I_i	Configuration	Quasiparticles
0	$^{7}/_{2}^{-}$	$\nu f_{7/2}$	1
147	$^{9}/_{2}^{-}$	$\nu h_{9/2}$	1
1910	$^{21}/_{2}^{-}$	$\nu h_{9/2}\nu f_{7/2}^{2}$	3
2382	$^{23}/_{2}^{-}$	$\nu f_{7/2}\nu h_{9/2}^{2}$	3
2562	$^{25}/_{2}^{-}$	$(\nu f_{7/2}\nu h_{9/2}^{2} \otimes \pi h_{11/2}^{2})_{1^+}$	5
2611	$^{25}/_{2}^{-}$	$\nu h_{9/2}\nu f_{7/2}^{2} \otimes (\pi h_{11/2}^{2})_{1^+}$	5
2755	$^{25}/_{2}^{-}$	$\nu f_{7/2}^{4}\nu h_{9/2}$	5
3312	$^{27}/_{2}^{-}$	$\nu f_{7/2}^{4}\nu h_{9/2} \otimes (\pi h_{11/2}^{2})_{1^+}$	7

Table 4.2: Maximally aligned quasiparticle configurations determined for ^{161}W

4.4.4 Emergence of Collectivity

With only a few nucleons outside of a spherical core the level energies of ^{161}W are complex. Figure 4.11 shows plots of angular momentum of the emitting state $I_i(\hbar)$ against transition energy in neighbouring even-N tungsten isotopes ^{160}W and ^{162}W [K^{+}01, D^{+}92]. In section 5.1 these plots are discussed for the heavier isotopes in terms of their alignment and rotational frequency, variables proportional to the spin and energy of the transitions. Here we will discuss them in terms of variables taken directly from experiment. This removes the need to specify K, a number which is ill-defined in γ-soft triaxial nuclei.

The two parallel structures of ^{161}W shown in Figure 4.11(b) both display a much more irregular pattern in their spin as a function of transition energy when compared to the heavier even-A nucleus ^{162}W, which displays a more collective pattern of increasing transition energy with spin. This would indicate a structure based upon non-collective multi-particle excitations whereas the heavier neighbours consist of collective bands built upon these aligned quasiparticles. In this way ^{161}W is more similar in behaviour to the lighter even-even isotope ^{160}W. A comparison of the low-spin states of the two nuclei shows that with the exception of a offset for the ground-state spin of ^{161}W, the alignment pattern is remarkably similar. The level structure of ^{161}W is based on single quasiparticle configurations when the odd neutron occupies

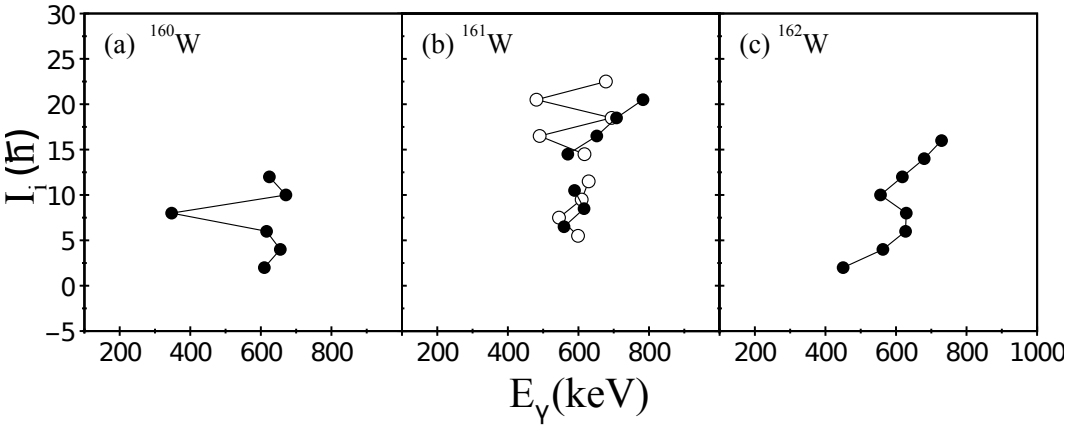

Figure 4.11: Initial spin I_i as a function of transition energy in neutron-deficient $^{160-162}$W, for odd-A ^{161}W filled circles represent states feeding the $9/2^-$ state (left hand structure) and open circles represent those feeding the $7/2^-$ ground state (right hand structure).

the $f_{7/2}$ and $h_{9/2}$ states near the Fermi surface while coupled to a near-spherical ^{160}W core.

strongly overlapping $\nu h_{9/2}$ and $\pi h_{11/2}$ spin-orbit partner orbitals. Federman and Pittel discuss such residual interactions [FP79] and the onset of deformation when the pairing interaction is overpowered by the isoscalar interaction between neutrons and protons where shell effects become insignificant relative to collective excitations.

The similar structure between the lighter ^{160}W nucleus and the odd-mass ^{161}W, which both behave as spherical systems near to a closed shell suggests a single neutron uncoupled from the core. The nuclear structure of low- to high-spin states in ^{161}W is governed by their individual single-particle degrees of freedom. The nucleus ^{161}W exists at a threshold for the onset of collectivity as a function of N in the light tungsten isotopes and indicates that the nuclear shape is strongly influenced by proton-neutron pairing interactions of spin-orbit partners at low deformation. This is indicated by the abundance of non-collective excitations which are observed to high spin.

Chapter 5

Collective Excitations in $^{162}\mathbf{W}_{88}$

Excited states in the neutron-deficient ^{162}W have been produced via the reaction ^{106}Cd(^{60}Ni,2p2n)^{162}W where the subsequent γ rays were detected using the Jurogam spectrometer array at the University of Jyväskylä. The level scheme has been extended beyond previous studies with the identification of a second band feeding the ground-state band. The underlying structure of the nucleus is discussed in terms of experimental aligned angular momentum within the framework of the cranked shell model. These experimental data suggest that the $h_{9/2}$ neutron states are increasingly favoured over the $i_{13/2}$ at low deformation. This change of structure is presented in the broader context of the nuclear structure in the $A \sim 160$ mass region.

5.1 Motivation and Previous Work

The very neutron-deficient tungsten isotope $^{162}W_{88}$ lies in the transitional region above the $N = 82$ shell closure. In this region nuclear behaviour evolves quickly from a spherical nucleus where single-particle motion is most prevalent, through γ-soft triaxial nuclei to deformed rotors near the neutron midshell. In the extremely neutron-deficient nuclei it is challenging to measure reduced transition probabilities and quadrupole moments due to low production cross sections and high γ-ray backgrounds from stronger reaction channels. However, the collectivity of a nucleus is correlated with the characteristics reflected in the yrast spectrum. A good experimental indicator of collectivity is to measure the ratio of the energy of the 4^+ state to the 2^+ state, the $E(4^+)/E(2^+)$, which increases with deformation. Figure 5.1 shows the $E(4^+)/E(2^+)$ ratio for even mass Hf, W, Os and Pt isotopes. The Hf and W isotopes show a similar smooth increase in $E(4^+)/E(2^+)$ as a function of neutron number, which indicates an increase in collectivity as the neutron number increases above $N = 82$. The Pt isotopes on the other hand (and Os to a lesser extent) show a pronounced variation from this smooth behaviour. This has been described as perturbations to the yrast sequence due to mixing of coexisting bands [DFS$^+$91, DDFB82].

It is thought to be the increasing neutron-proton attraction above $N > 88$ that accounts for the the onset of deformation [J$^+$11]. For nuclei with $N < 90$ the $f_{7/2}$ orbital is closest to the Fermi surface. This orbital has only a small overlap with the $h_{11/2}$ proton orbital, therefore the interaction is only small and the short-range pairing force causes sphericity to be favoured. With increasing number of valence neutrons the neutron orbital $h_{9/2}$ occupation probability is increased along with this attractive n-p interaction. As discussed by Federman and Pittel [FP77] the n-p interaction is often considered the strongest component of the nuclear force, and neutrons and protons filling the same shell-model orbitals or the attraction of spin-orbit partners can have strong effects on the deformation of a nucleus.

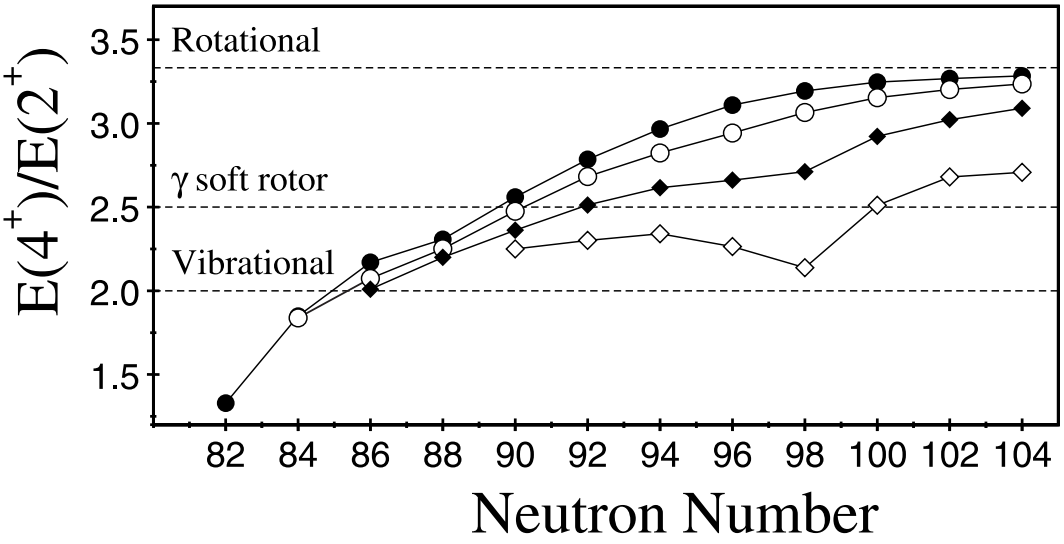

Figure 5.1: $E(4^+)/E(2^+)$ ratios for even-Z Hf (filled circles), W (open cirlces), Os (filled diamonds), Pt (open diamonds) as a function of neutron number. The dashed lines indicate the limits for rotational, vibrational and γ-soft nuclei.

Another important feature of the $E(4^+)/E(2^+)$ ratio between the spherical and rotational limits is region around the ratio of $E(4^+)/E(2^+) =\sim 2.5$ which corresponds to the γ-soft nuclei. Here the triaxial deformation of the nucleus is particularly sensitive to the occupation of specific orbitals and the relative positions of the proton and neutron Fermi surfaces at the top and bottom of their shells, respectively.

Figure 5.2 shows the Nilsson diagrams for protons and neutrons in the $A \approx 160$ region. At the predicted deformation parameters for ^{162}W ($\varepsilon_2 = 0.125$) [MNMW95] the proton Fermi surface lies in a region of low level density near the high-Ω $h_{11/2}$ states. The neutron Fermi surface lies close to the high-j, lowest-Ω $\nu i_{13/2}$ orbital and negative parity orbitals originating from both the $\nu f_{7/2}$ and $\nu h_{9/2}$ subshells. The $i_{13/2}$ neutron orbital dominates the yrast spectra of $N \geq 90$ W isotopes and the lowest energy configurations for multi-quasiparticle excitations involve either one (odd-A) or two (even-A) $i_{13/2}$ neutrons [SRA$^+$91, SHR$^+$92, T$^+$92]. Figure 5.2 shows that with decreasing deformation (towards the N=82 closed shell) the excitation energy of the $i_{13/2}$ neutron states increase relative to the Fermi surface allowing configurations involving the negative parity $f_{7/2}$ and $h_{9/2}$ orbitals to become favoured at low spin. This has been shown to be true in recent γ-ray spectroscopic

studies of $N < 90$ nuclei [D$^+$13, T$^+$10, DCS$^+$00, L$^+$11, DM$^+$15].

Of particular interest here is the observed differences between ^{162}W $N = 88$ and ^{164}W $N = 90$. The yrast band of ^{164}W [SRA$^+$91] was observed as having an alignment gain of $\Delta I_x = 11\hbar$ consistent with the rotational alignment of a pair of $i_{13/2}$ neutrons. Soon after, Dracoulis [D$^+$92] made the first measurements of the lighter ^{162}W, a lower alignment gain was measured at the first backbend, which was attributed to an $\nu(f_{7/2}/h_{9/2})^2$ configuration. Dracoulis *et al.* discussed comparisons of the aligned angular momentum for the tungsten and hafnium isotopes of N=86 to N=91. The difference in alignment between the two even-mass isotopes is clear showing the shift in structure with deformation, as predicted by the deformed shell model.

In this work the level scheme for ^{162}W has been confirmed with spin up to (17^-) using the RDT technique. This assists in the assignment of quasiparticles to their orbital configurations.

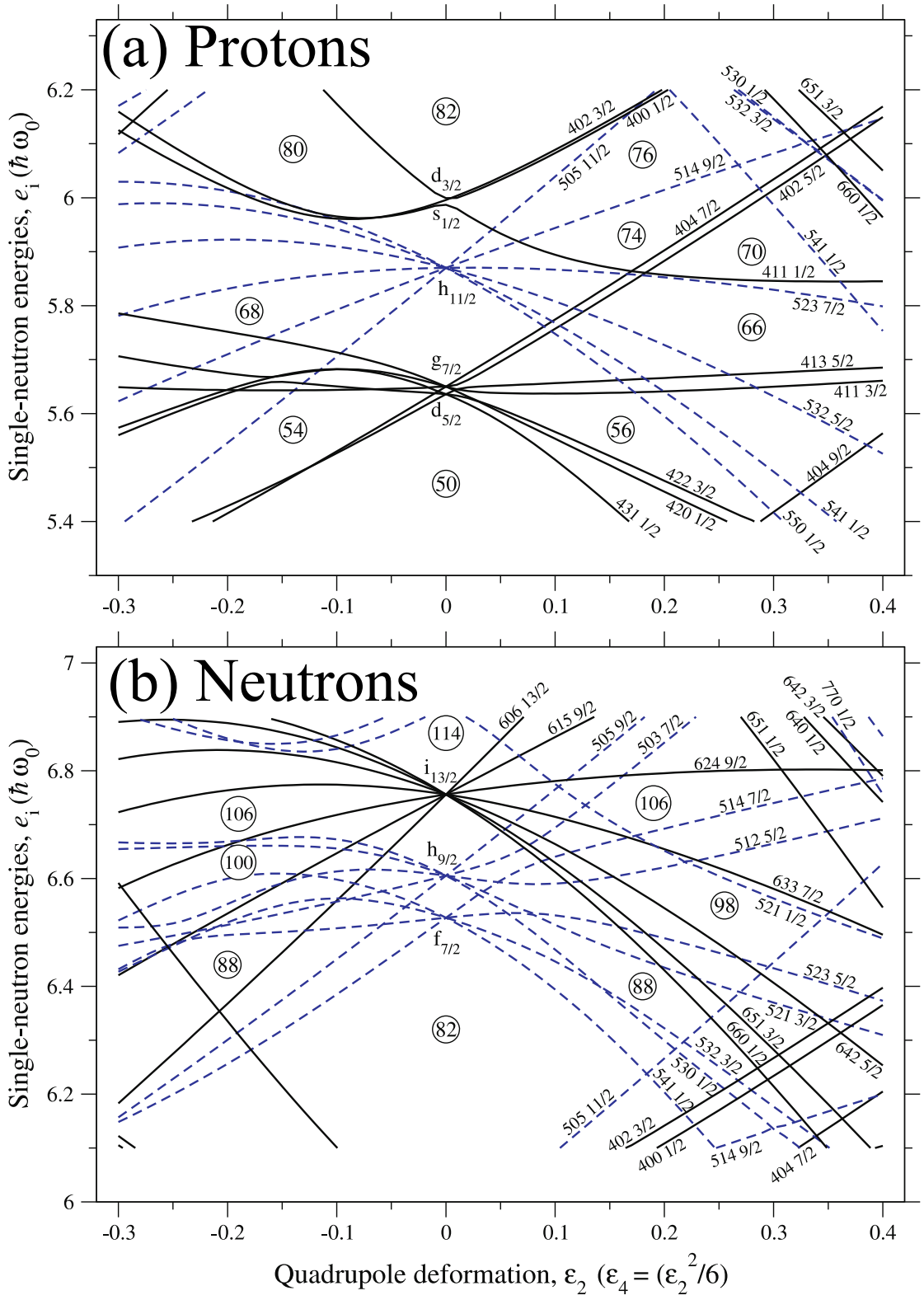

Figure 5.2: Reproduced from Figure 4.8

5.2 Experimental Details

The experiment to search for excited states in ^{162}W was performed at the Accelerator Laboratory of the University of Jyväskylä, Finland. Excited states in ^{162}W were produced using heavy-ion fusion evaporation reactions involving a self-supporting ^{106}Cd target foil with thickness of 1.0mg/cm^2, with $\sim$ 96% isotopic enrichment. The nucleus ^{162}W was produced via the $2p2n$ channel using a 270 MeV beam of ^{60}Ni with average current of 4pnA for $\sim$ 120 hours.

Gamma rays were detected at the target position by the Jurogam spectrometer array. Recoiling fusion-evaporation residues were separated from fission products and scattered beam by the RITU gas-filled separator and implanted into the GREAT spectrometer at the focal plane. A more in depth description of the equipment is given in section 3.3. All detector signals from Jurogam and GREAT were passed to the total data readout (TDR) acquisition system where they were time stamped with a precision of 10 ns to allow accurate temporal correlations between γ rays detected at the target position, recoils implanting in the focal plane and any subsequent decays. These data were then sorted into γ-γ matrices using GRAIN [Rah08] and analysed using the RADWARE ESCL8R software package [Rad95].

5.3 Results

5.3.1 Identification

The yrast states in ^{162}W were first observed by Dracoulis *et al.* using the HERA and CAESAR spectrometers [D$^+$92]. It has been possible to confirm observed γ rays identified for ^{162}W [L$^+$15, S$^+$09] using the RDT technique. The RDT technique allows spatial and temporal correlations between γ rays detected at the target position with subsequent characteristic α decays detected at the DSSD located at the focal

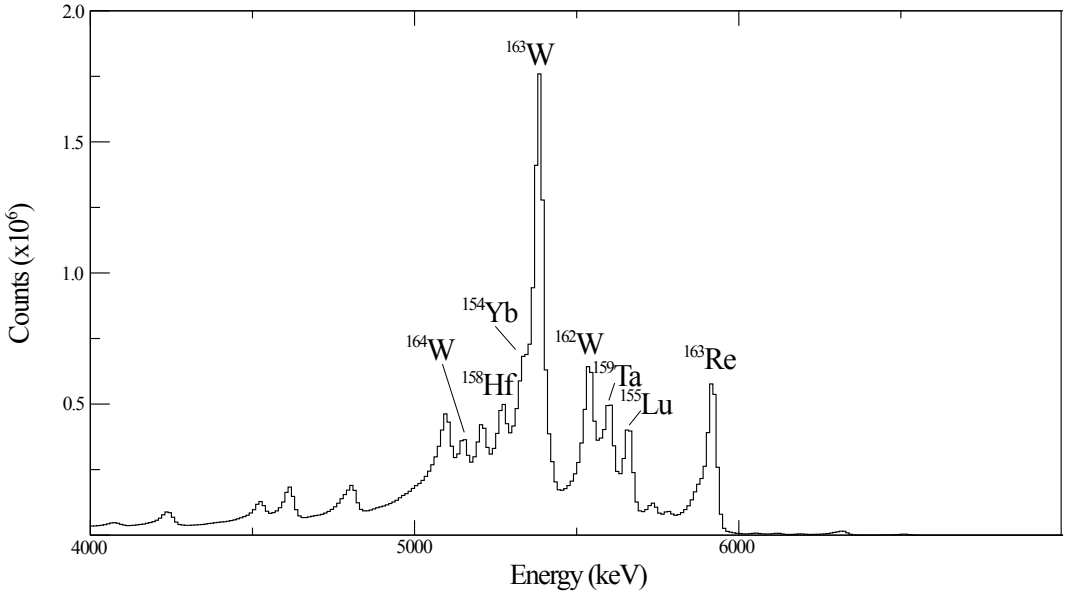

Figure 5.3: Energy spectrum of all α decays within 1200ms of the implantation of a recoil in the same DSSD pixel.

plane. For the RDT technique to provide a clean γ-ray spectrum it is necessary that the half-life of the radioactive decay is shorter than the recoil implantation rate. If two recoils impinge on the same pixel in a time comparable to the half-life random correlations can occur. The α decay properties of ^{162}W [PWC^{+}96] [E$_{\alpha}$=5541 keV, t$_{1/2}$=1200 ms, b$_{\alpha}$=44%] suggest that an unambiguous recoil-decay correlation can be achieved for the employed average recoil rate of 1.4kHz or $\sim$ 1 implantation per pixel per second.

Figure 5.3 shows α decays detected following the implantation of a recoil within the same pixel of the DSSD. The energy of the α decay of ^{162}W appears to overlap with those of other recoils produced via other reaction channels. Further conditions were therefore required in order to achieve unambiguous recoil-decay correlations. This involved demanding that each ^{162}W α decay is followed by the subsequent α decay of daughter ^{158}Hf and granddaughter ^{154}Yb in the same pixel of the DSSD. The relevant decay chain is shown in figure 5.4. The resulting γ-ray spectrum is shown in figure 5.5. The correlation time between each implantation and its successive decay was limited to 3600, 9000 and 1300 ms, respectively, around 3 times the

half-life of each decay. The transitions between low-spin states of ^{162}W are clearly observed and confirm those published in earlier work [L^{+}15].

5.3.2 Recoil-Decay Tagged γ-γ Coincidences

Figure 5.6 shows typical coincidence spectra used to deduce the level scheme of ^{162}W. These spectra were produced using recoil-decay correlations between the implanted recoil and the α-decay of ^{162}W, with the condition that only those decays following an implanted recoil within 500-4800 ms were used for tagging. This timing condition was used to limit the number of mis-correlations due to short-lived contaminants. The matrix used contained 6×10^{5} $\alpha(^{162}\mathrm{W})$-correlated γ-γ coincidence events. Figure 5.6(a) shows γ rays in coincidence with the 450 keV $2^{+} \rightarrow 0^{+}$ transition. The yrast band dominates the spectrum but there is also evidence of other structures feeding the yrast states. Figure 5.6(b) shows γ rays in coincidence with the 618 keV $12^{+} \rightarrow 10^{+}$ transition. These show the decay path of band 1 from (16^{+}) down to the ground state.

A second collective band has been identified in this work and is observed in Figure 5.6(c) by selecting γ rays in coincidence with the 535 keV transition, which appears to decay into Band 1 via the 296 keV transition.

These same timing and correlation conditions were applied when matrices for the measurement of DCO ratios. This involves measuring the ratio between intensities of γ rays measured extreme and normal angles. Due to insufficient statistics, DCO intensity ratios could only be measured for two transitions, the $4^{+} \rightarrow 2^{+}$ and $2^{+} \rightarrow 0^{+}$. This means that the multipolarity of the 296 keV linking transition could not determined. Table 5.1 contains the intensities of all assigned γ rays and those DCO ratios that could be measured.

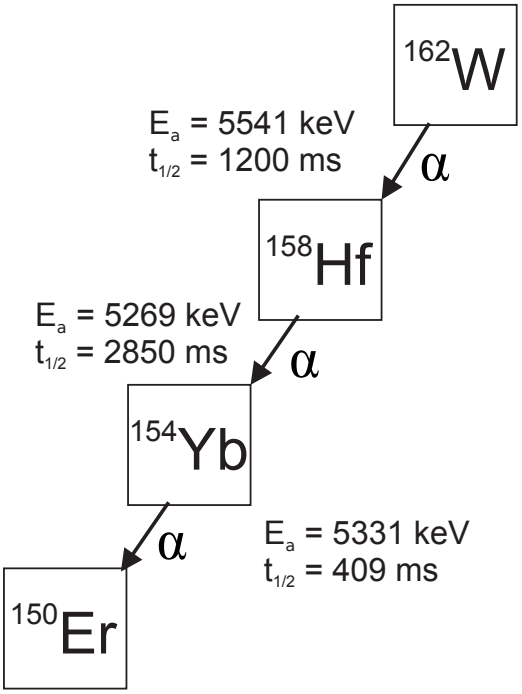

Figure 5.4: Alpha decay chain following the decay of ^{162}W. The radioactive decay data has been taken from [PWC^{+}96].

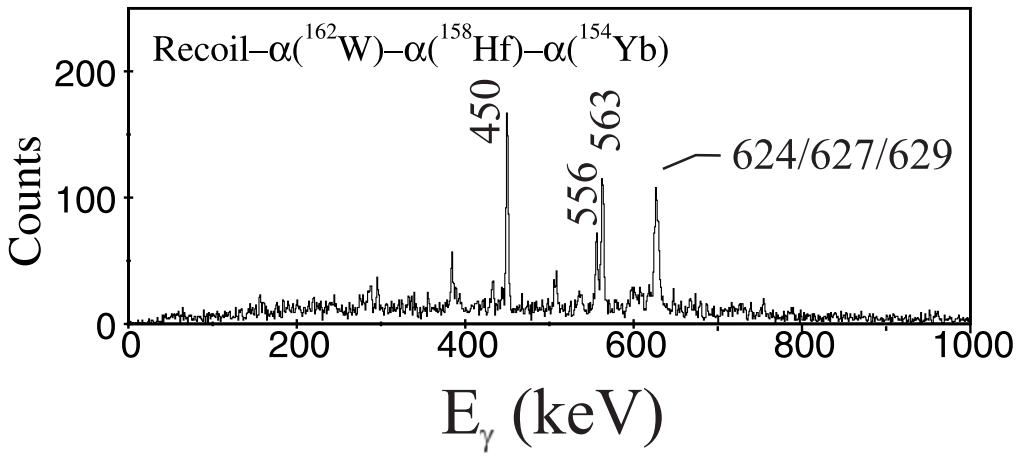

Figure 5.5: Gamma rays correlated with characteristic decays known to follow the implantation of a recoiling ^{162}W nucleus in the DSSD, this required the decay sequence $\alpha(^{162}\mathrm{W})$-$\alpha(^{158}\mathrm{Hf})$-$\alpha(^{154}\mathrm{Yb})$ to be completed within a single pixel. Correlation times between decays were limited to 3600, 9000 and 1300 ms, respectively.

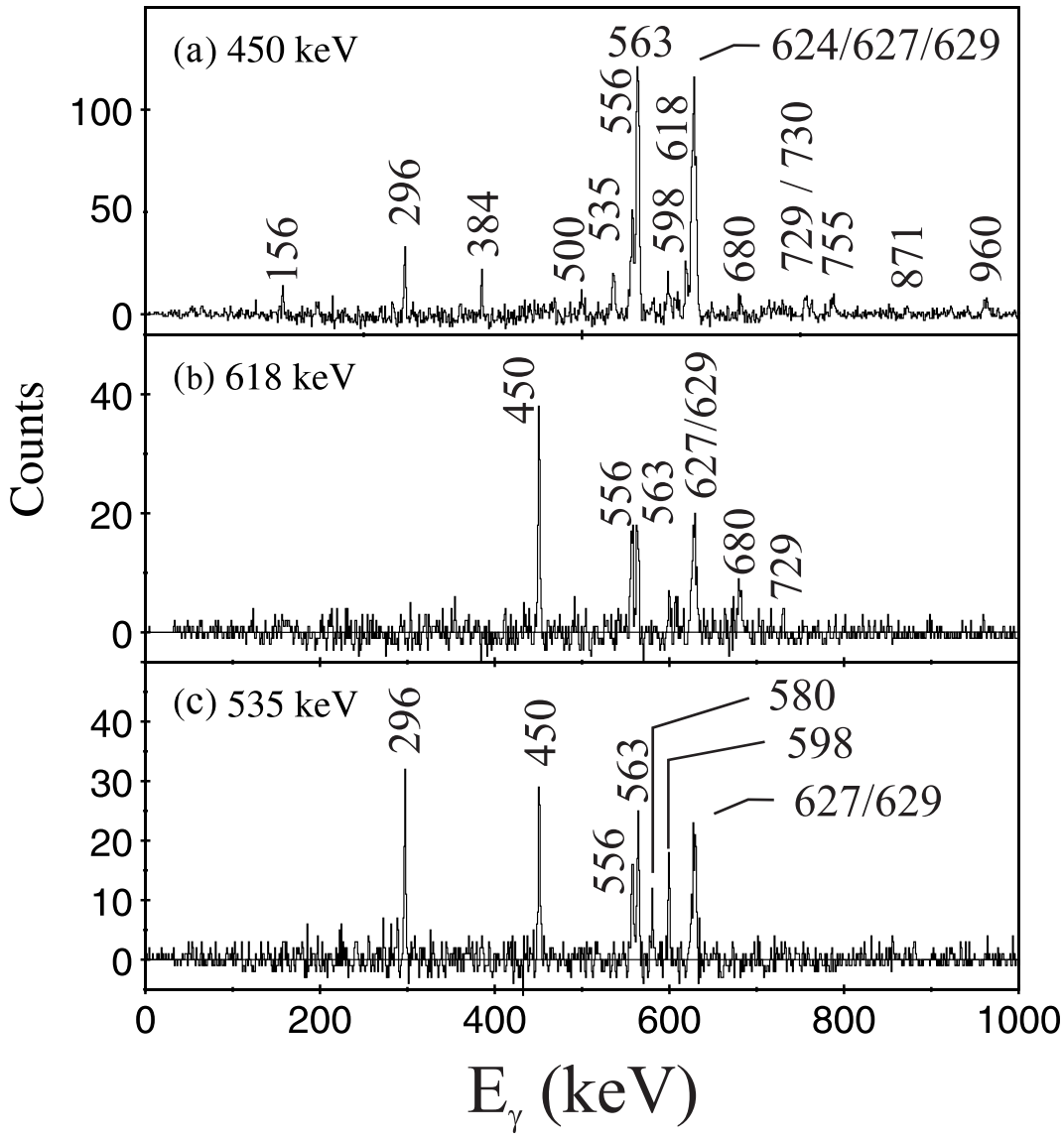

Figure 5.6: The following spectra were generated using a γ-γ matrix correlated with the decay of ^{162}W within 500-4800 ms of the implantation of a recoil, requiring a coincidence with transitions of energy; (a) 450keV (b) 618keV (c) 535keV.

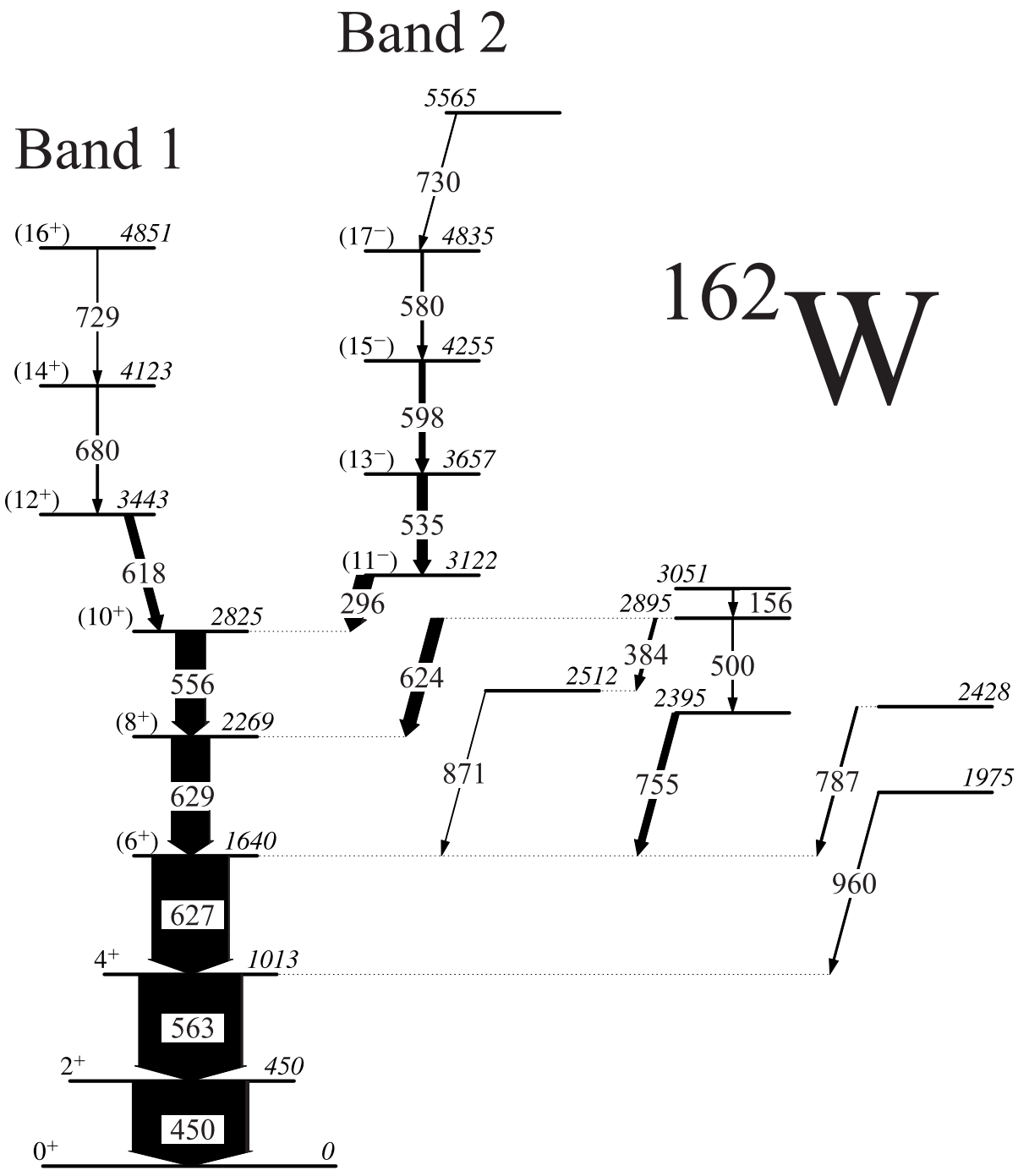

Figure 5.7: Level Scheme deduced for ^{162}W. Transition energies are given in keV and relative intensities are represented by arrow widths.

E_γ (keV)	I_γ (%)	R	I_i^π	$\rightarrow$	I_f^π	Band
156.1	4.2(7)					
295.9	15.0(13)		(11^-)	$\rightarrow$	(10^+)	$2 \rightarrow 1$
384.0	2.8(7)					
449.6	100.0(15)	1.2(2)	2^+	$\rightarrow$	0^+	1
499.8	1.5(6)					
535.0	9.0(6)		(13^-)	$\rightarrow$	(11^-)	2
556.2	26.1(18)		(10^+)	$\rightarrow$	(8^+)	1
562.8	90.0(6)	1.3(2)	4^+	$\rightarrow$	2^+	1
579.6	2.3(5)		(17^-)	$\rightarrow$	(15^-)	2
598.4	5.3(7)		(15^-)	$\rightarrow$	(13^-)	2
618.4	7.6(10)		(12^+)	$\rightarrow$	(10^+)	1
624.3	11.2(12)			$\rightarrow$	(8^+)	
626.6	67(4)		(6^+)	$\rightarrow$	4^+	1
629.1	33.5(24)		(8^+)	$\rightarrow$	(6^+)	1
680.4	2.0(5)		(14^+)	$\rightarrow$	(12^+)	1
728.6	1.1(4)		(16^+)	$\rightarrow$	(14^+)	1
730.4	1.1(4)			$\rightarrow$	(17^-)	
755.3	6.2(11)			$\rightarrow$	(6^+)	
787.4	2.0(7)			$\rightarrow$	(6^+)	
870.5	0.7(6)			$\rightarrow$	(6^+)	
960.4	1.6(8)			$\rightarrow$	(4^+)	

Table 5.1: Measured γ-ray transition properties for ^{162}W.

5.4 Discussion

The underlying quasiparticle configurations of structures in ^{162}W is discussed in terms of rotational alignments interpreted within the context of the cranked shell model. The collective behaviour of a number of valence nucleons outside of a closed shell is well known to be conveyed through the experimental yrast spectra. In many other works in this mass region the structure of a nucleus is discussed in terms of its aligned angular momentum and angular frequency. However, these values rely on the quantum number K, the projection of J onto the symmetry axis K, which is an ill-defined quantum number for γ-soft nuclei. In this work the initial spin, I_i of an emitting state is plotted against the γ-ray energy. Hereafter the

variation of I_i as a function of transition energy will be referred to as the alignment. Figure 5.8(a) shows that the ground-state band of ^{162}W is crossed by an aligned configuration. There is an alignment gain of $\sim 6\hbar$ at E_γ=600 keV ($\hbar\omega \sim 0.3$ Mev/$\hbar$). The experimental Routhians, shown in Figure 5.9, extracted from the level scheme also indicate a crossing frequency of 0.3 Mev/$\hbar$ for this alignment. These features can be interpreted in the context of Woods-Saxon cranking calculations [CDN$^+$87]. In these calculations, the pairing strength is modelled with a frequency dependent modification such that the pairing strength is reduced by 50% of the zero frequency value at $\hbar\omega$=0.7 MeV/$\hbar$ [WNJ$^+$88]. The quasiparticle Routhians calculated for ^{162}W are shown in Figure 5.11 where they are compared to calculations for ^{164}W. Quasiparticle Routhians, e$'$, have been calculated using quadrupole deformation parameters deduced from lifetime measurements performed by Doncel *et. al* (^{162}W 27(11) ps and ^{164}W 26(17) ps) [D$^+$17].

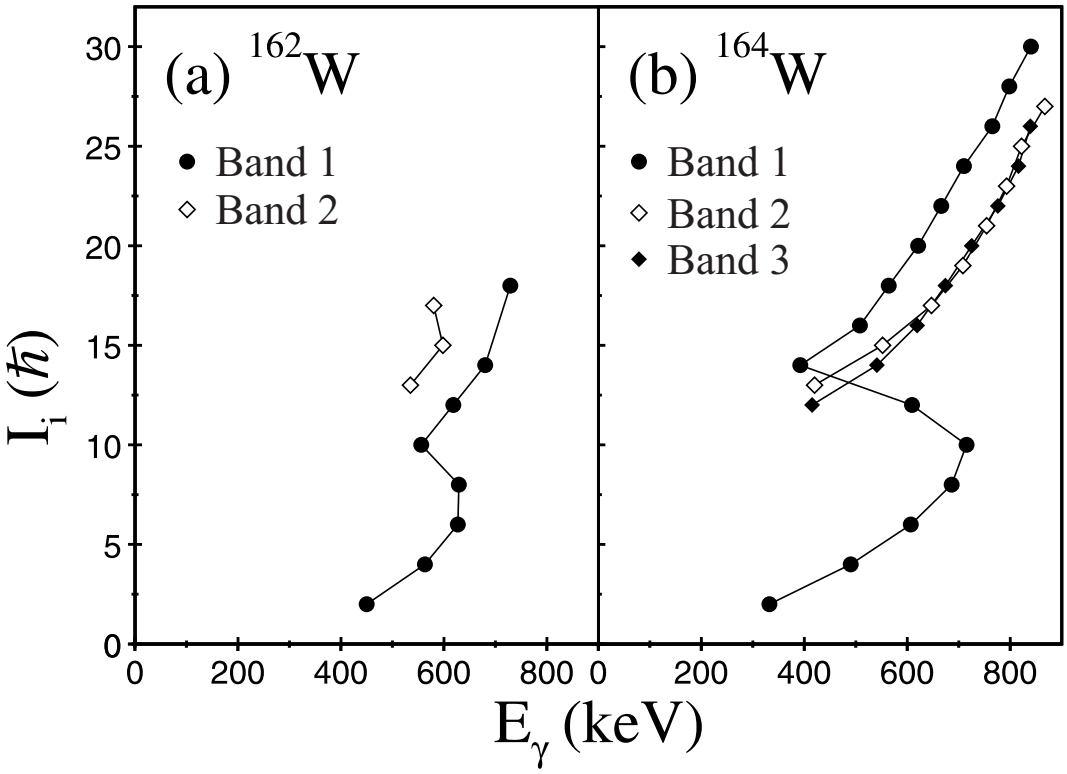

Figure 5.8: Initial spin I_i as a function of transition energy in Neutron-deficient 162W and 164W

These lifetimes can be converted into quadrupole deformation parameters, β_2. For

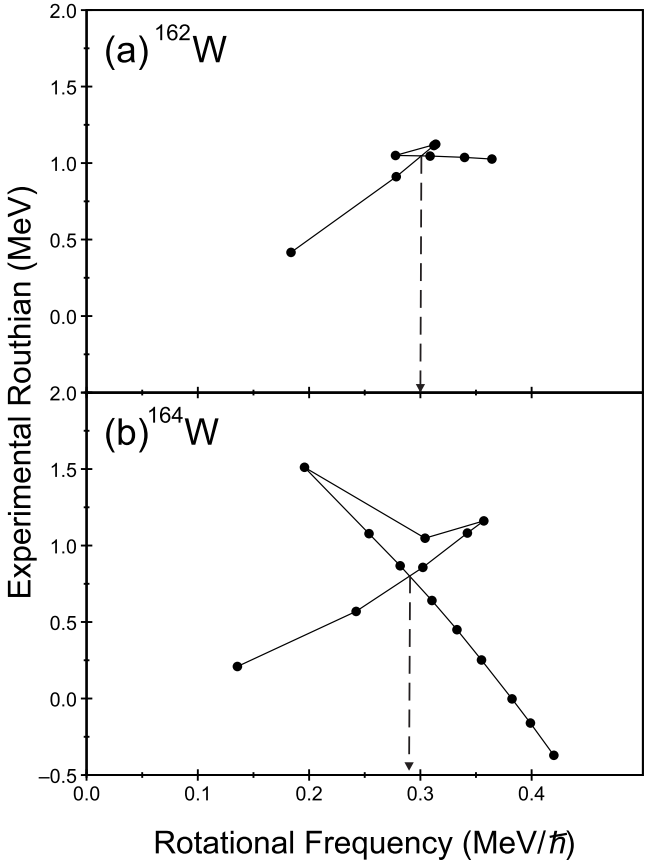

Figure 5.9: Routhians for ^{162}W (a) and ^{164}W (b)

E2 transitions the reduced transition probability is related to the lifetime of a transition between states I_i and I_f such that

$$B(E2; I_i \rightarrow I_f) = \frac{0.0816}{\tau E_\gamma^5 (1+\alpha)}, \tag{5.1}$$

where τ is the lifetime of the initial state and α is the conversion coefficient of the transition taken from [KBT$^+$08]. From this the transition quadrupole moments Q_t are calculated according to

$$B(E2; I_i \rightarrow I_f) = \frac{5}{16\pi} e^2 Q_t^2 \ \langle I_i 020 | I_f 0 \rangle^2, \tag{5.2}$$

by inserting the Clebsch-Gordon coefficients. Assuming a rigid rotor, with γ deformation = 0 Q_t becomes Q_0 and an approximation for the quadrupole moment is

calculated as a function of the deformation with

$$Q_0 = \frac{3}{\sqrt{5\pi}} R_{av}^2 \beta_2 (1 + 0.16\beta). \tag{5.3}$$

Deformation parameters β_2 for ^{162}W and ^{164}W have been extracted from the lifetimes measured by Doncel *et al.* to give 0.116 and 0.241, respectively. Calculated quasiparticle Routhians for ^{162}W and ^{164}W show that it is the neutrons that dominate effects on the nucleus at low frequency. Quasiparticle Routhians have been calculated as a function of rotational frequency for ^{162}W and ^{164}W using these quadrupole deformation parameters in the cranked shell model (CSM) formalism. The quasiparticle labelling convention is defined in Table 5.2.

The calculated Routhians for ^{162}W reproduce those crossing frequencies observed in experiment for the EF $\nu(h_{9/2})^2$ quasineutron configurations. Alignments can be extracted from the CSM calculations as the slope of the theoretical Routhian ($i_x = \frac{de'}{d\omega}$). The experimental alignment gain measured here $\Delta I_i \sim 6\hbar$ is consistent with the predicted EF alignment gain ($\sim 8\hbar$).

Band 2 in ^{162}W has an an initial alignment of $\sim 10\hbar$ at E_γ=600 keV ($\hbar\omega \sim 0.3$ Mev/$\hbar$). This is likely to be the AE two-particle alignment formed by coupling the $i_{13/2}$ neutron to the mixed $(h_{9/2}, f_{7/2})$ neutron orbital as observed in heavier even-even ^{164}W, shown in Figure 5.8(b). However the aligned $(i_{13/2})^2$ AB configuration also produces an alignment gain of $\sim 11.5\hbar$ and cannot be ruled out.

Figure 5.10 displays how the ground-state band of ^{162}W (d) differs from that of the lighter and heavier tungsten isotopes. The alignment plot for ^{162}W shows a backbend that can be interpreted in terms of quasiparticle alignments within the cranked shell model. This shows a marked difference to the lighter tungsten isotopes and suggests that ^{162}W is the first tungsten isotope to exhibit collective rotational excitations. A higher degree of alignment is seen in ^{164}W at a similar crossing frequency (see Figure 5.9). This has been interpreted as the alignment of a pair of

$i_{13/2}$ neutrons (AB). The cranked shell model calculations shown in figure 5.11(c) show that the AB alignment is favoured over the negative-parity EF configuration. Quasiparticle Routhians are highly sensitive to the deformation of the system and a comparison of the quasineutron Routhians for the two nuclei shows a significant drop in the frequency required to align a pair of negative parity $h_{9/2}$ or $f_{7/2}$ neutrons. These negative-parity orbitals compete with the $i_{13/2}$ quasineutron alignment, which dominates at in the heavier isotopes as the $i_{13/2}$ orbital increases in energy relative to the Fermi surface with decreasing deformation.

Routhians were also calculated for ^{162}W by Li *et. al* using deformation parameters predicted by Total Routhian Surface calculations ($\beta_2 = 0.146$ and $\beta_4 = 0.010$). These calculations give the (EF) alignment at an even lower frequency relative to the (AB) than those given above. It should be noted that the large uncertainties on the measured lifetimes and the exclusion of γ deformation from CSM calculations could have an effect on the calculated crossing frequencies.

The blocking of the AB crossing in the odd-A W isotopes enables a clearer picture of the effect of deformation on the relative positions of orbitals close to the Fermi surface and aids in elucidating these effects in its even-A neighbours. The observation of the increasing energy of the $i_{13/2}$ orbital relative to the Fermi surface as a function of decreasing deformation is also supported by alignment properties in the

Label	Parity & Signature (π, α)	Shell Model State
	Quasineutrons	
A	$(+, +1/2)_1$	$i_{13/2}$
B	$(+, -1/2)_1$	$i_{13/2}$
C	$(+, +1/2)_2$	$i_{13/2}$
E	$(-, -1/2)_1$	$h_{9/2}, f_{7/2}$
F	$(-, +1/2)_1$	$h_{9/2}, f_{7/2}$
	Quasiprotons	
e	$(-, -1/2)_1$	$h_{11/2}$
f	$(-, +1/2)_1$	$h_{11/2}$

Table 5.2: Labelling convention for quasiparticles.

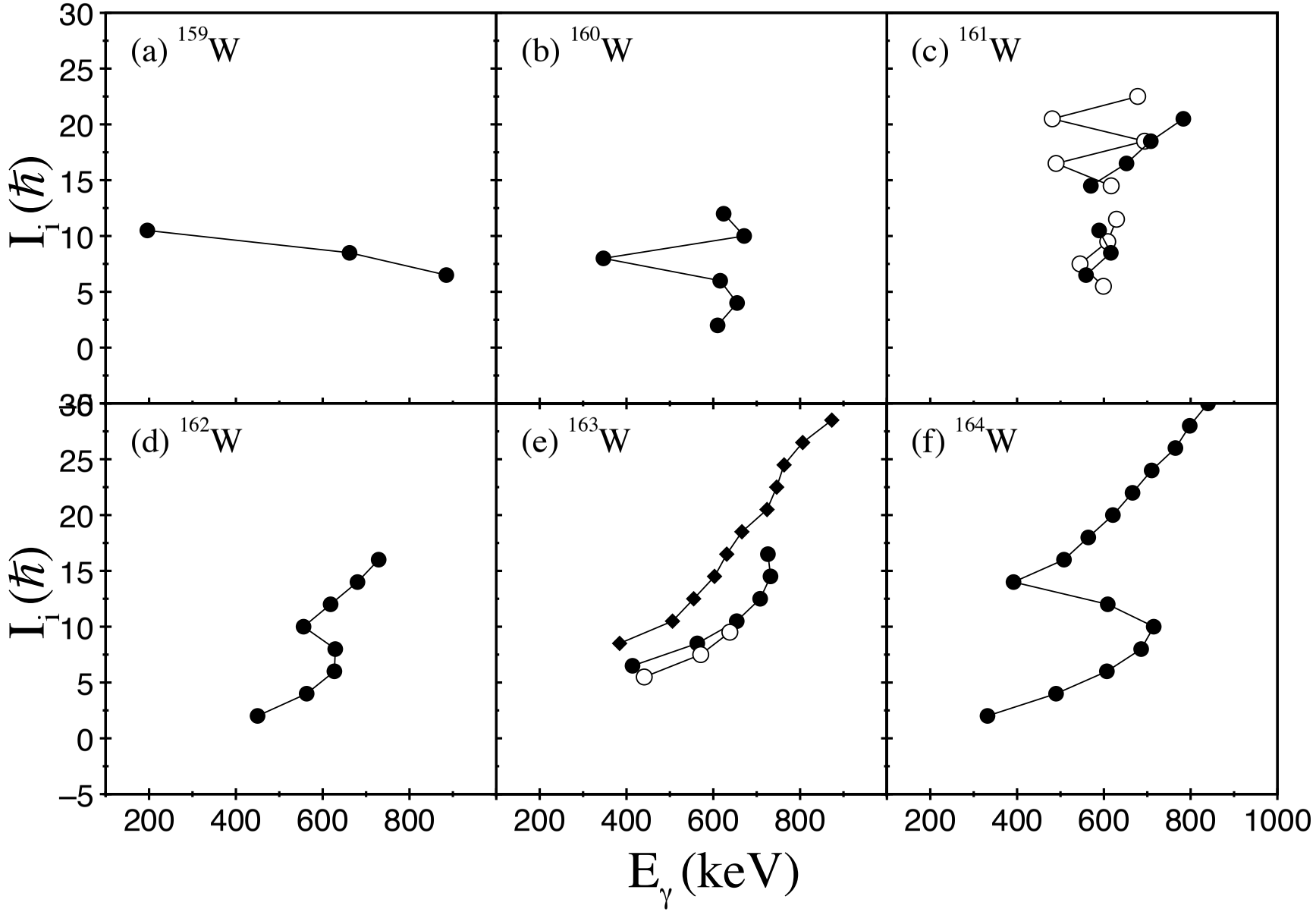

Figure 5.10: Initial spin I_i as a function of transition energy in neutron-deficient $^{159-164}$W

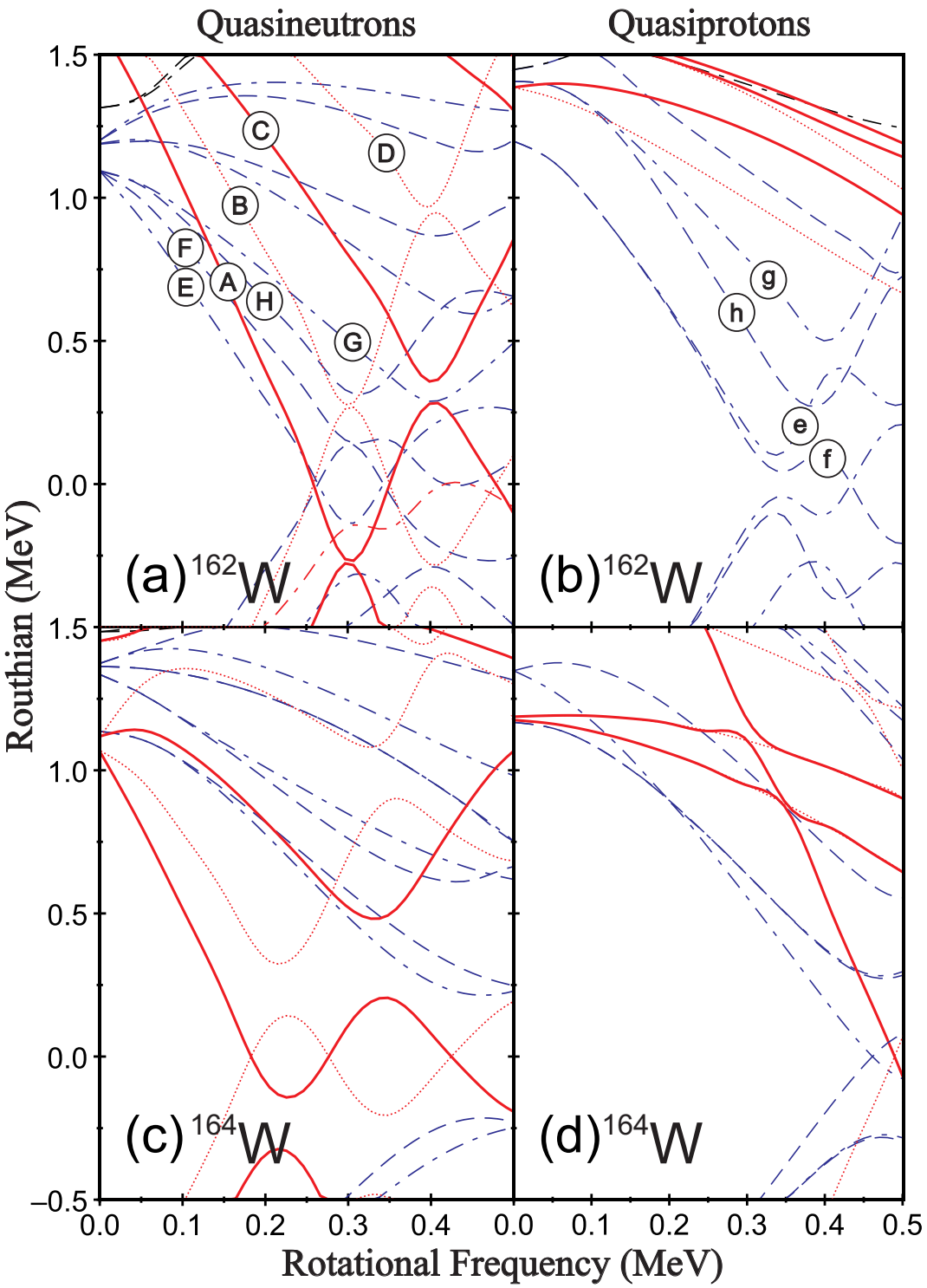

Figure 5.11: Quasiparticle Routhians calculated using a Woods-Saxon potential and quadrupole deformation parameters extracted from measured lifetimes [D$^+$17]. (a) quasineutron calculations for ^{162}W. (b) quasiproton calculations for ^{162}W . (c) Quasineutrons calculations for ^{164}W. (d) Quasiproton calculations for ^{164}W.

intervening odd-A isotope ^{163}W shown in figure 5.10(e). The first band crossing in odd-Mass, $N > 88$ W isotopes is typically assumed to be due to the alignment of the second $i_{13/2}$ (BC) neutron pair. Thomson *et al.* showed the yrast band of ^{163}W exhibits two band-crossings [T^{+}10]. The alignment pattern measured did not follow that of the heavier odd-N isotopes. Instead the first alignment at $\hbar\omega = 0.3$ MeV was assigned to the alignment of a $(h_{9/2}, f_{7/2})^2$ neutron pair. The second crossing frequency at $\hbar\omega = 0.37$ MeV was attributed to either the BC $i_{13/2}$ neutron alignment or the ef $h_{11/2}$ proton alignment.

A similar picture of these neutron alignments is seen the neighbouring odd-Z isotones ^{161}Ta and ^{163}Ta [S^{+}09, L^{+}11] shown in Figure 5.12. The AB neutron alignments are seen in ^{163}Ta, where an odd proton hole is coupled to the ^{164}W core. However a large signature splitting is seen at low spin, which indicates a γ-soft nucleus. Beyond the first crossing a smooth increase in spin is seen with zero signature splitting, which is indicative of an axial prolate shape at high spin following the AB neutron alignment and the subsequent gradual alignment of a pair of $h_{11/2}$ protons. Although both signatures of band 1 in ^{161}Ta display a similar change in alignment at the first crossing to the EF neutron alignment in ^{162}W, there is a large signature splitting that does not disappear in the aligned configurations. This indicates the alignment of the negative-parity orbitals has a lesser core-polarising influence on the triaxial deformation of the core nucleus at high spin. From these comparisons with the odd-z isotones it is inferred that the tungsten cores will have a similar degree of triaxial deformation. This is consistent with the measured $E(4+)/E(2+)$ ratios.

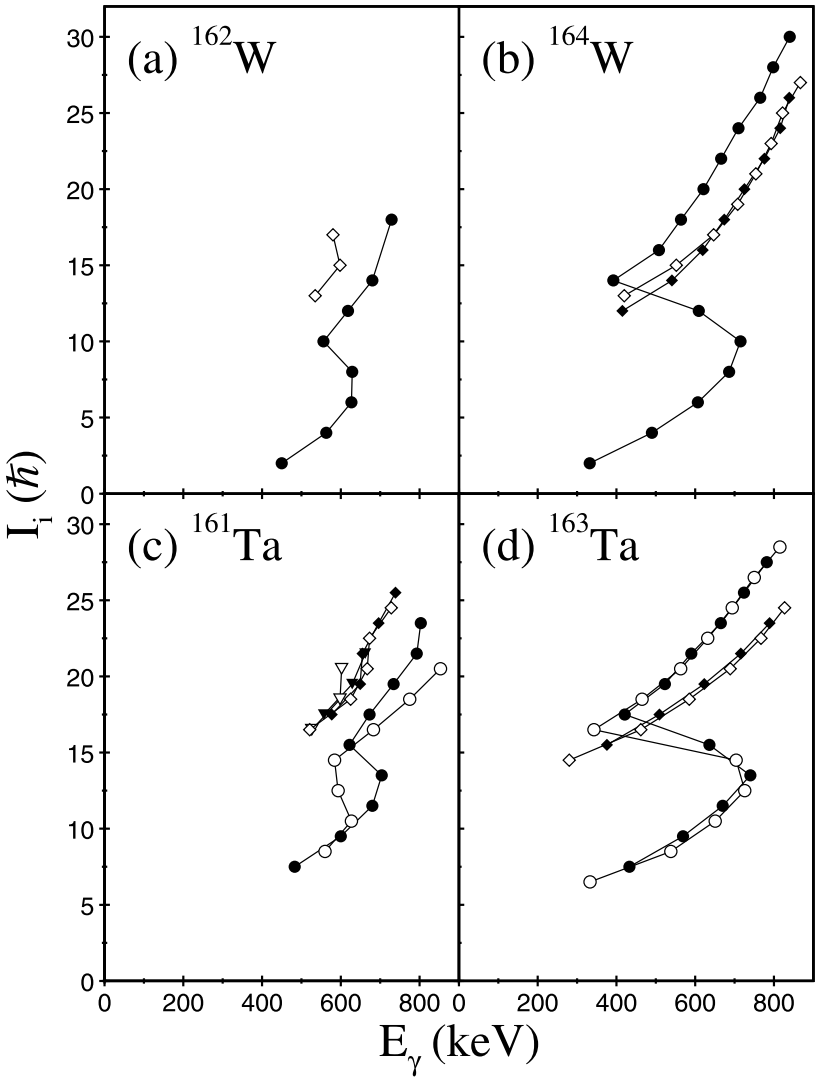

Figure 5.12: Angular momentum of the emitting state I_i as a function of γ-ray energy for collective bands in (a) ^{162}W (b) ^{164}W (c) ^{161}Ta (d) ^{163}Ta. Open (filled) circles correspond to the $\alpha = +1$ ($\alpha = -1$) signature partner in W isotopes or $\alpha = +1/2$ ($\alpha = -1/2$) signature partners in Ta isotopes.

Chapter 6

Conclusion

This thesis reports the discovery of new excited states in the light tungsten isotopes ^{161}W and ^{162}W. These have been identified using selective recoil decay tagging techniques performed with the Jurogam and GREAT spectrometers in conjuction with the RITU gas-filled separator at the university of Jyäskylä, Finland.

The nucleus ^{161}W has established excited states to a tentative spin of $45/2^{-}$. The level scheme has been interpreted in terms of non-collective multiparticle structures based on valence nucleons occupying the $f_{7/2}$,$h_{9/2}$ $i_{13/2}$ neutron orbitals and $h_{11/2}$ proton orbitals, respectively. The maximally aligned configurations of multiplets based on one, three, five and seven quasiparticle excitations have been identified for the first time.

The level scheme of heavier isotope ^{162}W has been extended to higher spins and includes the addition of an excited band structure. These structures have been interpreted in terms of rotational alignments within the theoretical context of the cranked shell model. Alignments and crossing frequencies have been compared with quasiparticle Routhians and indicate that the yrast structure of ^{162}W can be interpreted as a collective rotor. The first rotational alignment is assigned to be the EF $(f_{7/2}, h_{9/2})^2$ neutron configuration. This is different to the first alignment in the

heavier even-A isotope ^{164}W, which exhibits an alignment gain consistent with the $(i_{13/2})^2$ neutron configuration. This indicates an increase in deformation with the addition of neutrons to the $N = 82$ closed shell. Comparisons of these isotopes with their light, odd-Z isotones ^{161}Ta and ^{163}Ta indicate that at low spin the tungsten cores have a γ-soft triaxial deformation. From this work and comparison with both lighter and heavier tungsten isotopes ^{162}W appears to be the first tungsten isotope to exhibit collective rotational excitations This indicates a threshold of collectivity for neutron-deficient tungsten isotopes above the $N = 82$ shell closure.

Further work is necessary to establish precise measures of the deformation in these isotopes.

Bibliography

[A+76] G Andersson et al. Nuclear shell structure at very high angular-momentum. *Nucl. Phys. A*, 268(2):205–256, 1976.

[B+92] C.W. Beausang et al. Measurements on prototype Ge and BGO detectors for the Eurogam array. *Nucl. Instrum. Meth. A*, 313(1–2):37, 1992.

[B+99] R.A. Bark et al. Bandcrossings in Os-171. *Nucl. Phys. A*, 646(4):399 – 413, 1999.

[Baz92] D. Bazzacco. Gasp collaboration report. *Proceedings of the Workshop on Large gamma-ray Detector Arrays, Chalk River, Canada*, page 376, 1992.

[BFM86] R. Bengtsson, S. Frauendorf, and F.-R. May. Quasiparticle levels in rotating rare earth nuclei: A cranked shell-model dictionary. *At. Data. Nucl. Data Tables*, 35(1):15 – 122, 1986.

[Boh40] N. Bohr. Scattering and stopping of fission fragments. *Phys. Rev.*, 58:654–655, 1940.

[BS96] C.W Beausang and J Simpson. Large arrays of escape suppressed spectrometers for nuclear structure experiments. *J Phys G*, 22(5):527, 1996.

[CDN+87] S Cwiok, J Dudek, W Nazarewicz, J Skalski, and T Werner. Single-particle energies, wave-functions, quadrupole-moments and g-factors

in an axially deformed woods-saxon potential with applications to the 2-center-type nuclear problems. *Comput. Phys. Commun.*, 46(3):379–399, 1987.

[D+92] G.D. Dracoulis et al. Spectroscopy of very neutron-deficient hafnium and tungsten isotopes. *Proceedings of the International Conference of Nuclear Structure at High Angular Momentum*, 1992.

[D+13] M. C. Drummond et al. Low-lying excited states in the neutron-deficient isotopes Os-163 and Os-165. *Phys. Rev. C*, 87(5), 2013.

[D+17] M. Doncel et al. Lifetime measurements of excited states in W-162 and W-164 and the evolution of collectivity in rare-earth nuclei. *Phys. Rev. C*, 95(4), 2017.

[DCS+00] KY Ding, JA Cizewski, D Seweryniak, et al. High-spin excitations in Hf-158,Hf-159,Hf-160 from recoil-decay tagging. *Phys. Rev. C*, 62(3), Sep 2000.

[DDFB82] J.L. Durell, G.D. Dracoulis, C. Fahlander, and A.P. Byrne. Contrasting high-spin yrast bands in Os-172 and Os-174 and an unexpected low-frequency anomaly in Os-172. *Phys. Lett. B*, 115(5):367 – 371, 1982.

[DFS+91] GD Dracoulis, B Fabricius, AE Stuchbery, AO Macchiavelli, W Korten, F Azaiez, E Rubel, MA Deleplanque, RM Diamond, and FS Stephens. Shape coexistence from the structure of the yrast band in Pt-174. *Phys. Rev. C*, 44(4):R1246–R1249, 1991.

[DM+15] T. R. Davis-Merry et al. Collective excitations in the transitional nuclei Re-163 and Re-165. *Phys. Rev. C*, 91(3), 2015.

[E29] Rutherford E. Discussion on the structure of atomic nuclei. *Roy. Soc, Proc A*, 123:386, 1929.

[Eec06] S. Eeckhaudt. Spectroscopy in the transfermium region: probing rotational, non-yrast and isomeric structures in No-253,254. *Thesis, University of Jyväskylä*, 2006.

[FP77] P Federman and S Pittel. Towards a unified microscopic description of nuclear deformation. *Phys. Lett. B*, 69(4):385–388, 1977.

[FP79] P Federman and S Pittel. Unified shell-model description of nuclear-deformation. *Phys. Rev. C*, 20(2):820–829, 1979.

[G+05] P.T Greenlees et al. Heavy element spectroscopy at jyfl. *AIP Conf. Proc.*, 764(1), 2005.

[Gam28] G. Gamow. The quantum theory of nuclear disintegration. *Nature*, 1928.

[GC28] R. W. Gurney and E. U. Condon. Wave mechanics and radioactive disintegration. *Nature*, 122:439, 1928.

[GTH65] SR. De Groot, HA. Tolhoek, and WJ Huiskamp. In K. Siebahn, editor, *Alpha-, beta- and gamma-ray spectroscopy*, volume 2, chapter Orientation of Nuclei at Low Temperatures, page 1199. North-Holland Pub. co., Amsterdam, 1965.

[GYL+88] A Ghiorso, S Yashita, M Leino, L Frank, J Kalnins, P Armbruster, Jp Dufour, and Pk Lemmertz. Sassy, A Gas-Filled Magnetic Separator For The Study Of Fusion Reaction-Products. *Nucl. Instrum. Meth. A*, 269(1):192–201, 1988.

[Har64] SM. Harris. Large-spin rotational states of deformed nuclei. *Phys. Rev. Lett.*, 13:663–665, 1964.

[Hey04] Kris L. G. Heyde. *Basic ideas and concepts in nuclear physics : an introductory approach.* Series in fundamental and applied nuclear physics. Bristol : Institute of Physics, 2004., 2004.

[HFM+79] S. Hofmann, W. Faust, G. Münzenberg, W. Reisdorf, P. Armbruster, K. Güttner, and H. Ewald. Alpha decay studies of very neutron deficient isotopes of Hf, Ta, W, and Re. *Z. Phys A*, 291(1):53–70, 1979.

[HJS49] O Haxel, J. Hans D. Jensen, and Hans E. Suess. On the "magic numbers" in nuclear structure. *Phys. Rev.*, 75:1766–1766, 1949.

[Ing54] D. R. Inglis. Particle derivation of nuclear rotation properties associated with a surface wave. *Phys. Rev.*, 96:1059–1065, 1954.

[J+11] D. T. Joss et al. The influence of quasineutron configurations on Ta-161 and nearby odd-A nuclei. In *4Th International Conference On Proton Emitting Nuclei And Related Topics*, volume 1409 of *AIP Conference Proceedings*, 2011. 4th International Conference on Proton Emitting Nuclei and Related Topics, Bordeaux, France, 2011.

[J+17] D. T. Joss et al. Spectroscopy at the two-proton drip line: Excited states in W-158. *Phys. Lett. B*, 772, 2017.

[JLA+04] D. T. Joss, K. Lagergren, D. E. Appelbe, et al. Recoil decay tagging of γ rays in the extremely neutron-deficient nucleus Os-162. *Phys. Rev. C*, 70:017302, Jul 2004.

[K+01] A Keenan et al. First observation of excited states in the neutron deficient N=86 isotones Ta-159 and W-160. *Phys. Rev. C*, 63(6), 2001.

[K+04] H Kettunen et al. Decay studies of Au-170,171, Hg-171-173, and Tl-176. *Phys. Rev. C*, 69(5), 2004.

[KBT+08] T. Kibedi, T. W. Burrows, M. B. Trzhaskovskaya, P. M. Davidson, and C. W. Nestor, Jr. Evaluation of theoretical conversion coefficients using BrIcc. *Nucl. Instrum. Meth. A*, 589(2):202–229, 2008.

[Kra88] Kenneth S. Krane. *Introductory nuclear physics.* New York ; Wiley, 1988., 1988.

[L+95] M Leino et al. Gas-Filled Recoil Separator For Studies Of Heavy-Elements. *Nucl. Instrum. Meth. B*, 99(1-4):653–656, 1995.

[L+01] I. Lazarus et al. The GREAT triggerless total data readout method. *IEEE Transactions on Nuclear Science*, 48(3):567–569, 2001.

[L+11] K. Lagergren et al. γ-soft shapes and quasiparticle excitations in Ta-161. *Phys. Rev. C*, 83:014313, 2011.

[L+15] H. J. Li et al. Recoil-decay tagging spectroscopy of W-162. *Phys. Rev. C*, 92(1), 2015.

[May50] Maria Goeppert Mayer. Nuclear configurations in the spin-orbit coupling model. I. empirical evidence. *Phys. Rev.*, 78:16–21, 1950.

[MNMW95] P. Moller, J.R. Nix, W.D. Myers, and Swiatecki W.J. Nuclear ground-state masses and deformations. *At. Data. Nucl. Data Tables*, 59(2):185 – 381, 1995.

[MS74] E. Der Mateosian and A.W. Sunyar. Tables of attenuation coefficients for angular distribution of gamma rays from partially aligned nuclei. *At. Data. Nucl. Data Tables*, 13(4):391 – 406, 1974.

[NBF94] P J Nolan, F A Beck, and D B Fossan. Large arrays of escape-suppressed gamma-ray detectors. *Annu. Rev. Nucl. Part. Sci.*, 44(1):561–607, 1994.

[Nil55] S.G. Nilsson. Binding States of Individual Nucleons in Strongly Deformed Nuclei. *Mat. Fys. Medd. K. Dan. Vidensk. Selsk.*, 29:1–69, 1955.

[Nol90] PJ Nolan. Eurogam — a high efficiency escape suppressed spectrometer array. *Nucl. Phys. A*, 520:c657 – c667, 1990. Nuclear Structure in the Nineties.

[O+09] D. O'Donnell et al. Spectroscopy of the neutron-deficient nucleus Os-167. *Phys. Rev. C*, 79(6), 2009.

[P+03] R.D Page et al. The GREAT spectrometer. *Nucl. Instrum. Meth. B*, 204:634, 2003.

[P+09] E. S. Paul et al. Loss of collectivity in the transitional Er-156 nucleus at high spin. *Phys. Rev. C*, 79(4), 2009.

[PWC+96] R. D. Page, P. J. Woods, R. A. Cunningham, T. Davinson, N. J. Davis, A. N. James, K. Livingston, P. J. Sellin, and A. C. Shotter. Radioactivity of neutron deficient isotopes in the region N $<$ 82 $<$ Z. *Phys. Rev. C*, 53:660, 1996.

[PWD+95] E. S. Paul, P. J. Woods, T. Davinson, et al. In-beam γ-ray spectroscopy above Sn-100 using the new technique of recoil decay tagging. *Phys. Rev. C*, 51:78–87, Jan 1995.

[R+10] P. Rahkila et al. Shape coexistence at the proton drip-line: First identification of excited states in Pb-180. *Phys. Rev. C*, 82(011303), 2010.

[Rad95] D.C Radford. ESCL8R and LEVIT8R: Software for interactive graphical analysis of HPGe coincidence data sets. *Nucl. Instrum. Meth. A*, 361(1–2):297 – 305, 1995.

[Rah08] P. Rahkila. Grain-A Java data analysis system for Total Data Readout. *Nucl Instrum Meth A*, 595(3):637–642, 2008.

[S+05] D Seweryniak et al. Multiparticle configurations in N=84 isotones located at the proton drip line. *Phys. Rev. C*, 71(5), 2005.

[S+09] M. Sandzelius et al. γ-ray spectroscopy of Ta-163. *Phys. Rev. C*, 80:054316, 2009.

[S+10] C. Scholey et al. Isomeric and ground-state properties of Pt-171, Os-167, and W-163. *Phys. Rev. C*, 81(1), 2010.

[S+11] Sapple, P. J et al. In-beam γ-ray spectroscopy of the $N = 85$ isotones W-159 and Re-160. *Phys. Rev. C*, 84:054303, 2011.

[SHR+92] J Simpson, F Hanna, M A Riley, A Alderson, M A Bentley, A M Bruce, D M Cullen, P Fallon, and L Walker. High-spin gamma-ray spectroscopy of W-165 and W-166. *J Phys G*, 18(7):1207–1225, 1992.

[SRA+91] J Simpson, M A Riley, A Alderson, M A Bentley, A M Bruce, D M Cullen, P Fallon, F Hanna, and L Walker. Yrast band spectroscopy of W-164 and the systematics of the 1st i13/2 Neutron backbend in the neutron deficient rare-earth nuclei. *J Phys G*, 17(4):511–523, 1991.

[SSH+86] R. S. Simon, K. H. Schmidt, F. P. Heßberger, S. Hlavac, M. Honusek, G. Münzenberg, H. G. Clerc, U. Gollerthan, and W. Schwab. Evidence For Nuclear Shape Coexistence In Hg-180. *Z. Phys. A*, 325(2):197–202, 1986.

[T+92] K. Theine et al. High-spin structure of W-167 and W-168. *Nucl. Phys. A*, 548(1):71–101, 1992.

[T+10] J. Thomson et al. Competing quasiparticle configurations in w-163. *Phys. Rev. C*, 81(014307), 2010.

[TFL49] CH Townes, HM Foley, and W Low. Nuclear Quadrupole Moments And Nuclear Shell Structure. *Phys. Rev.*, 76(9):1415–1416, 1949.

[WNJ+88] R Wyss, J Nyberg, A Johnson, R Bengtsson, and W Nazarewicz. Highly deformed intruder bands in the A$\sim$130 mass region. *Phys. Lett. B*, 215(2):211–217, 1988.

[WS54] RD Woods and DS Saxon. Diffuse Surface Optical Model For Nucleon-Nuclei Scattering. *Phys. Rev.*, 95(2):577–578, 1954.

[X+13] C. Xu et al. Spectroscopy of Yb-157 and structure evolutions in odd-A Yb isotopes. *Phys. Rev. C*, 87(3), 2013.

[Yam67] T. Yamazaki. Tables of coefficients for angular distribution of gamma rays from aligned nuclei. *Nucl. Data, Sec. A*, 3(1):1 – 23, 1967.

[Z+96] CT Zhang et al. Complete valence particle yrast lines in N=84 nuclei above gadolinium. *Phys. Rev. C*, 54(1):R1–R5, 1996.

Appendix

Here are contained the fits to angular distribution of oriented states for excited states in ^{161}W. Intensities were measured at each ring of the Jurogam detector, $157.6°, 133.57°, 107.94°, 94.16°, 85.84°$ and $72.05°$. Intensities were normalised about 1, and fit to function

$$W(\theta) = 1 + A_2 P_2(cos\theta) + A_4 P_4(cos\theta), \tag{1}$$

so as to calculate angular distribution coefficients A_k. Further information on this is given in section 3.9.2 and values displayed on figures are also listed in table 5.1, in some cases outliers have been removed to improve the fit.

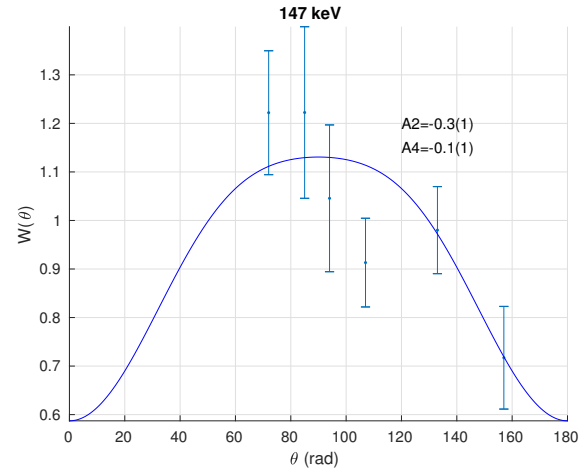
147 keV
A2=-0.3(1)
A4=-0.1(1)
W(θ)
θ (rad)

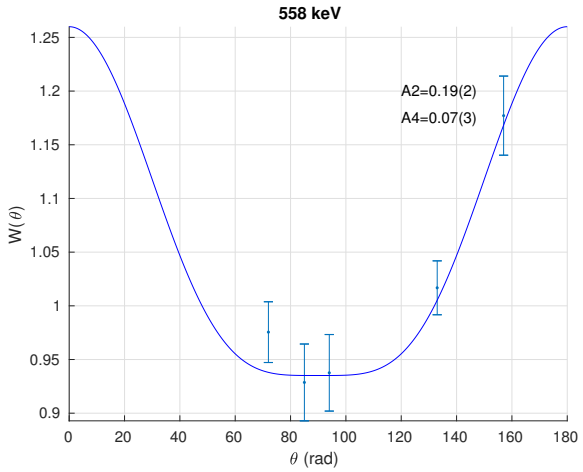
558 keV
A2=0.19(2)
A4=0.07(3)
W(θ)
θ (rad)

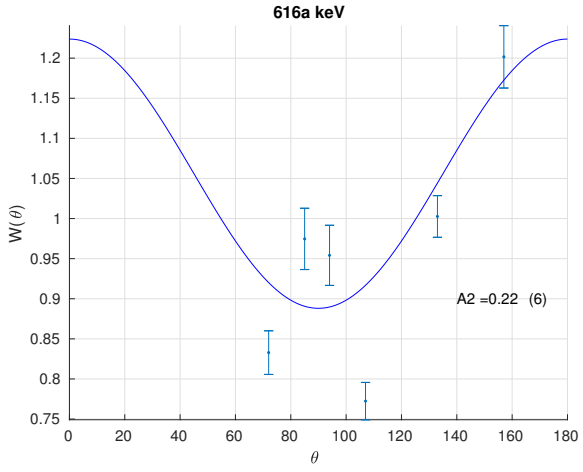
616a keV
A2 =0.22 (6)
W(θ)
θ

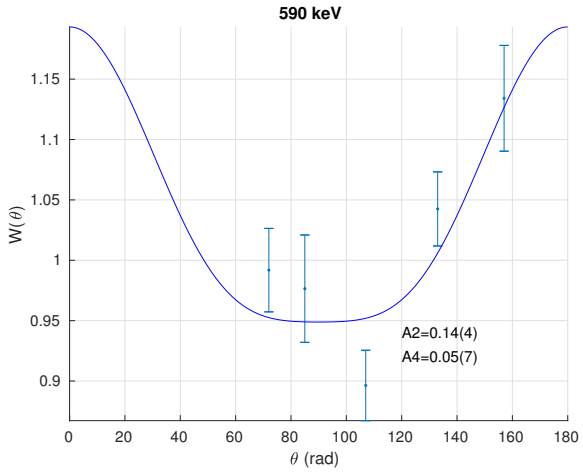
590 keV
A2=0.14(4)
A4=0.05(7)
W(θ)
θ (rad)

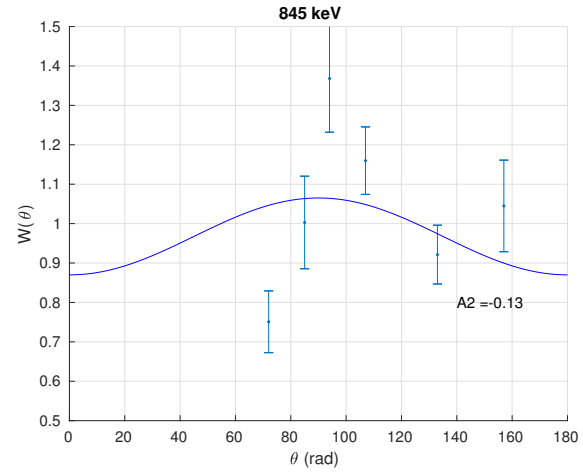
845 keV
A2 =-0.13
W(θ)
θ (rad)

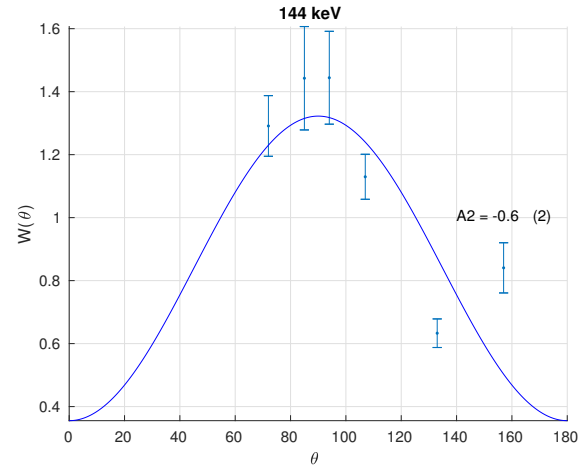
144 keV
A2 = -0.6 (2)
W(θ)
θ

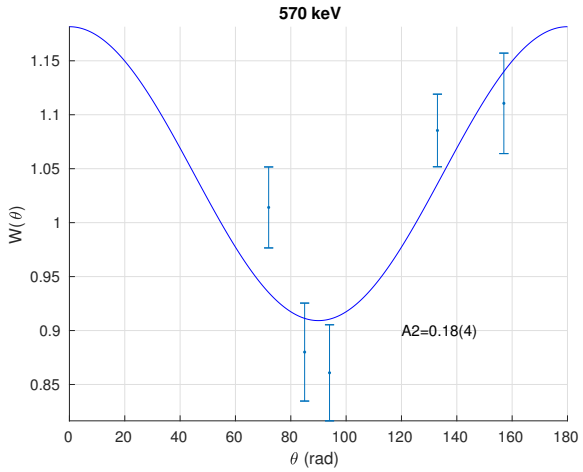
570 keV
W(θ)
θ (rad)
A2=0.18(4)

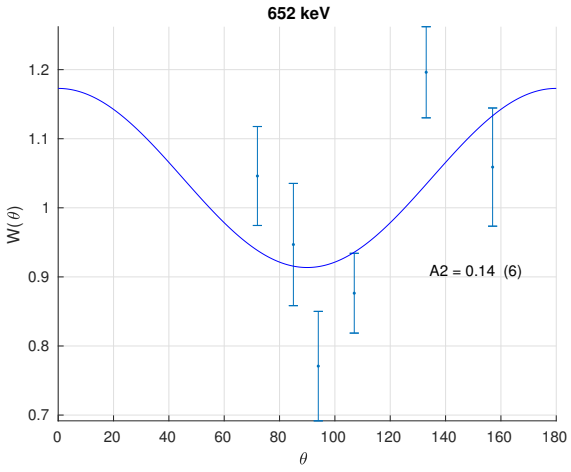
652 keV
W(θ)
θ
A2 = 0.14 (6)

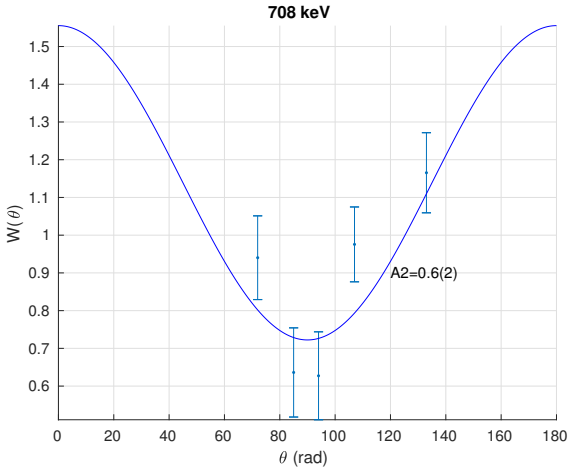
708 keV
W(θ)
θ (rad)
A2=0.6(2)

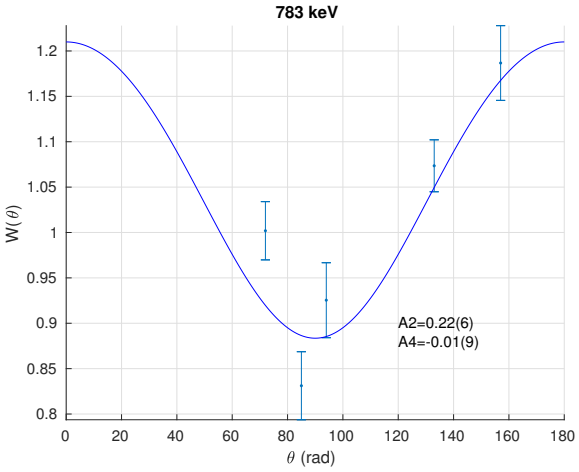
783 keV
W(θ)
θ (rad)
A2=0.22(6)
A4=-0.01(9)

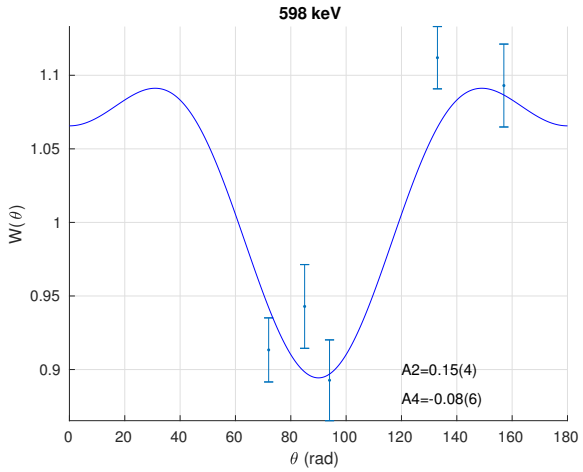
598 keV
W(θ)
θ (rad)
A2=0.15(4)
A4=-0.08(6)

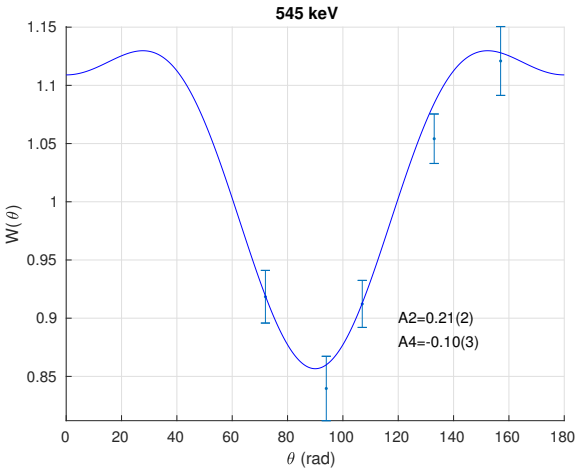
545 keV
W(θ)
θ (rad)
A2=0.21(2)
A4=-0.10(3)

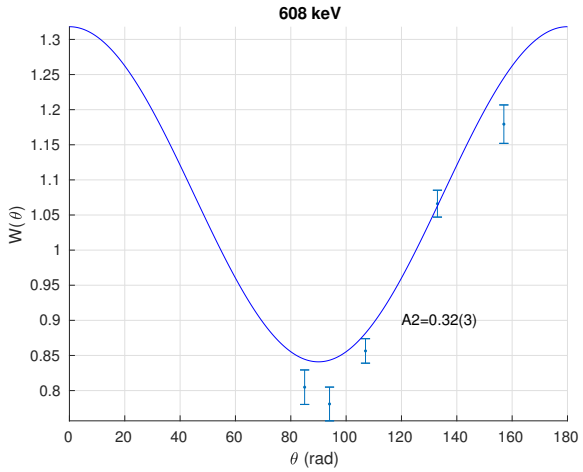
608 keV
W(θ)
θ (rad)
A2=0.32(3)

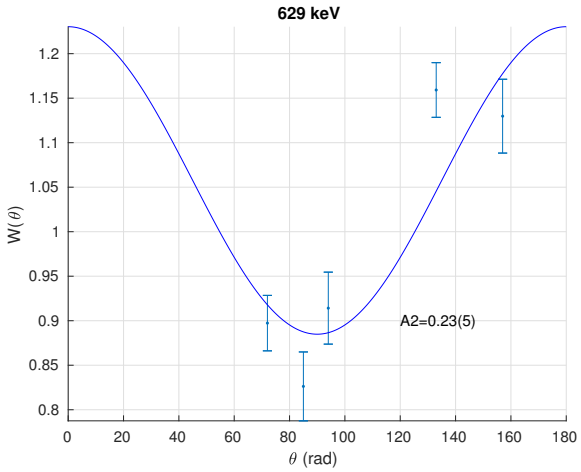
629 keV
W(θ)
θ (rad)
A2=0.23(5)

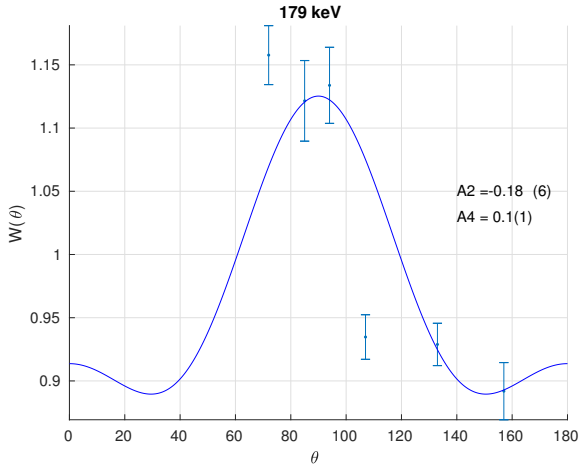
179 keV
W(θ)
θ
A2 =-0.18 (6)
A4 = 0.1(1)

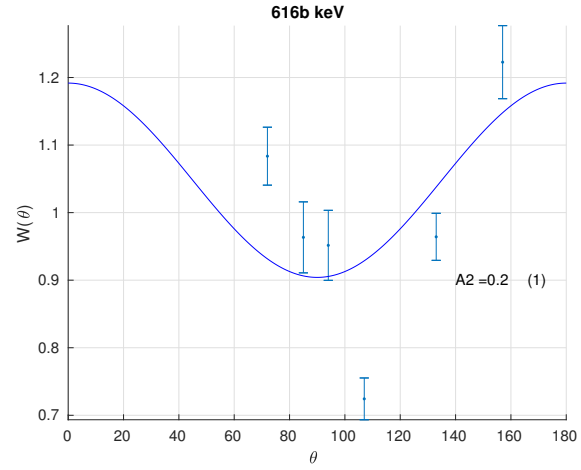
616b keV
W(θ)
θ
A2 =0.2 (1)

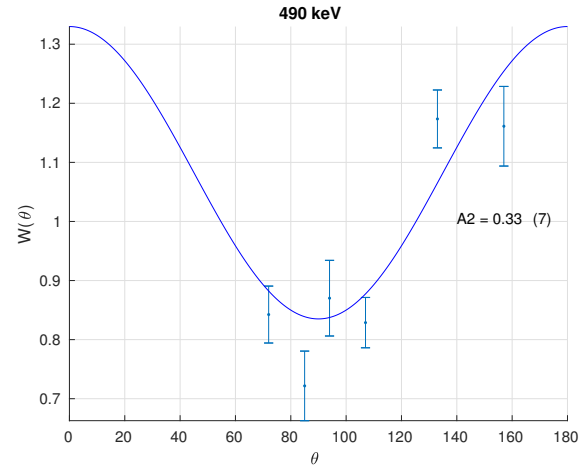
490 keV
W(θ)
θ
A2 = 0.33 (7)

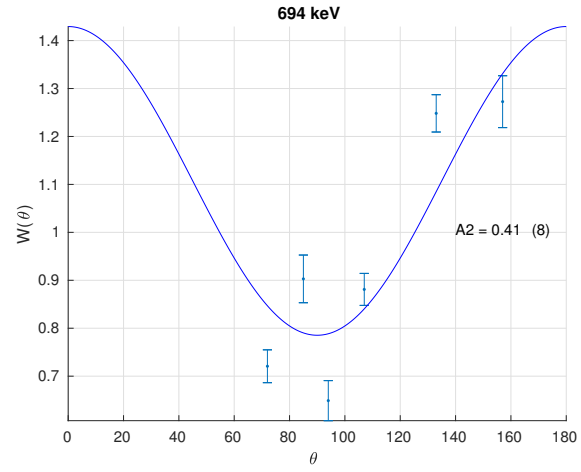
694 keV
W(θ)
θ
A2 = 0.41 (8)

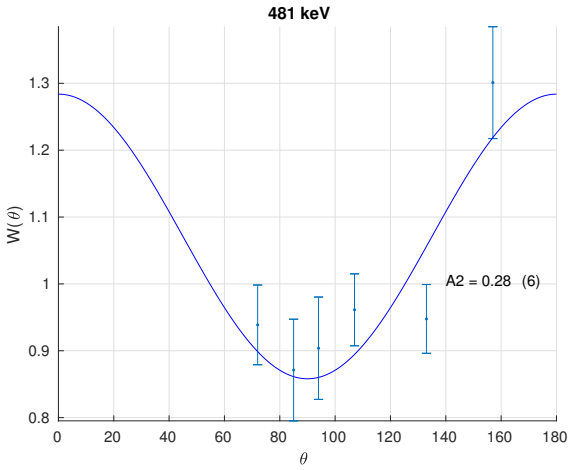
481 keV
W(θ)
θ
A2 = 0.28 (6)

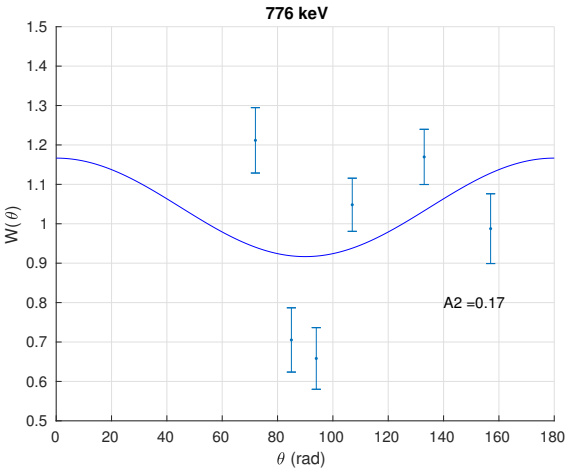
776 keV
W(θ)
θ (rad)
A2 =0.17

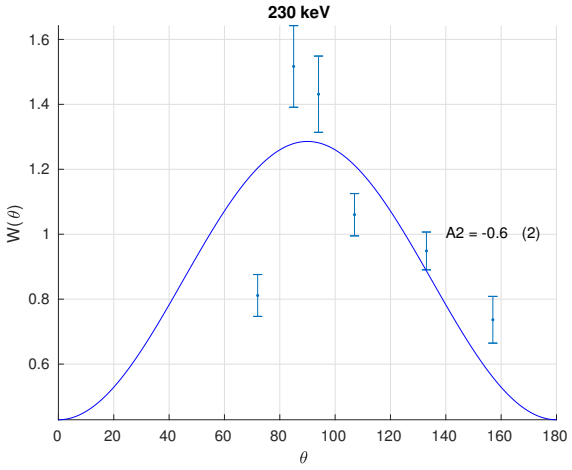
230 keV
W(θ)
θ
A2 = -0.6 (2)